Blade Dynamics and Flux Measurements for Model Seagrass Blades in Waves and Currents

by

Erin Grace Connor

B.S. Chemical Engineering
The University of Notre Dame, 2012

Submitted to the Department of Civil and Environmental Engineering
in partial fulfillment of the requirements of the degree of

Master of Science in Civil and Environmental Engineering

at the

MASSACHUSETTS INSTITUTE OF TECHNOLOGY

September 2014

Signature redacted

Author: _____
Department of Civil and Environmental Engineering
August 8, 2014

Signature redacted

Certified by: _____
Heidi M. Nepf
Donald and Martha Harleman Professor of Civil and Environmental Engineering
Thesis Supervisor

Signature redacted

Accepted by: _____
Heidi M. Nepf
Chair, Departmental Committee for Graduate Students

Blade Dynamics and Flux Measurements for Model Seagrass Blades in Waves and Currents

by

Erin Grace Connor

Submitted to the Department of Civil and Environmental Engineering
on August 8, 2014 in Partial Fulfillment of the Requirements of the Degree of
Master of Science in Civil and Environmental Engineering

ABSTRACT

Complex interactions between flow conditions, blade posture, and mass transport processes, represent a challenge to fully understanding the influence of hydrodynamic conditions on the flux of nutrients to the blade surface of submerged aquatic vegetation. To isolate the physical mechanisms from biological processes, model seagrass blades constructed from low-density polyethylene (LDPE) film were used as a laboratory proxy. In accordance with previous studies of LDPE, the balance of the drag force due to fluid motion and the restoring force due to blade stiffness determined the blade posture in unidirectional flow and the relative motion in oscillatory flow. The blade rigidity was adjusted by changing either the blade length or the blade thickness. Horizontal force measurements showed that the reconfiguration of blades in flow resulted in a less than quadratic power-law relation between force and velocity. Specifically, $F \sim U^{3/4}$. Two techniques and two tracer chemicals (dibromochloromethane and 1,2-dichlorobenzene) for estimating uptake by LDPE, as an analogue to nutrient uptake by seagrass, are described and compared. Mass uptake by blades during flux experiments demonstrated mixed control by both the LDPE-side and water-side mass transfer velocities. In experiments using 1,2-dichlorobenzene, measured uptake was fit to a numerical diffusion model to estimate the water-side transfer velocity. The water-side transfer velocity had a non-linear dependence on velocity in that the rate of increase of the mass transfer velocity decreased with greater blade bending in flow.

Thesis Supervisor: Heidi M. Nepf
Title: Donald and Martha Harleman Professor of Civil and Environmental Engineering

ACKNOWLEDGEMENTS

First and foremost, I would like to thank my advisor, Heidi Nepf. I am extremely grateful to her for all the guidance and encouragement she offered to me throughout this project. As a mentor, she truly puts her students first. In many ways, she allowed me to take ownership of this project and my experience as a graduate student, which has helped me to grow both as a scientist and as a person. I would also like to thank the rest of the Nepf research group, especially Jeff Rominger, Elizabeth Finn, Judy Yang and John Kondziolka. They helped me learn the ropes of fluid mechanics research, sacrificed their time to help with experiments, and became good friends. In addition, I owe a special thanks to the Gschwend lab, and in particular to John MacFarlane and Patricia Tcaciuc. Their knowledge of organic chemistry and passive samplers was invaluable and their patience unmatched. Their contributions to the project improved it immensely, and I am thankful beyond words. Thanks are also due to Anthony Carrasquillo and Kelsey Boulanger. Their advice on chemistry, grammar, and graduate student life is greatly appreciated.

Finally, I owe so much gratitude to my friends and family. In Cambridge, I found a home away from home, and that is entirely due to the wonderful people I have had the pleasure of meeting here. The community in the Parsons lab has been a source of comradery and laughter, which has made the challenges of graduate school bearable. I would also like to recognize my close friends Meghan and Casey who shared in all of my successes and failures over the last two years. Last by not least, I would like to thank my family. Even half way across the country, their love and support are my rock and my source of strength. I owe all my humble accomplishments to them and to the joy they bring into my life (especially you two, Audrey and Jack).

CHAPTER 1. INTRODUCTION

It is widely recognized that seagrass provides indispensable ecological and economic services. Seagrass inhabits coastal areas all over the world in great diversity. Over fifty separate species are recognized with a great variety of different morphologies within many of those species (Kuo and den Hartog, 2006). Many of the benefits afforded to a coastal area result from the ability of seagrass to attenuate incoming currents and waves. The reduced velocities in and around seagrass meadows protect the shorelines from increased erosion under normal conditions as well as provide protection from extreme storm events by reshaping the coastal landscape over time (Koch et al, 2009). There is further evidence that beyond the simple prevention of erosion, they may retain nutrients within the local soil environment (Barko and James, 1998). The seagrass communities also create sheltered areas, which shrimp and other commercially lucrative fish species use as nurseries (Costanza et al, 1997). Seagrass also benefits its surrounding ecosystem through its high primary productivity (Duarte and Chiscano, 1999). As primary producers, seagrass improves the local ecosystem by preventing anoxic conditions (Waycott et al, 2005). Seagrass supports biodiversity by providing a food source for populations of larger animals, such as manatees, dugong, and sea turtles. Furthermore, seagrass is a globally relevant sink for carbon. In fact, seagrass stores more carbon per hectare than rainforests (Fourqurean, 2014). Because seagrass confers so many advantages to its environment, the protection and restoration of seagrass is of vital importance to the health of coastal ecosystems. A methodology for determining the optimal environmental conditions could be extremely useful for restoration efforts. However, seagrass interacts with the surrounding fluid environment in complicated ways from the blade scale to the meadow scale. Of these

interactions, perhaps the least well understood is the influence of the flow environment on mass transport to the flexible blades of mature seagrass plants.

Seagrasses are capable of acquiring necessary nutrients through their leaf surfaces in addition to their roots (Touchette and Burkholder, 2000; Romero et al, 2006). The scalar transfer of dissolved nitrogen and phosphorus containing chemical species, as well as photosynthesis reactants and products (dissolved inorganic carbon and O_2), at the leaf level may directly affect their growth rates. Understanding the physical mechanism for chemical transport at the blade surface is the key to understanding and, conceivably, predicting their uptake rates. A number of field studies have attempted to show that in conditions where light and other biological factors are not limiting factors, the uptake of nutrients is governed by the hydrodynamic conditions (eg. Cornelisen and Thomas, 2006 and 2009; Nishihara and Ackerman, 2006; Morris and Peralta, 2008). These studies have shown that an increase in flow rate over the plants results in an increase in uptake. Several of these studies have also shown that wave conditions may result in an enhancement of flux to the plants beyond equivalent unidirectional flows (Thomas and Cornelison, 2003).

There are several approaches to describing the physical mechanism for mass transport to submerged aquatic vegetation (SAV) leaves. Many of these approaches begin by assuming a diffusive boundary layer close to the surface of the leaf. Above the diffusive boundary layer, the concentration of the chemical species of interest is considered to be well-mixed by turbulent mixing. Within the diffusive boundary layer, the concentration follows a continuous gradient to the leaf surface. Because turbulence compresses the diffusive boundary layer to very near the surface, the concentration profile is most often assumed to be approximately linear. Mass transport across the diffusive boundary layer is

limited by molecular diffusion and typically described using Fick's law. This framework is illustrated in Figure 1-1 and described mathematically using Equation 1.1,

$$J = k\Delta C = \frac{D_w}{\delta_D}\Delta C \tag{1.1}$$

Where J is the mass flux, k is a transfer velocity, ΔC is the concentration difference across the diffusive boundary layer, D_w is the molecular diffusivity of the species in water and δ_D is the thickness of the diffusive boundary layer. Different interpretations of the flow field around the blade lead to different approximations for the thickness of the diffusive boundary layer.

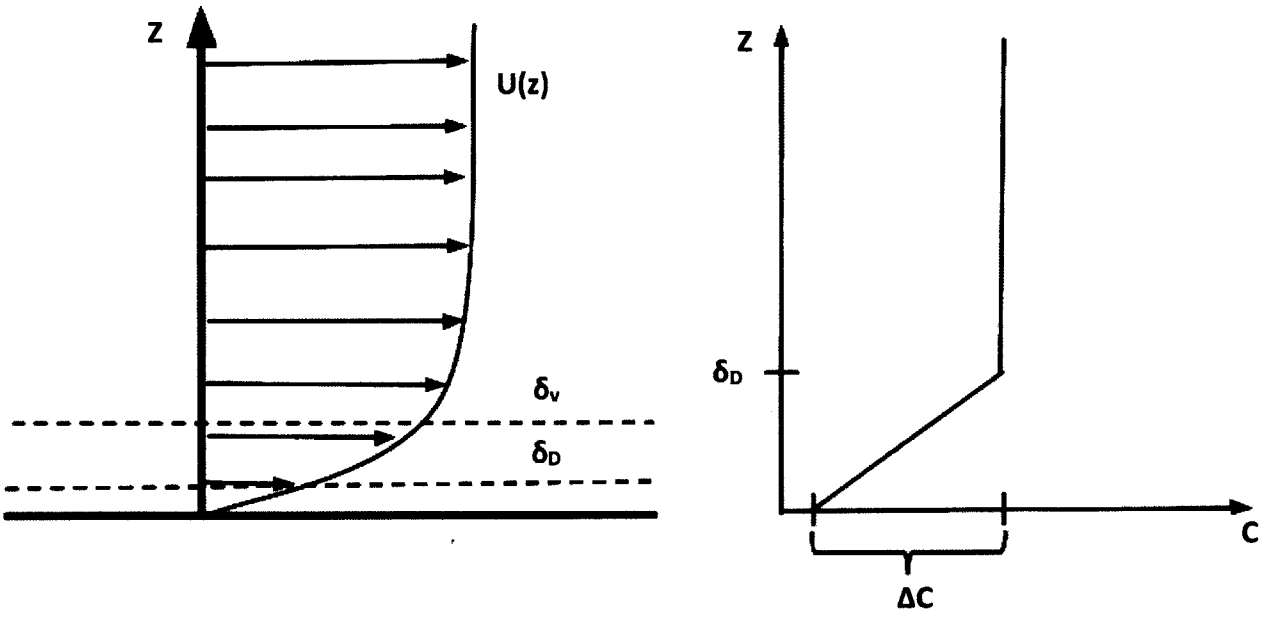

Figure 1-1. Illustration of viscous and diffusive boundary layers.

The most straightforward way to describe the flux to seagrass blades comes from theory on flux to a flat plate. In this case, the no-slip condition at the surface of the blade causes a viscous sub-layer (δ_v) to form above the blade. At the leading edge of the plate, the flow remains laminar and the diffusive boundary layer grows with distance from the plate's

leading edge according to the same dependence on the Reynolds number as the momentum boundary layer (δ). At some distance from the leading edge, the momentum boundary layer becomes turbulent, but the viscous sub-layer remains laminar and maintains a roughly constant thickness with distance along the plate. The thickness of the viscous sub-layer, δ_v, is proportional to the inverse of the friction velocity ($\cong 5v/u_*$). Within the viscous sub-layer, a layer taken to be the diffusive boundary layer (δ_D) forms, which is found empirically to be a function of the Schmidt number ($Sc = v/D_w$, the ratio between diffusive and viscous time scales). Thus, the thickness of the diffusive boundary layer within a turbulent boundary layer is given by Equation 1.2.

$$\delta_D = \delta_v Sc^{-1/3} \tag{1.2}$$

The viscous sub-layer and diffusive boundary layer are shown in Figure1-1. Equations 1.1 and 1.2 together will be called the flat plate model for flux.

Subsequent theories recognized the potential for disturbances of the boundary layer due to wave motions or a moving boundary. In the surface renewal model, the diffusive sub-layer is periodically stripped away, and must regrow between disturbances (Higbie, 1935). This model has been successfully used to describe data from flux experiments in kelp (Stevens and Hurd, 1997; Stevens et al, 2003; Huang et al 2011). The time-averaged flux (indicated by an over-bar notation) derived by Stevens and Hurd (1997) is shown here as Equation 1.3.

$$\bar{J} = \left(\frac{D_w}{\delta_D} + \frac{2\delta_D}{T}\sum_{n=1}^{\infty}\frac{1}{n^2\pi^2}\left(1 - exp\left(-n^2\pi^2\frac{D_w}{\delta_D^2}\right)\right)\right)\Delta C \tag{1.3}$$

In this equation, T is the time between diffusive boundary layer disturbances. If the time between disturbances is very small in comparison to the time for the formation of the turbulent boundary layer ($T_{BL} = \delta_D^2/D_w$), then the flux is significantly enhanced, relative to the flat plate model (Equations 1.1 and 1.2), which assumes a static diffusive sub-layer thickness. However, as the time scale for disturbances approaches infinity, the flux approaches the case for a constant diffusive boundary layer (Equation 1.2). One of the shortcomings of the surface renewal model is that it does not account for the possibility of a partial stripping of the boundary, and therefore it likely overestimates the flux. Also, it is only dependent on the period of the disturbance (wave period or turbulent time-scale), but not on disturbance amplitude or blade characteristics. Intuitively, these factors would seem to be important in determining the intensity of the disturbance. For example, according to the surface renewal model, any two waves with the same frequency are expected enhance the flux to exactly the same degree. However, it stands to reason that a smaller amplitude wave would have less energy and create less of a disturbance to the boundary layer than a larger amplitude wave. The blade characteristics must also play a role in the degree of flux enhancement by waves. Very rigid blades resist motion and can have a higher relative velocity than flexible blades that move with the wave to some degree. Therefore, a rigid blade likely experiences larger disturbances of the boundary layer than a flexible blade going with the flow.

A third alternative theory was developed by Ledwell (1984) who considered the mass transfer coefficient at an air-water interface in comparison to conditions at a smooth wall. In contrast to the previous frameworks discussed which center around a boundary

layer thickness, the Ledwell model starts from the assumption that an eddy diffusivity, taken to be the product of a mixing velocity scale and a mixing length scale, dominates the transfer velocity term. Ledwell argues that the relative perpendicular motion at the boundary is the appropriate velocity scaling for the eddy diffusivity because these motions are responsible for the physical transport of mass. Using these assumptions, the following expressions for the flux is derived (Ledwell, 1984; Rominger and Nepf, 2014):

$$\bar{J} = \frac{3\sqrt{3}}{2\pi}\beta^{1/3}D_w^{2/3}\Delta C \tag{1.4}$$

Where,

$$\beta \approx \left.\frac{\partial \nabla \cdot v'}{\partial z}\right|_{z=0} = \frac{\partial^2 w'}{\partial z^2} \approx \frac{u_{rel}}{b^2} \tag{1.5}$$

$\nabla \cdot v'$ is the two dimensional divergence tangent to the interface. The divergence scales with the turbulent component of the velocity field perpendicular to the surface. Furthermore, because the width of the blade (b) is several times less than the length, Rominger and Nepf (2014) assume the divergence scales as the relative velocity (u_{rel}) divided by the blade width resulting in the right hand expression in Equation 1.5. The precedent of this scaling argument comes from studies of flow normal to bluff bodies (Sparrow et al, 1979; Koumoutsakos and Shiels, 1996). An interpretation of this relationship is that for very little relative motion, the blade moves passively with the fluid and the molecular diffusivity contributes a larger fraction to the overall transfer velocity. On the other hand, if the relative motion is large, fluid motions carry mass to the blade surface much more quickly than would occur by molecular diffusion alone.

There are a number of ways the impact of flow conditions on flux may be complicated by biological mechanisms which compensate for varying flow conditions. For

example, some species are capable of shifting carbon equilibria by releasing H^+ ions, complicating the interpretation of flux measurements made by photosynthesis rates (Kuo and den Hartog, 2006). This is further supported by studies which have shown that different species may have adapted to diffusive boundary layer limiting conditions more than others (Jumars et al, 2001). Nishihara and Ackerman (2009) also provide an example of how the relationship between seagrass and hydrodynamics may be more complicated than a simple boundary layer model by comparing the timescale for diffusion to the measured uptake rates of O_2 by the freshwater SAV *Vallisneria Americana.* The measured timescale for uptake, based on vertical concentration profiles, was longer than the timescale for diffusion through a diffusive boundary layer whose thickness was determined experimentally by measuring the momentum boundary layer using particle image velocimetry. They interpret these results as indicating that the physical uptake of dissolved inorganic carbon (DIC) was not limited by physical transport through a diffusive boundary layer, but rather by some other physicochemical process.

Light availability is another example of a potential biological complication. Even though most studies provide saturating light conditions, the reconfiguration of blades by flow may shade some blades, creating areas where light is still limiting (Zimmerman, 2006; McKone, 2009). A third example of biological complications in understanding flux to seagrass blades comes from the ability of some seagrass to store nutrients for use during nutrient poor times (Sanford and Crawford, 2000). If environmental conditions do result in unfavorable mass transport regimes, it seems likely that these plant species have evolved to compensate. Unfortunately, a lack in research into the mechanism of mass transfer to

solid flexible boundaries make it difficult to predict and explain the mass uptake differences observed for live plant experiments.

In addition to the biological mechanisms just discussed, other physical mechanisms make it difficult to understand the impact of hydrodynamics on blade-scale transport processes. Because the plants are usually in meadows, which are known to alter their surrounding flow conditions, it is possible that within a single canopy different mechanisms may apply to mass transfer to different blades. Multiple studies have shown that uptake rates of nitrogen are significantly impacted by the location of a particular blade in the meadow. While Morris and Peralta et al (2008) observed 20% greater uptake rates for the blades at the leading edge of a patch, Bal et al (2013) observed more complicated flow and species dependent spatial patterns in addition to flux enhancement at the leading edge. Bal et al (2013) also showed that for two different species of fresh water submerged grasses, *Potamogeton natans* and *Ranunculus fluitans*, the degree of correlation between the uptake of nitrogen and the turbulent kinetic energy increased for a meadow with a higher characteristic shoot density. This result implies that canopy characteristics may determine whether blade scale diffusion or patch scale turbulence events are more important for transporting nutrients to seagrass.

At the meadow scale, oscillatory flows are known to interact with submerged canopies differently than unidirectional flows. Relative to current-dominated flow conditions, wave-dominated flow conditions are associated with diminished in-canopy flow attenuation (Lowe et al, 2005a; Luhar et al, 2010), enhanced mixing between the bed and water column (Koch and Gust, 1999), and enhanced nutrient flux (Weitzman et al 2013; Lowe et al, 2005b; Thomas and Cornelisen, 2003). For example, Lowe et al (2005a) showed

that the flow penetration for wave motion exceeded that for unidirectional current. They also demonstrated that the resultant depth averaged canopy velocities could account for flux enhancements observed for oscillatory flow in comparison to unidirectional flow of the same overall magnitude (Lowe et al, 2005b). However, Weitzman et al (2013) showed that while the increased flow penetration of wave motion also occurs for flexible canopies, the depth averaged velocities could not fully account for flux enhancement. Because the canopy used by Lowe et al (2005b) was made up of rigid cylinders, Weitzman et al (2013) suggest the additional flux enhancement, witnessed especially at high wave frequency, is likely due to the more dynamic blade motion possible for flexible structures. The importance of blade posture is further supported by observed correlations showing an increased uptake for a lower bending angle (Bal et al, 2013; Morris and Peralta et al, 2008).

In all models discussed here, higher velocities are expected to increase the flux. However, the complex interactions between blade posture, velocity, and flux make it extraordinarily difficult to predict a relationship between velocity and flux. A blade oriented in the stream-wise direction has a flux that can be more easily related to the velocity. As the velocity over a fully pronated blade increases, the boundary layer thins, causing a greater overall flux to the surface. A fully erect blade acts as a bluff body in the flow. The upstream face likely experiences a stagnation point limiting the flux whereas the downstream face may experience increased turbulent mixing enhancing the flux. Overall, it is difficult to say how the cumulative effect might compare to a pronated blade at the same flow rate. Intermediate postures are even more complex. The angle to the incident flow field could conceivably accelerate the flow over the top face of the blade thinning the boundary layer and enhancing the flux. Then again, there may still be a stagnation point

and enhanced turbulence on the blade's underside. Sparrow and Tien (1977) studied mass loss from a square plate inclined to oncoming airflow and found it to be independent of the plate angle. Denny and Roberson (2002) measured the heat transfer from a flat plate in a wind tunnel saw and a similar lack of dependence on the pitch. However, in low flow conditions, the pitch-independent flux was somewhat greater than the flux to a completely horizontal plate. The inherent linkage between blade posture and velocity implies that as the velocity is increased, the blades pass through multiple regimes that have a slightly different dependency on velocity. It remains unclear what the overall impact of blade reconfiguration will be on flux as a function of velocity. To be applicable across many flow conditions and species, a flux model will need to account for the physical parameters of seagrass as well as the local hydrodynamic conditions.

In addition to flux measurements, there have been a number of studies that examine the influence of hydrodynamic conditions on blade motion. A number of physiological factors can impact how seagrass interacts with different hydrodynamic conditions at the blade scale. Stiffness, blade density, thickness and length all play important roles in determining the posture of blades under currents and waves (Luhar and Nepf, 2011; Zeller et al, 2014). The posture is also an important factor to consider when predicting the flux to and from the blade surface in physical transport limited regimes. As a result, the same physiological variables determining the posture of the blade likely can be used to predict the potential flux to the blades given a particular set of wave and current conditions. In particular, Luhar and Nepf (2011) showed that these physiological parameters can be condensed into two dimensionless parameters: B and Ca. The buoyancy parameter, B, represents the balance in buoyant forces to the restoring force due to stiffness. The Cauchy

number, Ca, is the ratio of the drag force to the restoring force due to the stiffness of the blade. The equations are shown below.

$$B = \frac{(\rho_b - \rho_w)gbhl^3}{EI} \tag{1.6}$$

$$Ca = \frac{\rho_b C_D b U^2 l^3}{2EI} \tag{1.7}$$

In both equations, ρ_b is the density of the blade, ρ_w is the density of the fluid, g is the gravitational acceleration, h is the blade thickness, l is the length of the blade, C_D is the drag coefficient, E is the Young's modulus, and I is the second moment of area.

Under wave conditions, an additional parameter is important called the Keulegan-Carpenter number, KC (Luhar, 2012). This number represents the ratio of the wave orbital motion to a relevant geometry length scale. Zeller et al (2014) make a convincing argument for using the blade tip excursion as the geometry length scale by showing that the drag coefficient is most accurately described as function of KC defined as such. However, because this requires an a priori knowledge of the blade motion, it is more practical to use the blade width, as in Luhar (2012).

The many ecological and economic benefits of seagrass motivate our interest in understanding the potential flux of nutrients to seagrass blades. However, complexities in biological and field conditions make it difficult to isolate the influence of physical mass transport processes. Several theories attempt to capture the mechanism with varying degrees of success. Based on previous studies on flux and blade dynamics, it is evident that physical characteristics of the blades play a significant role in the physical mechanism for nutrient transport. The ultimate goal is to develop a useful and robust model while maintaining an appropriate degree of simplicity in order to apply the model to field cases

where knowledge of specific parameters may be limited or only available as large-scale averages. In this work, the three models for flux to flexible blades will be compared using low-density polyethylene (LDPE) as a laboratory analogue for seagrass. First, the applicability of this model to seagrass is demonstrated and its motion characterized. Second, a method for measuring flux to a model seagrass blades will be developed for testing the effectiveness of each theory. The results of flux experiments are presented in comparison to the relevant flux models. Finally, we suggest next steps for improving the method as a tool for achieving the goal of a comprehensive flux model.

CHAPTER 2. BLADE DYNAMICS IN WAVES AND CURRENTS

2.1 INTRODUCTION

A number of studies have attempted to describe and parameterize the flow-induced drag imposed upon a single blade of seagrass. Of particular interest is the reconfiguration, or the bending of flexible plants in response to flow, that often has the effect of reducing drag and protecting plants from damage or uprooting. The reconfiguration of individual blades in flow also determines canopy height canopy height, which plays a dominant role in the flow attenuation by an entire meadow of seagrass (Bradley and Houser, 2009, Luhar and Nepf, 2013). In addition, individual blade dynamics impact other processes relevant to seagrass. For example, reconfiguration can cause self-shading and impact light availability. Also, the posture of the blade may be a significant factor in the formation of diffusive boundary layers and, consequently, nutrient flux.

The forces that determine the degree of reconfiguration are the buoyancy force, the restoring force due to the blade's stiffness, and the drag force. These forces are depicted qualitatively in Figure 2-1.

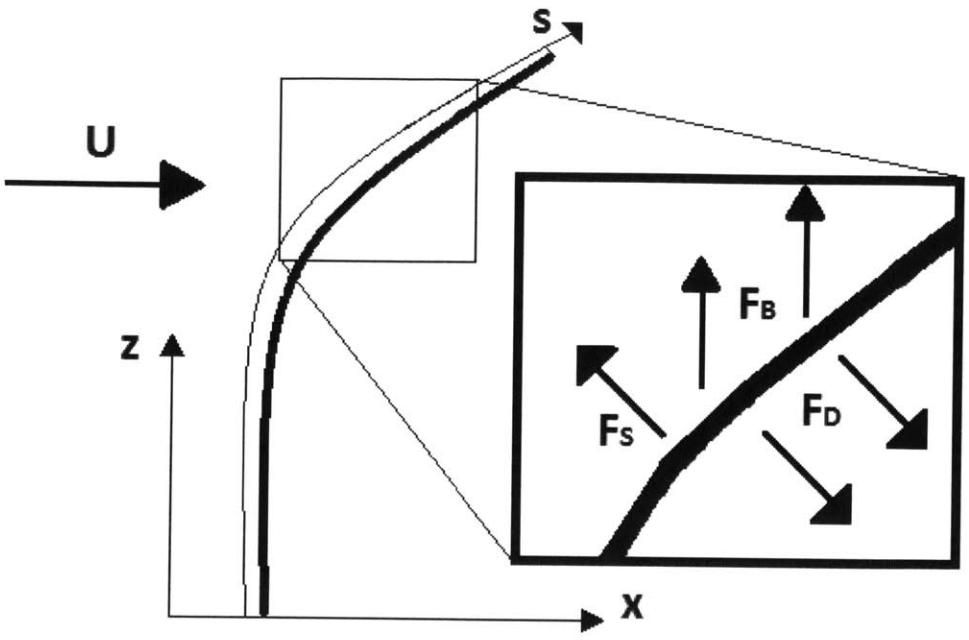

Figure 2-1. Illustration of the forces acting on a blade in flow and coordinate systems. The drag force, F_D, and the buoyancy force, F_B, act along the length of the blade in the blade normal and vertical (z-) directions, respectively. The restoring force due to stiffness, F_S, acts in the blade normal direction. The s-direction is defined by the location along the length of the blade with s = 0 at the base of the blade.

A more complete mathematical description of the forces acting on the blade are given by Luhar and Nepf (2011), who show the proper scaling of the equation governing blade motion leads to two dimensionless parameters important for dynamic similarity. The definitions of these parameters were given in Chapter 1 and are restated here as Equation 2.1, which represents the ratio of the buoyancy force to the restoring force due to blade rigidity, and Equation 2.2, which represents the ratio of the drag force to the restoring force due to blade rigidity, with the later called the Cauchy number.

$$B = \frac{(\rho_b - \rho_w) g b t l^3}{EI} \tag{2.1}$$

$$Ca = \frac{\rho_b C_D U^2 b l^3}{2EI} \tag{2.2}$$

Where ρ_b is the blade density, ρ_w is the fluid density, g is the gravitational acceleration, h is the blade thickness, l is the length of the blade, b is the blade width, C_D is the drag coefficient, E is the young's modulus, and I is the second moment of area ($=bt^3/12$). The results of Luhar and Nepf (2011) are especially useful in that they provide a means for predicting the posture of the blade from knowledge of the blade's physical characteristics and surrounding flow environment. Additionally, they show that, for Ca ≤ 2.5 and B << 1, the stream-wise force varies as $F_x \sim U^2$. The blade effectively acts as a stiff, erect plate with a drag force equal to $1/2\rho C_d b l U^2$. Whereas for Ca >> 1, the blade is in a pronated posture, and the horizontal force goes as $F_x \sim U^{3/4}$. Because buoyancy resists reconfiguration, as B increases, the transition to a fully pronated posture occurs at larger Ca and the force scales with velocity to different power, i.e. $F_x \sim U^a$ with a < 1. The deflected height of the blade is a function of Ca and B. These results are summarized in Figure 2-2 (Fig. 2 (c) from Luhar and Nepf, 2011) which shows both the deflected height and the normalized horizontal force varying with Ca for discrete values of B. The transition in how the force varies with velocity as a result of the blade posture may provide insight into the fluid environment at the blade surface. For example, more vertical postures are associated with stagnation zones both upstream and downstream of the blades whereas blades in streamlined postures have boundary layers that more closely resemble flat plate boundary layers. It's worth noting that the blade postures and drag values shown in Figure 2-2 only reflect form drag. Luhar and Nepf hypothesize that the skin friction may become more important for $F_x/\left(\frac{1}{2}\right)\rho C_d b l U^2 < 0.05$.

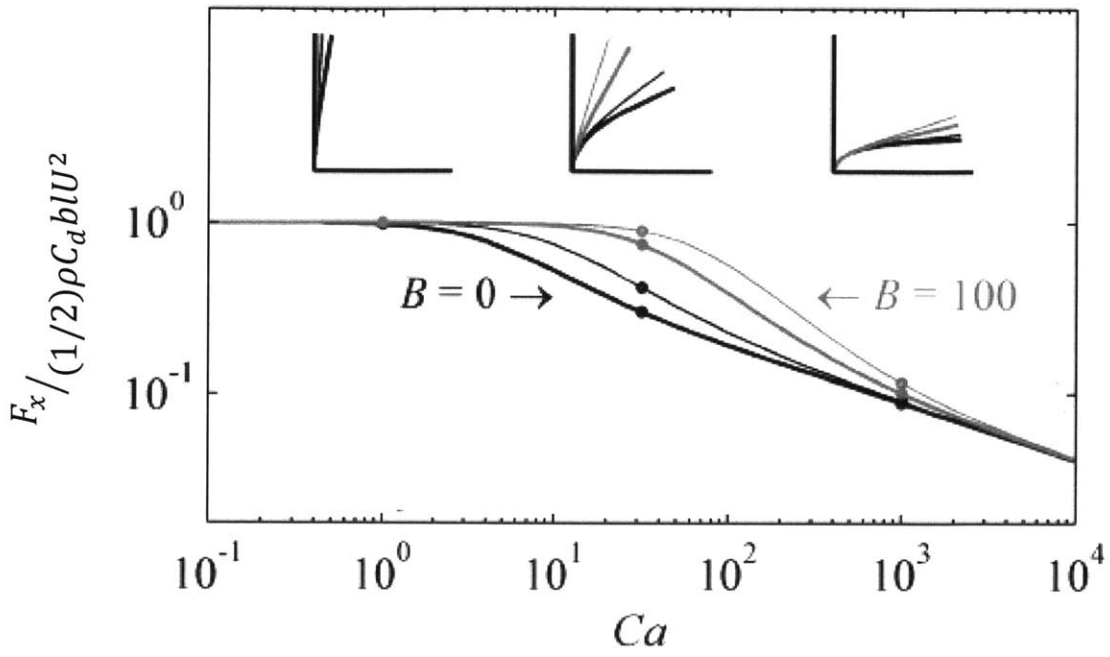

Figure 2-2. Model predictions for the normalized horizontal force and blade posture made by Luhar and Nepf (2011). The force is plotted against the Cauchy number (Ca) for B = 0 (thick black line), 10 (thin black line), 50 (thick grey line), and 100 (thin grey line). The subsets show the blade postures with the different lines representing the four values of the buoyancy parameters. The dots on the force plot correspond to the postures shown for Ca = 1, 32, and 1000.

When comparing unidirectional conditions to wave conditions, the definitions of Ca and B are essentially the same, but there are differences in the meaning of U and C_D. The velocity is constant in the unidirectional case, but for the wave case it varies throughout the wave period, T_w. The peak wave velocity, U_w, is usually used as the characteristic velocity. For the unidirectional case, the drag coefficient is assumed to be constant and equal to the value found empirically for a flat plate perpendicular to the flow (Vogel, 1994). For the wave case, the drag coefficient is a function of the Keulegan-Carpenter number (KC) as given by $C_D = 10 * KC^{-1/3}$ (Graham, 1980). The Keulegan-Carpenter number is the ratio of the characteristic wave distance (wave excursion) over a length scale characteristic to the

problem of interest. For example, for a cylinder of diameter d in a wave field with peak velocity U_w and period T_w, $KC = U_w T_w/d$. It can also represent the relative importance of drag forces to inertial forces. Originally, KC was developed for the description of wake development around shore structures. A rigid cylindrical geometry was most often considered with the diameter used as the length scale. Since the geometry of seagrass is significantly different, proper consideration must be given to the choice of length scale. Weitzman et al (2013) used element spacing as the length scale in their canopy scale flux experiment (see also Lowe et al, 2005a). Zeller et al (2013) showed that measured drag coefficients collapsed onto a single line when KC was defined using the blade excursion, defined as the maximum displacement distance experienced by a blade in one wave cycle. However, as Zeller et al point out, this definition requires a priori knowledge of the blade behavior in flow, and so has little predictive power. Additionally, most of the Zeller et al cases involve a combination of currents and waves for which the blade became pronated very early in the wave cycle. In this work, the drag force described is a form drag proportional to the frontal area of a single blade in wave-only conditions. The blade width (b) is chosen as the geometric length-scale of the body, which is similar to the cylinder diameter in the original KC definition. Specifically, $KC = U_w T_w/b$. Zeller et al correctly raise concerns that such a simply defined KC omits physical characteristics important for flexible structures in oscillating flow. However, we propose that by incorporating KC into the definition of Ca, blade dynamics can be understood by means of a single parameter without prior knowledge of the blade motion.

The relative motion between the blade and the fluid determines both the drag force and the flux (Luhar, 2012; Rominger, 2013; Rominger and Nepf, 2014). To characterize the

relative motion between the fluid and the blade under wave conditions, we relate the wave excursion to the blade excursion. The blade excursion is defined as the horizontal distance traveled by the blade over the course of one wave period, or x_{BE} = max(x) – min(x) (Figure 2-3). As the bottom of the blade is fixed to the basal stem, the excursion varies along the length of the blade, being greatest near the stem and least at the blade tip. The wave excursion is a measure of the distance traveled by a fluid parcel over half a wave cycle, or $A_w = T_w U_w / 2\pi$. Specifically, the maximum distance traveled by a fluid parcel within a wave cycle is $2A_w$ (see Figure 2-3). Finally, we define the relative velocity between the blade and the fluid as the difference between the wave and blade excursion divided by the wave period.

$$U_{rel} = \frac{\pi}{T_w}(2A_w - x_{BE}) \tag{2.3}$$

Additionally, a relationship between the excursion, KC and Ca can be found. Assuming the buoyancy force is insignificant (B << 1) and the drag force acts uniformly along the length of the blade, we can use a cantilever bending equation to approximate the maximum deflection of the blade.

$$x_{BE,tip} = \frac{F_D l^3}{8EI} = \frac{\frac{1}{2}\rho_b C_D U_W^2 b l^4}{8EI} = \frac{1}{8} Ca * l \tag{2.4}$$

This relation between the maximum blade tip excursion and Ca holds for small bending angles which holds for Ca < 8.

Depending on the wave and blade conditions, three regimes are possible. For a stiff blade with small to moderate wave strength (specifically, Ca < 8), there will be minimal blade deflection and the relative velocity will approach the wave velocity (Figure 2-3 (a)). For more flexible blades under similar flow conditions (Ca > 8), the blade will move passively with the waves over most of the wave cycle, and there will be little relative motion (Figure 2-3 (b)). However, if the blade is sufficiently flexible to pronate (Ca>8) and the wave excursion is much larger than the blade length ($l/A_w << 1$), the blade is stationary and pronated over most of the wave cycle, and the relative velocity will again approach the wave velocity. This third regime occurs for Ca >> 8 (Figure 2-3 (c)).

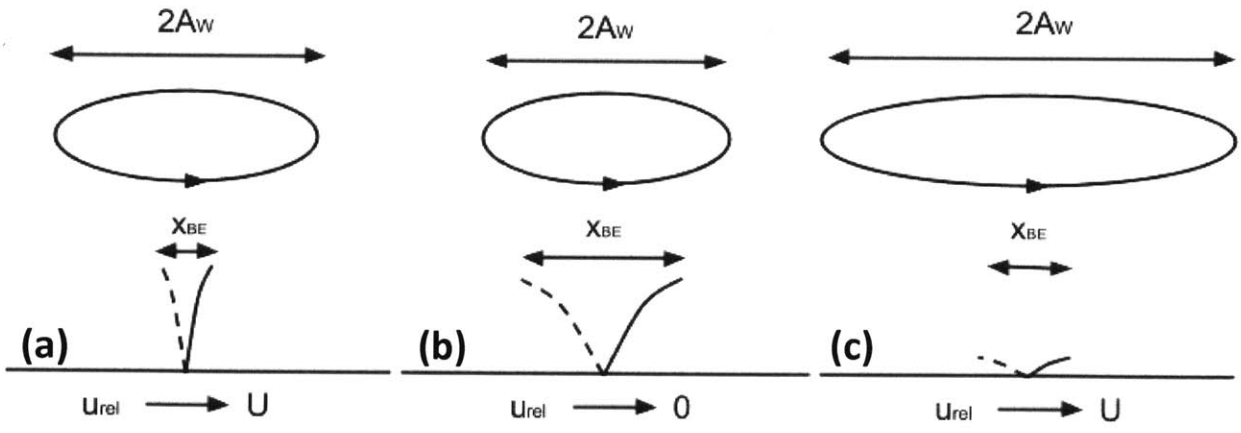

Figure 2-3. Different possible regimes for blades in oscillatory flow.

In this chapter, we consider the effects of unidirectional and oscillatory flow conditions on a single flexible blade. A laboratory proxy for seagrass blades was constructed from low-density polyethylene. The results presented here confirm the dynamic similarity between the model system and seagrass. For unidirectional flow, we

measured the posture of the blades and the horizontal forces over a range of velocities. For oscillatory flow, we recorded blade motion and determined the relative velocity over a range of Cauchy numbers. Furthermore, the results provide a basis for distinguishing between blade behavior regimes as the experimental conditions are changed. The ability to differentiate these regimes becomes especially relevant when interpreting flux experiments. The flow environment right at the blade surface can be difficult to observe experimentally. However, we can use our understanding of how the flow affects the posture and drag forces to infer the surface conditions. The observed transitions between regimes presented in this chapter inform our interpretation of subsequent flux experiments carried out with the same model seagrass and flow conditions.

2.2 METHODS

Model seagrass blades were fashioned from low-density polyethylene (LDPE) film with a Young's modulus, E, of 0.3 GPa and density, ρ_b, of 0.925 g/cm^3 (Ghisalberti and Nepf, 2002). Two different lengths, 15 cm and 5 cm, were cut from 0.25 mm thick LDPE. A single length, 15 cm, was cut from 1.6 mm thick LDPE. All blades were 1 cm wide and assumed to have the same Young's modulus and density. By varying the thicknesses and lengths of model blades, the Cauchy number could be tuned to represent a range of dynamic behavior. Not only did this range capture different physical regimes in mathematical parameter space, but it was also consistent with the wide range of Ca values observed in the field for seagrass. The model blade physical characteristics in combination with the wave conditions used in experiments resulted in Ca ranging from 0.25-380. A wider range of velocities were examined under unidirectional conditions but only for the thinner LPDE

resulting in Ca ranging from 3.0-1200. These values are shown in comparison to typical seagrass in Table 2.1. Even though for the current experiments B > 1, from Figure 2-2 we can see that this will only have a slight impact on the Ca number where the blade behavior deviates from a flat plate. Therefore, we assume that the buoyancy is insignificant for all model cases. As seen in Table 2.1, the mean B for real seagrass fits this assumption, however may be important in certain cases such as seagrass with enhanced buoyancy due to lacunae. We carried out experiments in a 24 m long, 38 cm wide flume filled to 38 cm depth. Blades were mounted on an acrylic ramp placed approximately 10 m from the pump inlet and 10.5 m from the wave maker paddle. Above the ramp, depth was reduced to 25 cm. This setup is shown in Figure 2-4.

Table 2.1 Physical parameters of seagrass in comparison to LDPE model blades

	Thalassi testudinum[1]	*Zostera marina*[2]	*Posidonia oceanica*[3]	Current Experiments	Wave Experiments
t (mm)	0.3-0.37	0.15-0.225	0.2	0.250	0.250, 1.6
b (cm)	1	0.3-0.475	1	1	1
l (cm)	0.1-0.25	0.15-0.6	0.15-0.5	15	5, 15
ρ_b (kg m^{-3})	942	700	910	920	920
E (GPa)	0.4-2.4	0.26	0.47	0.3	0.3
B	3.0e-5-0.0042	0.0098-1.4	0.0024-0.09	2.2	0.054-2.2
Ca	0.036-4000	3.7-500000	3.8-88000	3.0-1200	0.25-380

[1]Bradley and Houser (2009)
[2]Fonesca et al (2007), Abdelrhman (2007)
[3]Folkard (2005)

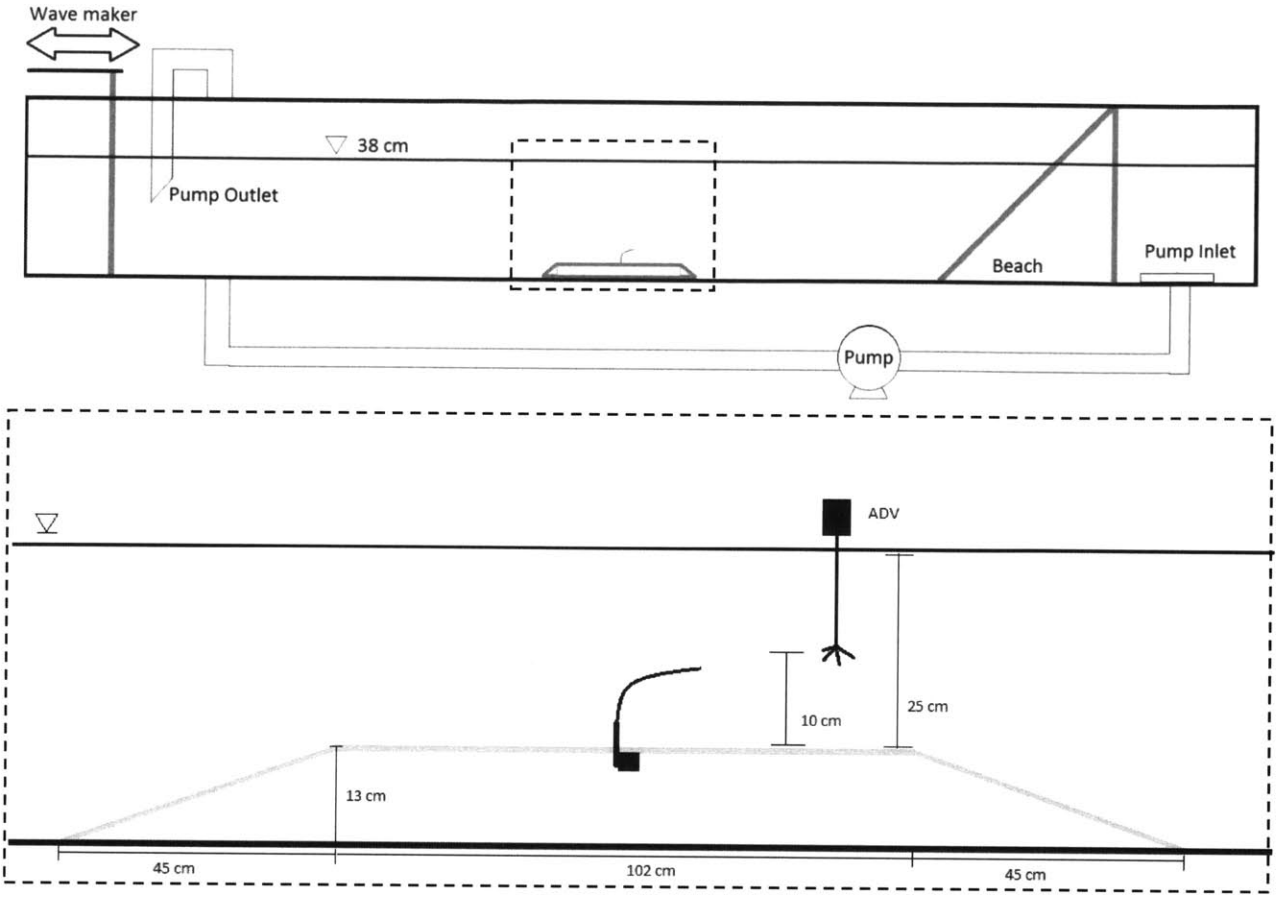

Figure 2-4. Schematic of experimental setup. Wave and current experiments were run separately with the beach removed while the pump was operating. ADV measurements were taken in the same horizontal location as the blade mounting in between experiments in which the blade was present in the flume. Not to scale.

2.2.1 Current Experiments

For unidirectional flows, the flow rate of a recirculating pump was adjusted to produce the mean velocities shown in Table 2.2. Velocity measurements were taken at 2 cm increments in the vertical above the center of the ramp using 3D Nortek Vectrino Acoustic Doppler Velocimetry (ADV). As seen in Figure 2-5, the velocity profiles were roughly constant with vertical position above 4 cm ($z / h = 0.1$) from the ramp's surface.

Table 2.2 Unidirectional experimental conditions and LDPE model blade parameters										
Thickness (mm)	**0.25**		**Experiment 1**				**Experiment 2**			
Length (cm)	**15**									
Width (cm)	**1**	**U (cm/s)**	5.3	10.3	20.7	39.6	2.0	4.5	9.4	19.2
E (GPa)	**0.3**									
ρ_b (kg/m3)	**920**	**Ca**	22	82	330	1200	3.0	16	68	290
B	**2.2**									

Additionally, the height of the blade tip above the ramp was determined for each velocity visually using a meter stick. A load cell (FUTEK) measured the force on the blade in the horizontal direction. A bridge completion module (National Instruments NI-USB 9237) connected the load cell to a computer where the electrical response of the load cell was monitored and recorded using NI Labview. The load cell was initially calibrated using known weights ranging from 0-0.006 N, which demonstrated an approximately linear response factor. For each flow condition, the force on a bladeless mount was also measured and subtracted from the total force recorded when the blade was present. Data was recorded at 1 kHz for 2 min to obtain an average force.

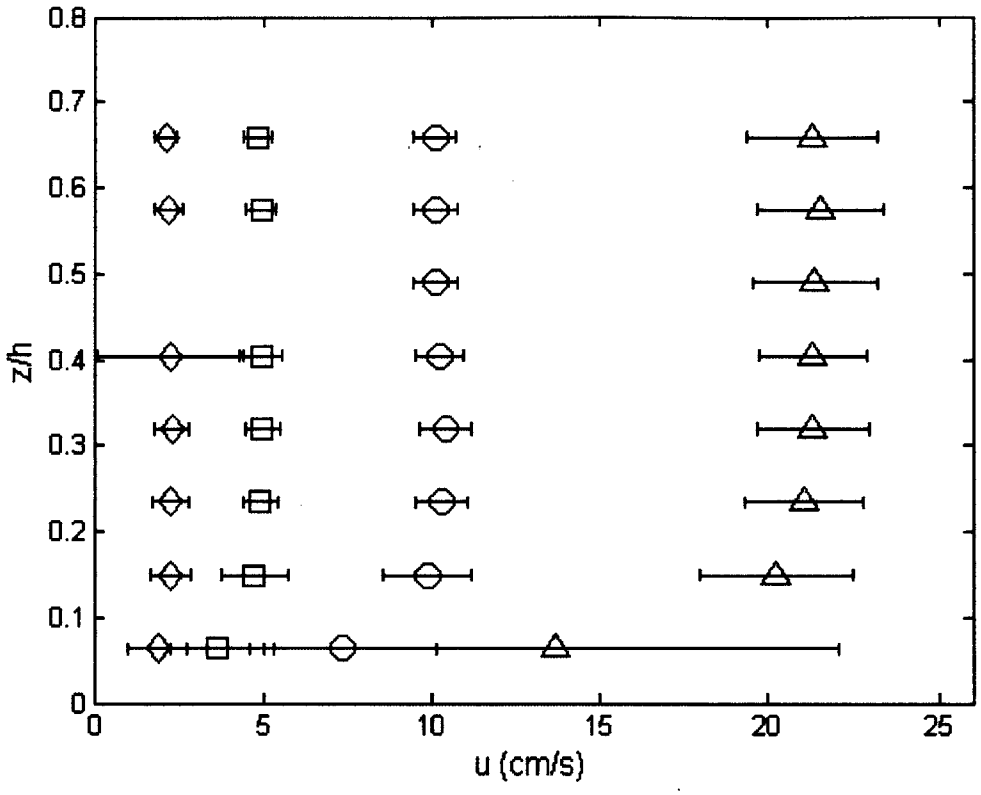

Figure 2-5. Vertical profile of the stream-wise velocity. Different symbols indicate a different pump setting. The horizontal error bars show the 95% confidence interval on the mean from the ADV time series.

2.2.2 Wave Experiments

The flume is fitted with a paddle wave maker which was controlled using a programmable signal generator (Syscomp WGM-101). Given a water depth, an appropriate wave form can be loaded into the signal generator such that the paddle creates waves of a desired frequency and amplitude. The waveform was created using Luhar's (2012) code developed in Matlab and based on the closed form solution for piston movement. A large ramp, "beach", extending above the water level was placed at the downstream end of the water channel to reduce waves reflected off the back wall of the flume. Waves with a period of 2 seconds and amplitude of either 1 cm or 4 cm were generated resulting in a RMS velocity of 3.9 cm/s and 13.0 cm/s, respectively, measured with an ADV placed 10 cm

above the center of the ramp. A phase average of the ADV velocity for each condition is shown in Figure 2-7, and a summary of experimental conditions is provided in Table 2.3. The drag coefficients shown in Table 2.3 were calculated using $C_D = 10 * KC^{-1/3}$. The waves exhibited a behavior typical of Stoke's waves in that the wave crests were somewhat larger and steeper than the wave troughs.

Table 2.3 Oscillatory experimental conditions and LDPE model blade parameters

		LDPE 1	LDPE 2	LDPE 3
Thickness (mm)		0.25	0.25	1.6
Length (cm)		15	5	15
Width (cm)		1	1	1
E (GPa)		0.3	0.3	0.3
ρ_b (kg/m^3)		920	920	920
B		2.2	0.082	0.054
U_w (cm/s)	**Cd**		**Ca**	
6.2	4.4	67	2.5	0.25
18.9	2.7	380	14	1.5

In order to determine the relative velocity experimentally for comparison to flux experiments, videos of blades exposed to each wave condition were taken using a Sony digital camera and Fire-i video capture software at a rate of 15 frames per second and with a resolution of 640 x 480 pixels. The videos were then analyzed using the image processing toolbox in Matlab. In order to resolve movement along the length of the blade, blades were painted black in 1 cm intervals along the length of the blade and placed in front of a white background with front lighting. Images were first converted to black and white so that only the black sections of the blade appear in the images. The algorithm then identified the locations where a transition from white to black (or vice versa) occurred. The positions of

these transitions were then ordered according to location along the blade and tracked through time. Figure 2-6 shows how the algorithm processes images using an exemplifying frame. Additionally, the vertical position of the wave surface was tracked in the videos and correlated to the blade motion. The excursion of the blade as a function of length along the blade was determined by subtracting the average minimum x location from the average maximum x location of the blade over approximately 10 wave cycles. For the 15 cm thin blades, the algorithm occasionally was unable to resolve the different 1 cm locations as the blade bent over on itself while returning from the most upstream position. Because only the maximum and minimum locations of the blade sections are considered for subsequent calculations, this error should not impact the analysis considered here.

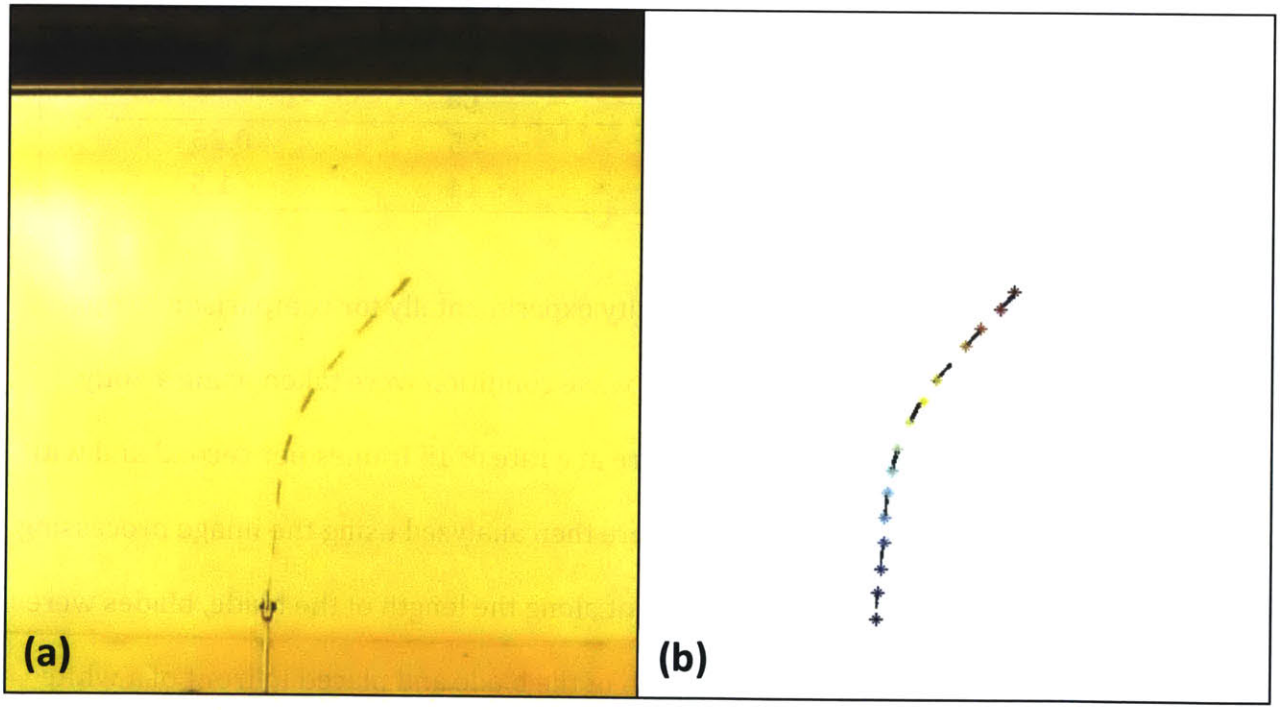

Figure 2-6. Examples of original (a) and processed (b) still frame images from videos used to determine blade motion relative to fluid motion.

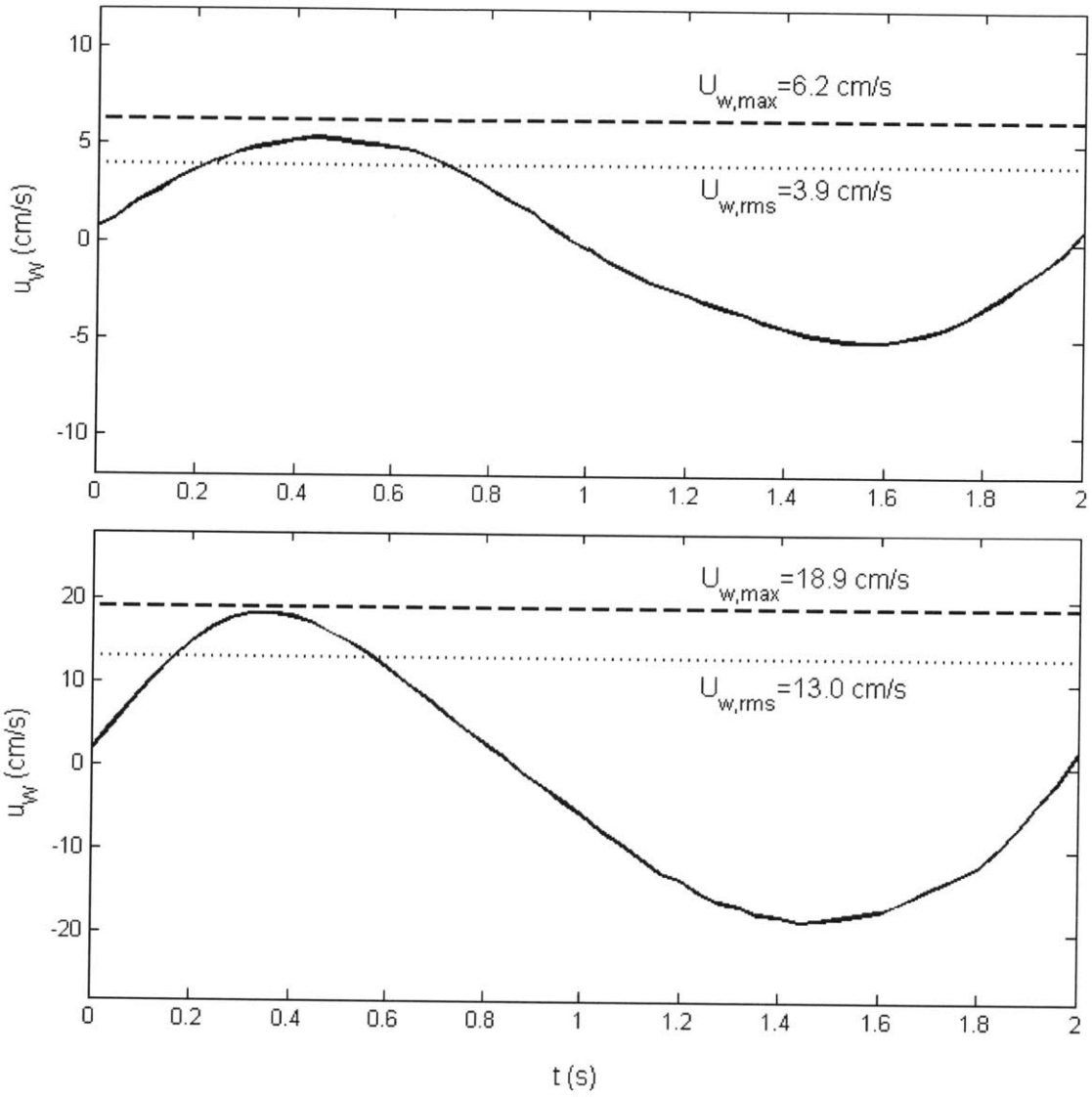

Figure 2-7. Phase averaged wave velocities for waves with 1 cm (top) and 4 cm (bottom) amplitudes.

2.3 RESULTS

2.3.1 Current Experiments

Figure 2-8 shows the reconfiguration of two different blades as the velocity is increased. The vertical height of the blade tip above the base is normalized by the blade length which was 15 cm for both cases. The solid line represents an exponential fit to the data. The decrease in blade tip height with increasing velocity was most dramatic at low

velocities (U < 10, Ca < 80). It also appears somewhat more variable from blade to blade at lower velocities in comparison to higher velocities. During measurements, it was noted that some blades had a pre-existing bias to bend or sag to one direction. At the low velocities (U < 10, Ca < 80), the blade tip height may be more susceptible to these biases likely resulting from the way the sheeting was rolled for storage prior to being cut.

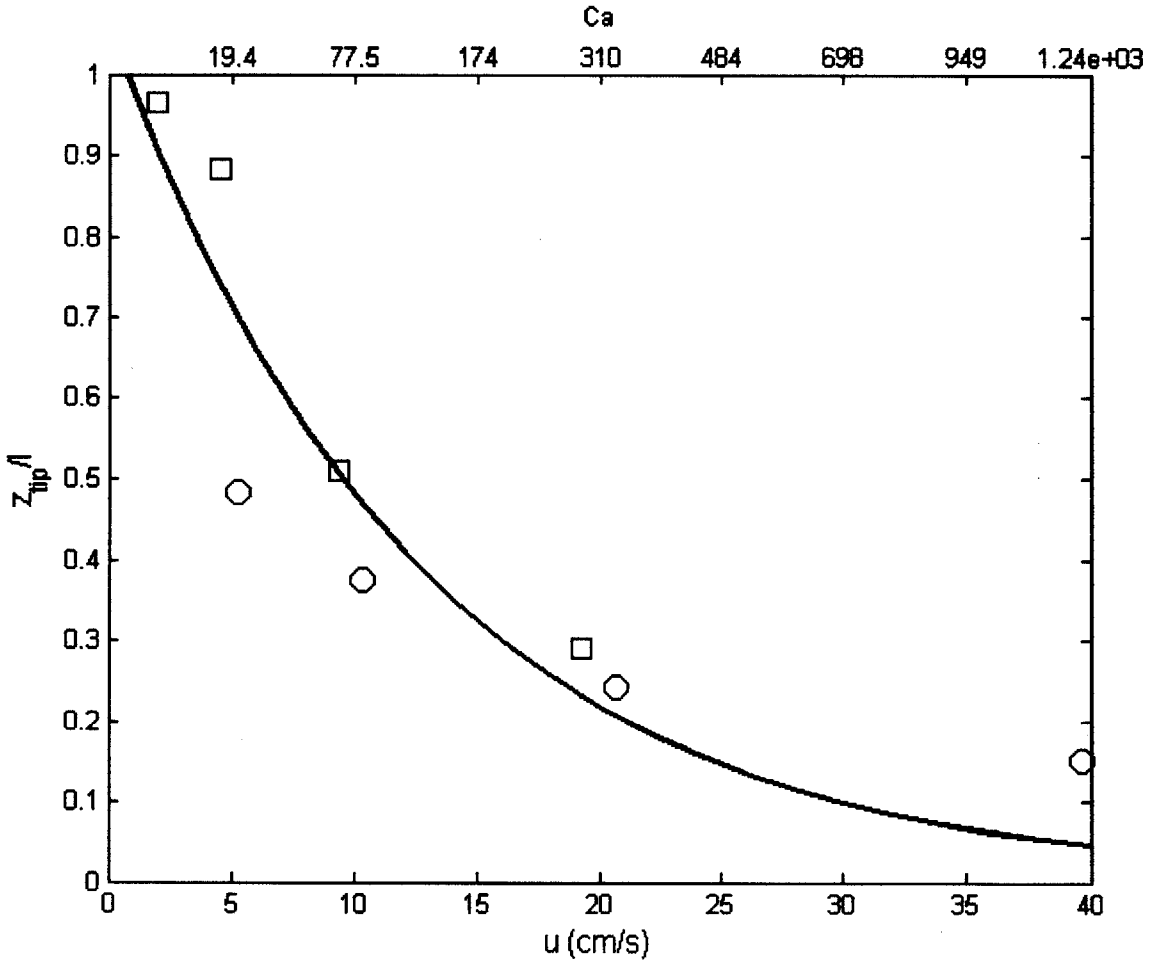

Figure 2-8. Deflected blade tip height normalized by blade length as a function of flow velocity. Different symbols correspond to different blades used and the solid line shows an exponential fit to the data (y = 1.03 * exp[-0.08 * u]). All blades shown were the same dimensions (1 cm x 15 cm x 0.25 mm). Error bars are comparable to symbol size.

Table 2.4. Deflected blade tip height above the top of the blade mounting								
U (cm/s)	2.0	4.5	5.3	9.4	10.3	19.2	20.7	39.6
Z_{tip}/l	0.966	0.883	0.483	0.510	0.376	0.290	0.242	0.150

The results of the force measurements related to the horizontal drag are presented in Figure 2-9 and Table 2.5. Luhar and Nepf (2011) predict the horizontal force to have a scaling law $F_x \propto U^a$ with $a = 4/3$ for Ca ≥ 2.5. The nonlinear fit of the drag data found using a least squares method resulted in $a = 1.4 \pm 0.3$, and is shown in Figure 2-9. The measured scaling law was notably much less than a quadratic scaling law (a = 2) associated with rigid blades, and it agreed with the predicted scaling law. Because an upright, rigid blade has a quadratic scaling law, the deviation from the quadratic scaling law indicates that reconfiguration significantly impacted the drag for all flow rates tested. Additionally, the predicted scaling law of $a = 4/3$ was derived assuming that the buoyancy force and the drag due to skin friction are negligible in comparison to form drag and the restoring force due to stiffness.

Table 2.5 Horizontal force measurements				
U (cm/s)	2.0	4.5	9.4	19.2
F_x (N)	0.0005	0.0025	0.0048	0.0155

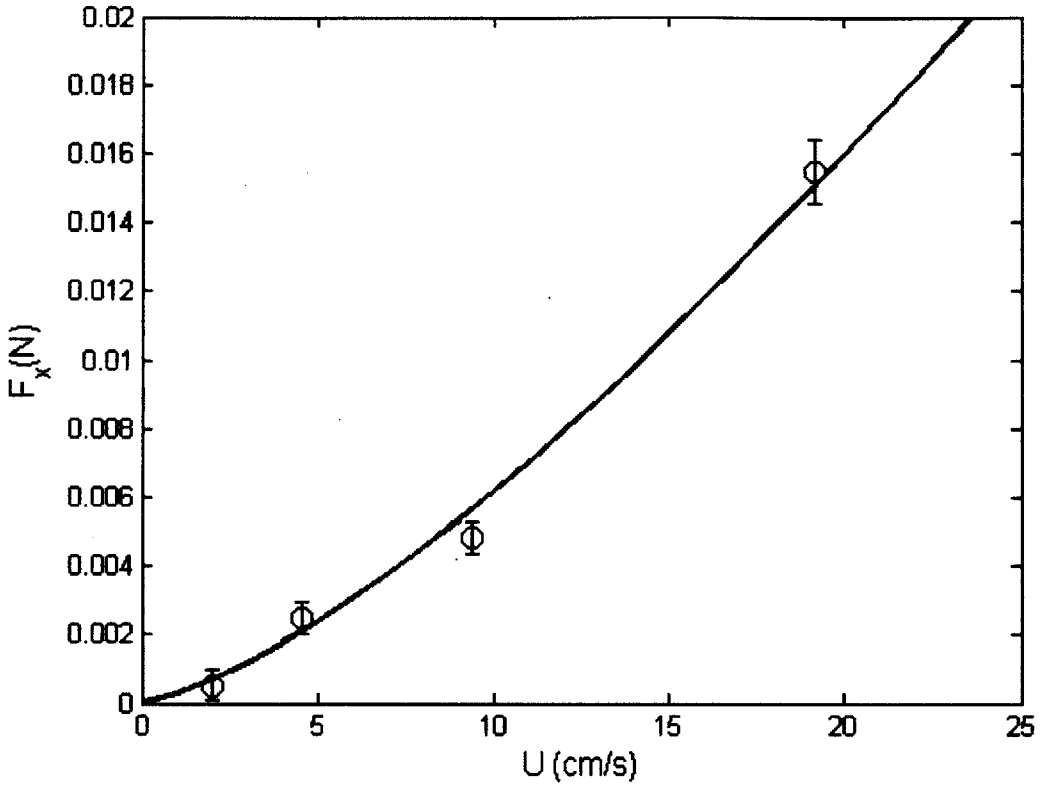

Figure 2-9. Horizontal force on a single blade under different flow rates. Error bars indicate standard deviation in the measurements recorded for a duration of 2 minutes at each flow rate. The solid line is the best fit scaling law function ($y = 2.7e\text{-}4 * U^{1.4}$).

2.3.2 Wave Experiments

The motion of the blades during a wave cycle can be seen in Figure 2-10. For the small amplitude wave (T_w = 2 s, a = 1 cm, U_w = 6.2 cm/s), all blades remain mostly upright during the entire wave cycle. The thick blade and short blade had noticeably less motion than the long, thin blade at all velocities. While the thick and short blades (Ca < 15) moved more in the large amplitude wave (T_w = 2 s, a = 4 cm, U_w 18.9 cm/s), they still remained mostly upright. The long, thin blade clearly moved differently than the stiff blades bending and swaying with the flow. The wave excursions, A_w ($= U_w T_w / 2\pi$), for the low and high amplitude waves were 2.0 cm and 6.0 cm, respectively. Keeping that in mind while examining Figure 2-10 (c) and (d), it can be seen that the same approximate distance is

covered by the tip of the long, thin blade suggesting that the blade tip moves passively with the fluid such that $u_{rel} = 0$ at the blade tip. For the long, thin blade, Ca = 67 and 380, and the ratio of blade length to wave excursion, $l/A_w = 7.5$ and 2.5, respectively. For this parameter range (Ca > 15 and $l/A_w > 1$), we expect the blades to be in the regime pictured in Figure 2-3 (b) which is confirmed by the observed blade behavior ($u_{rel} < U_w$). In all cases (Figure 2-10 (a)-(f), the frequency of blade motion matched the frequency of the operative wave motion.

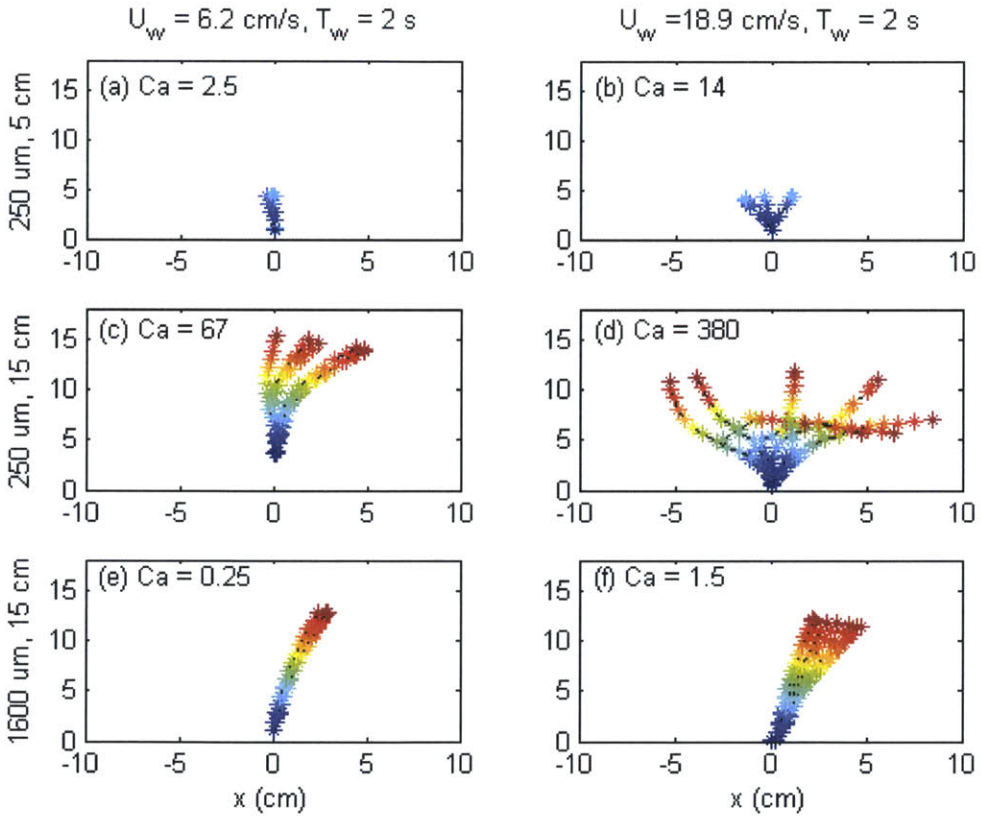

Figure 2-10. Series of still images of the blades during one wave cycle superimposed to illustrate blade motion. The colored markers show a particular blade location identified by the algorithm and tracked in time. Traces are 0.33 s ($T_w/6$) apart.

A more rigorous determination of the relative motion was also carried out (Figure 2-11). Because the wavelength (~3.5 m) was much larger than the depth, the waves are best described as shallow water waves with a depth invariant wave excursion. Therefore,

the relative motion for each of the blades was calculated using Equation 2.3 along the length of the blade assuming A_w does not vary with vertical coordinate. For all of the blades, the relative motion approaches U_w near the fixed base of the blade and is smallest at the blade tip. The long, thin blade which had the highest Ca for each wave condition showed the least amount of relative motion with a depth-average U_{rel} of 3.2 cm/s and 10.4 cm/s for U_w equal to 6.2 and 18.9 cm/s, respectively. Strikingly, the short thin blade and long thick blade collapse together for both velocities. The short thin, blade and long, thick blades showed the greatest overall relative motion with a blade-length averaged value of 5.8 cm/s and 17.4 cm/s for U_w equal to 6.2 and 18.9 cm/s, respectively. Figure 2-11(b) shows that the blades with similar Ca have a similar fractional reduction of u_{rel} from the rigid case, U_w. Specifically, blades with Ca < 15 collapse together and blades with Ca > 15 collapse together. The change in blade behavior due to a threshold Ca indicates that Ca accurately predicts the effective stiffness of blades. The very little relative motion seen for the short thin blade confirms that adjusting Ca by adjusting the length is an effective means for tuning the dynamic behavior of the blade without having to adjust the thickness. The ability to adjust the stiffness using blade length proved to be a useful tool for subsequent flux measurements which could only be carried out with the thinner LDPE.

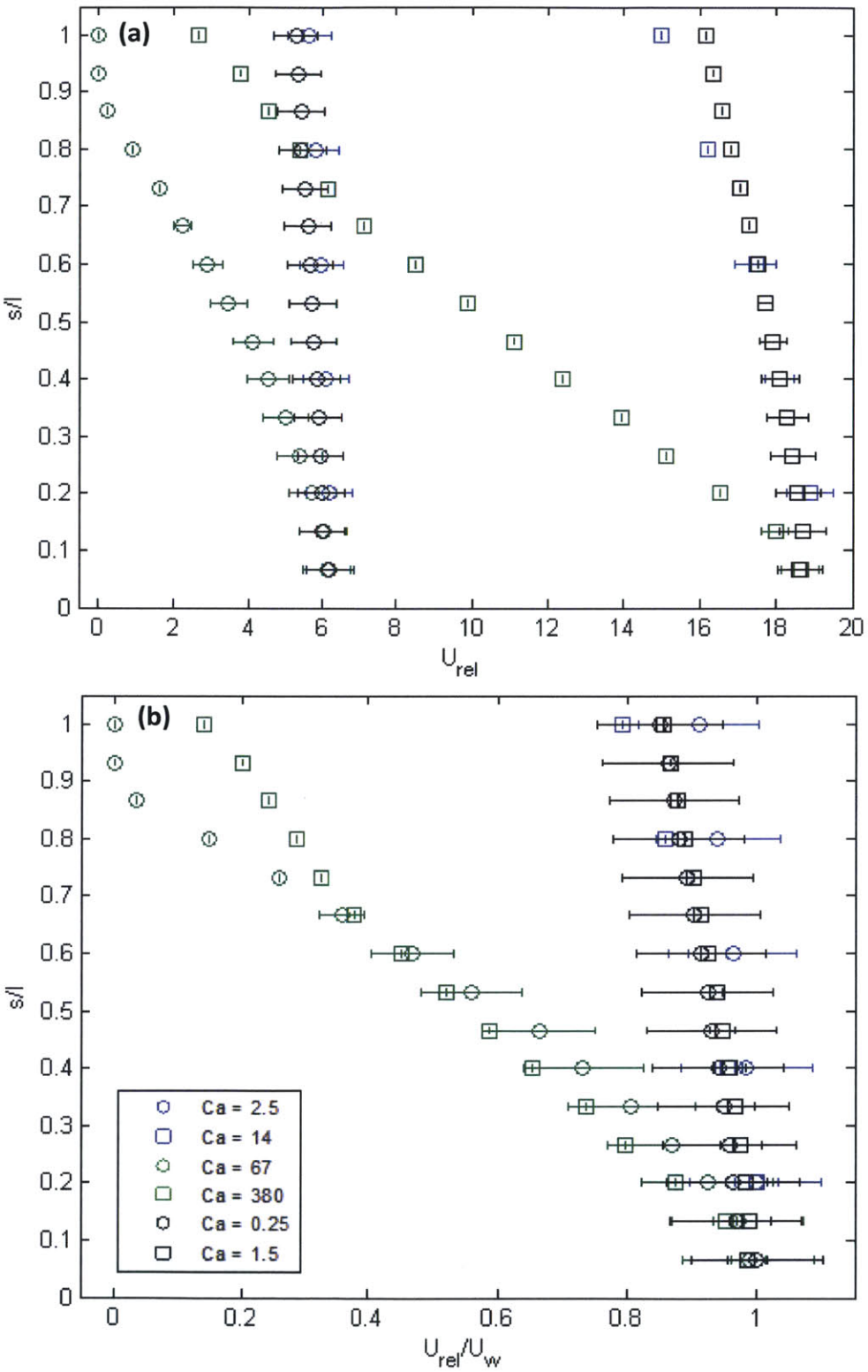

Figure 2-11. The relative motion of the blades shown for each of the blade locations normalized by the blade lengths. Data from large waves conditions (U_w = 18.9) and small wave conditions (Uw = 6.2) are indicated by squares and circles, respectively. Results are also distinguish by blade: long, thin blades (green), short, thin blades (blue), and long, thick blades (black). The same data versus the relative velocity normalized by the peak wave velocity in shown in subplot (b).

Table 4.6 Measured blade-length averaged relative velocity						
Ca	0.25	1.5	2.5	14	67	380
$\mathbf{U_{rel}/U_w}$	0.920	0.932	0.959	0.906	0.518	0.542

To further describe the impact of the scaling parameters on the blade regime, the blade tip excursion normalized by the blade length is shown as a function of Ca in Figure 2-12. As previously discussed, the drag coefficient used to estimate Ca was calculated using the relationship $C_d \sim KC^{-1/3}$. Therefore, the figure can also be interpreted as the variation in blade excursion with $KC^{-1/3}$. The solid line in the figure shows, for comparison, the excursion predicted according to Equation 2.4. The data agrees with this prediction for $Ca < 10$, after which it levels out at an excursion approximately equal to the blade length, which is the obvious physical limit, i.e. the blade excursion cannot exceed the blade length. The agreement between the data and the prediction supports the assumptions made in deriving the prediction, namely, that buoyancy force is negligible and the blade acts as a beam bending under a uniform load (form drag). The deviation between the data and the prediction for $Ca > 10$ lends further evidence to a transition from the blade regime shown Figure 2-3 (a) to the regime in Figure 2-3 (b) at this value for Ca. Recall that larger Ca occurs for either a more flexible blade (smaller EI) or a larger drag force (larger U_w). Beyond the critical Ca the force on the blade overcomes the blade's effective stiffness and the blade moves in sync with the waves. While the third regime (Figure 2-3 (c)) was never observed in these experiments, it was the majority of cases in the work by Zeller et al (2013). In this case, the wave excursion greatly exceeds the blade length, and the normalized blade excursion remains at the physical limit, 1. However, the blade is pronated

early in the wave cycle, and the assumption of small bending angles used in formulating the prediction is no longer valid.

The qualitative picture of blade motion, u_{rel}, and blade tip excursion all show that a blade with Ca < 10 can be considered to be in the regime in which the blade remains mostly vertical in the flow and the relative velocity is comparable to the wave velocity (Figure 2-3(a), Figure 2-10 (a-b) and (e-f)). For Ca > 10, the blades are in the second regime (Figure 2-3(b), Figure 2-10 (c-d)) in which the relative velocity is less than the wave velocity, which reduces the drag.

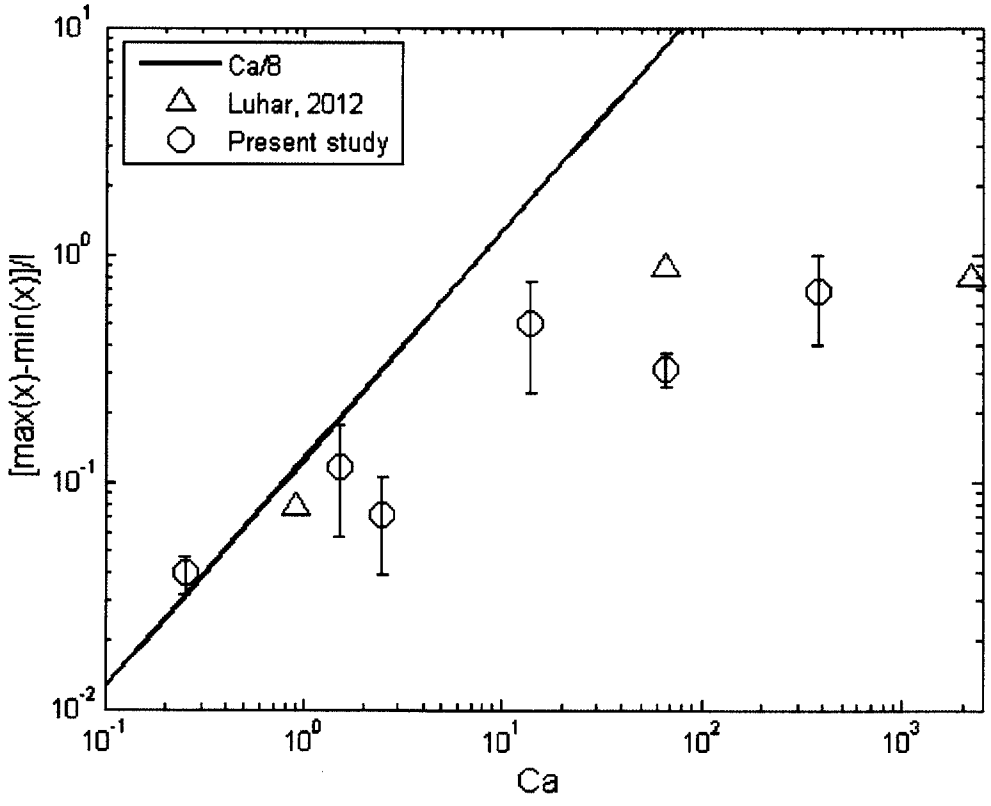

Figure 2-12. Blade tip excursion normalized by blade length and shown versus Cauchy number.

2.4 CONCLUSIONS

The behavior of model seagrass in unidirectional and oscillatory flow conditions was observed. In accordance with previous studies (Ghisalberti and Nepf, 2002; Luhar and Nepf, 2011), the model seagrass met the requirement of dynamic similarity to real seagrass. For the unidirectional case, the deflected blade tip height gradually decreased with increasing velocity. Although there was somewhat higher variability in blade posture at low velocities, heterogeneity in model construction material (LDPE) likely accounts for these differences. The horizontal force followed expected scaling with $F_x \propto U^{3/4}$. This scaling corresponds to a blade streamlined in flow with negligible buoyancy and Ca ≥ 2.5.

In oscillatory flow conditions, the relative motion of blades was successfully extracted from videos of blades. The ability to manipulate the effective stiffness of the blades using blade length and thickness was demonstrated. The ability to do so relates directly to the Cauchy number calculated with a KC dependent drag coefficient. This dimensionless number, Ca, proved to be an effective means for predicting blade excursion and consequently the regime for relative motion. In all cases, the wave excursion was on the same order of magnitude as the blade length so that blades fell into one of two possible regimes: nearly stationary blades with $u_{rel} \rightarrow U_w$ (Ca < 15), and blades for which reconfiguration occurs continuously through the wave cycle with $u_{rel} \rightarrow 0.5U_w$ (Ca > 15).

In both cases, the physical blade characteristics are critical for determining the dynamic response of the blade to the flow. The blades show a substantial deviation from the behavior of a flat plat either perpendicular or parallel to flow. Consequently, we hypothesize that the most significant physical mechanisms for mass and momentum transfer occur as a result of the blade normal components of the flow. A reduced

dependence on the velocity occurs for the drag force on the blades in unidirectional currents. Mass transfer processes may be similarly less dependent on the velocity as a result of streamlining in flow. For oscillatory conditions, the relative motion between the blade and fluid best describes the normal component of velocity. Again, it has been shown that this results in an alteration of the drag force dependence on velocity (Luhar, 2012). The next chapter explores more directly the relation between blade physical characteristics, flow conditions and mass flux.

CHAPTER 3. FLUX EXPERIMENTS USING DIBROMOCHLOROMETHANE

3.1 INTRODUCTION

Low-density polyethylene provides a convenient model to study fluid-plant interactions relevant to aquatic vegetation. It is based on a method called passive sampling, which is used by environmental scientists to determine pollutant levels in soil, water and air. As described by Adams et al (2007), many hydrophobic organic compounds partition into low-density polyethylene (LDPE) from water. The amount that accumulates in the LDPE is a function of the chemical- and matrix-specific partition coefficient with water (K_{PEw}). The partition coefficient describes the tendency for a chemical to be found in one phase relative to another, in this case the tendency to be found in PE relative to water. The partition coefficient, which is also sensitive to temperature and salinity, is defined at equilibrium by the ratio of the concentrations in the two phases ($K_{PEw} = C_{PE}/C_w$).

Passive sampling deploys LDPE in the field where it takes up the chemical of interest in proportion to the background concentration. By measuring the resultant concentration in the LDPE, the background concentration can be calculated using K_{PEw}. However, large organic compounds can take on the order of months to reach equilibrium, which makes it impractical to wait for equilibrium conditions in the field. To work around this limitation, the loss of a reference compound impregnated in the passive samplers before deployment is also monitored. Assuming the reference compound is controlled by the same mass transfer limitations, the approximate deviation from equilibrium can be calculated for both the reference compound and compound of interest. Improvements on the first order approximations were made by Fernandez et al (2009), who took into account differences in diffusivities and partition coefficients between the reference and

target compounds using a one-dimensional diffusion model. Even with the use of reference compounds, the technique still requires deployment times of days to weeks to obtain measurable amounts of the target compounds. As a result, this approach provides time-averaged concentrations, and is not used to distinguish between changes in the environment that occur over shorter timescales. This chapter describes an adaptation of the passive sampling technique designed to measure the mass accumulation in model seagrass blades made of LDPE.

In the study of seagrass and other submerged aquatic vegetation (SAV), gaps exist in our understanding of the mechanisms controlling the physical transport of dissolved chemicals to the blade surface. Previous experiments observing the uptake of nutrients by seagrass suggest biological mechanisms can also control uptake for some environmental conditions (see discussion in Chapter 1). Isolating and clarifying the physical mechanisms influencing chemical uptake by flexible structures could greatly benefit the study of live macrophytes, by providing a way to tease apart the physical limitations to flux from the biological limitations. Employing LDPE as model seagrass for the study of chemical uptake provides an elegant means for doing so. Previous studies discussed in Chapter 2 of this work have already shown that LDPE mimics seagrass motion in response to flow in both unidirectional and oscillating flow conditions. In this chapter, flux experiments are described in which the uptake of an organic compound by LDPE in different flow conditions was monitored. The results are compared to predictions made using proposed flux models, namely, the flat plate model, the surface renewal model, and the Ledwell model (see Chapter 1 for details of each model). Hopefully, insights gained can be used to

improve both the study of seagrass nutrient uptake and applications of passive sampler technology.

3.2 FLUX MODELS

Ideally, the LDPE would act as a perfect sink for the chemicals so that it would imitate conditions in which the rate of biological uptake greatly exceeds the mass transfer rate in the water, making the mass transfer rate the controlling step for flux. In reality, the LDPE is not a perfect sink. Specifically, the rate of uptake by the LDPE is a function of the rate of diffusion within the blade, which is influenced by the target chemical's physical properties, specifically the diffusion coefficient within the LDPE (D_{PE}) and the partition coefficient (K_{PEw}).

Because the timescale for diffusion across the thickness (h) of the blade is much smaller than the timescale for diffusion across the length (l) or width (b) of the blade ($h^2/D_{PE} << b^2/D_{PE} << l^2/D_{PE}$), we can consider the chemical diffusion into the blade as a one-dimensional problem in the coordinate defining the blade thickness, namely z. Following the approach taken by Fernandez, Harvey and Gschwend (2009), a one-dimensional diffusion model is formulated as a boundary value problem and solved in the Laplace domain. The governing equations for the time-varying concentration in the LDPE and water boundary layer are

$$\frac{\partial C_{PE}}{\partial t} = D_{PE}\frac{\partial^2 C_{PE}}{\partial z^2}, \qquad for\ -h/2 < z < h/2 \tag{3.1}$$

and

$$\frac{\partial C_w}{\partial t} = D_w\frac{\partial^2 C_w}{\partial z^2}, \qquad for\ z < -h/2\ and\ z > h/2 \tag{3.2}$$

where h is the blade thickness, C_{PE} is the concentration within the LDPE, D_{PE} is the diffusion coefficient within the LDPE, C_w is the concentration within the water boundary layer, and D_w is the diffusion coefficient within the water. The variable z is the coordinate across the blade thickness defined as zero at the centerline of the blade and equal to h/2 at the edge of the blade. The boundary conditions are as follows:

$$D_{PE}\frac{\partial C_{PE}}{\partial z} = 0, \qquad for\ z = 0 \tag{3.3}$$

$$D_{PE}\frac{\partial C_{PE}}{\partial z} = D_w\frac{\partial C_w}{\partial z}, \qquad for\ z = \pm h/2 \tag{3.4}$$

The first boundary condition arises from the symmetry of the problem about the blade centerline (z = 0). The boundary condition at z = ±h/2 assumes that the flux into the LDPE is matched by the flux from the bulk fluid to the surface (i.e. no accumulation). In addition, the concentrations at the PE-water interface are constrained by the local equilibrium set by PE-water partition coefficient, K_{PEw},

$$C_{PE} = K_{PEw}C_w, \qquad for\ z = \pm h/2 \tag{3.5}$$

Deviating from the solution in Fernandez et al (2009), Tcaciuc et al (2014) defined the outer boundary condition using the diffusive sub-layer thickness (δ_D). Effectively, the model assumes chemical flux within δ_D occurs through molecular diffusion, but in the fluid domain beyond δ_D (e.g. z> h/2 + δ_D) turbulent diffusion is sufficiently strong to maintain a uniform, background concentration, $C_{w,\infty}$, i.e.

$$C_w = C_{w,\infty}, \qquad for\ z = \pm\left(\frac{h}{2} + \delta_D\right) \tag{3.6}$$

Below I describe how each of the flux models describing the transport of the chemical from the bulk to the blade surface (flat plate, surface renewal, and Ledwell) can be used to predict an effective diffusive sub-layer thickness, $\delta_{D,eff}$, to use in Equation 3.6. With these

boundary conditions and the initial condition $C_{PE} = 0$ for $-h/2<z<h/2$, Tcaciuc et al (2014) found a solution to Equations 3.1 and 3.2 in the Laplace domain, and, after integrating the concentration over the blade thickness, the mass of compound in the LDPE (M) is expressed as a fraction of the equilibrium mass (M_{sat}).

$$\frac{M}{M_{sat}} = \frac{1}{s\sqrt{s}} \frac{1}{coth\sqrt{s} - K_{PEw}/\sqrt{\psi}\tanh(-\alpha\sqrt{\frac{s}{\psi}})} \tag{3.7}$$

In this equation, s is the Laplace domain variable based on a dimensionless time ($\hat{t}=4tD_{PE}/h^2$), ψ is the ratio of diffusivities (D_w/D_{PE}), and α is the ratio of the sub-layer thickness to half the thickness of LDPE ($2\delta_{D,eff}/h$). A Matlab code created by Hollenbeck (1998) and based the de Hoog algorithm was used to invert Equation 3.7 from the Laplace domain into the time domain.

In the next few paragraphs I consider how the flux models presented in Chapter 1 can each be used to describe an effective diffusive sub-layer, $\delta_{D,eff}$, that can be used within Equation 3.6 to predict chemical uptake. From boundary layer theory over a flat plate,

$$\delta_{D,eff} = 5\upsilon/u_* Sc^{-1/3} \tag{3.8}$$

The friction velocity on the plate, u_*, is a function of the free-stream velocity, U. Specfically, u^*/U is a constant generally between 0.05 and 0.1, depending on the roughness of the surface. After sufficient time ($t > T_D = \delta_{D,eff}^2/D_w$), the concentration profile within the diffusive sub-layer becomes linear between the surface concentration ($C_w(z = 0)$) and the bulk concentration ($C_{w,\infty}$), and we can define a constant transfer velocity,

$$k = \frac{D_w}{\delta_D} \tag{3.9}$$

The surface renewal model does not assume that the sub-layer thickness is constant. Instead, periodic motion drives fluid from outside the sub-layer to the blade surface every T seconds. The time-averaged enhancement of the flux due to this renewal is summarized in Equation 3.10 (Stevens and Hurd, 1997).

$$\bar{k} = \left(\frac{D_w}{\delta_D} + \frac{2\delta_D}{T}\sum_{n=1}^{\infty}\frac{1}{n^2\pi^2}\left(1 - exp\left(-n^2\pi^2\frac{D_w}{\delta_D^2}\right)\right)\right) \tag{3.10}$$

The third model was originally conceived by Ledwell (1980), and so we refer to it as the Ledwel model. In this model, the transport of scalars to the water-blade boundary is dominated by eddy diffusivities set by the turbulent component of the velocity field that is perpendicular to the surface, which, in turn, scales with the divergence tangent to the surface. Rominger and Nepf (2014) further simplified the model by assuming the divergence scales as the relative velocity divided by the width of the blade, which is consistent with studies of flow normal to bluff objects (Koumoutsakos and Shiels, 1996, Sparrow et al, 1979). The Ledwell model is then expressed here as Equations 3.11 and 3.12.

$$\bar{k} = \frac{3\sqrt{3}}{2\pi}\beta^{1/3}D_w^{2/3} \tag{3.11}$$

Where,

$$\beta \approx \left.\frac{\partial \nabla \cdot v'}{\partial z}\right|_{z=0} = \frac{\partial^2 w'}{\partial z^2} \approx \frac{u_{rel}}{b^2} \tag{3.12}$$

To compare the models, I frame each in terms of an effective sub-layer thickness. While this approach is not physically realistic for all models, it makes comparison between models easy, because all three models can be interpreted based on the intuitive understanding that a smaller $\delta_{D,eff}$ is associated with a higher flux. For the flat plate model,

the original definition of the diffusive sub-layer is retained (Equation 3.8) and $u_* = 0.05*U$ is assumed, with U parallel to the flat plate.

For the other models, the effective sub-layer thickness is calculated by substituting for k into Equation 3.9 and rearranging, yielding:

$$\delta_{D,eff} = \frac{D_w}{k} \tag{3.13}$$

For the surface renewal model, substituting Equation 3.10 into Equation 3.13 gives the following effective boundary layer thickness.

$$\delta_{D,eff} = D_w \left(\frac{D_w}{\delta_D} + \frac{2\delta_D}{T} \sum_{n=1}^{\infty} \frac{1}{n^2\pi^2} \left(1 - exp\left(-n^2\pi^2 \frac{D_w}{\delta_D^2} \right) \right) \right)^{-1} \tag{3.14}$$

Substituting Equation 3.11 into 3.13 yields the following effective boundary layer thickness for the Ledwell model.

$$\delta_{D,eff} = \frac{2\pi}{3\sqrt{3}} \left(\frac{u_{rel}}{b^2} \right)^{-1/3} {D_w}^{-2/3} \tag{3.15}$$

Figure 3-1 provides a graphical comparison of the three models and highlights important differences. The effective diffusive boundary layer thickness is shown as a function of the characteristic velocity (U), which can be interpreted as the current or peak velocity for waves (U_w). The blade widths were chosen to encompass typical values for seagrass (~ 1 cm) and other SAV, such as kelp (~ 10 cm). The velocities cover a range typically experienced by SAV in the field, albeit excluding more extreme examples such as storm events, which can exceed 50 cm/s. The disturbance periods (T) include possible disturbance periods relevant to aquatic vegetation, e.g. associated with waves (T = 2 s (wind waves) to 20 s (swell)), and disturbance periods that highlight specific model behavior. At higher velocity and longer renewal time, the surface renewal model

approaches the flat plate boundary layer model, which decreases slowly with increasing U. However, flux is enhanced (smaller $\delta_{D,eff}$) by the renewal periods in the wave-related range (T = 1 and 10 s), over the full velocity range considered. This suggests that at current speeds U < 20cm/s, wave action is beneficial in elevating flux. This is consistent with the more detailed evaluation by Huang et al (2011, Figure 7 of that paper), who showed that wave-related disturbances (1 to 20 s) provide flux enhance for current speed below 20 cm/s, but provide no flux enhancement in currents above 1 m/s. In between (20cm/s to 1 m/s), there is a frequency dependent transition, with benefit from shorter period waves persisting to higher currents. At very low velocity (U < 4 cm/s), $\delta_{D,eff}$ grows rapidy with decreasing velocity and even relatively long renewal timescales (T = 1000 s in Figure 3-1) result in flux enhancement (diminished $\delta_{D,eff}$). Also seen in Figure 3-1 is the significant impact of blade width on the Ledwell model in comparison to other models. The Ledwell model yields a higher flux only at low velocity (U < 5 cm/s). For U > 5 cm/s, Figure 3-1 indicates that blades with b ~ 1 cm (such as many seagrass species) will still have higher flux than a flat plate according to the Ledwell model, whereas wider blades (such as kelp) may actually have a lower flux according to this model.

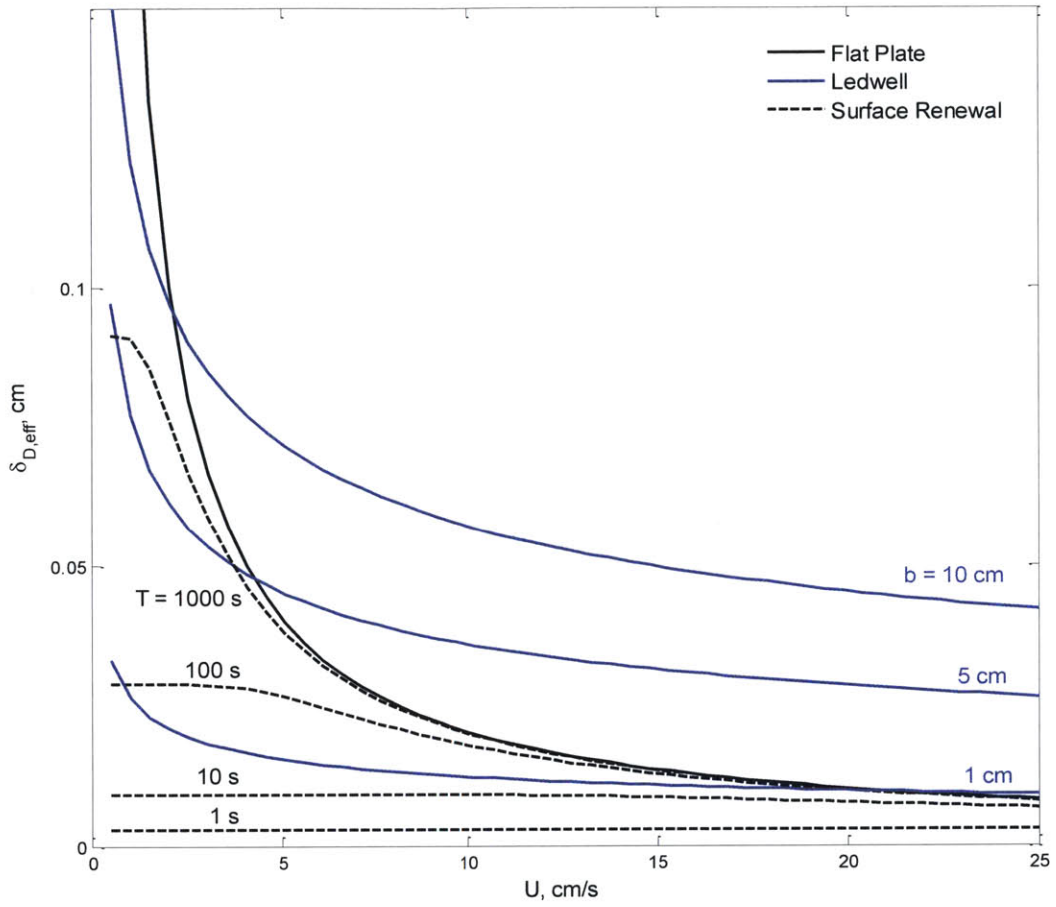

Figure 3-1. Dependence of the effective boundary layer thickness on characteristic velocity. Blue lines indicate the effective thickness based on the Ledwell model (Eq. 3.15) for different blade widths. Solid black line is the boundary layer thickness based on the friction velocity (Eq. 3.8). Dashed lines show the effective boundary layer thickness calculated using the surface renewal model (Eq. 3.14) for different renewal periods.

When calculating $\delta_{D,eff}$ for the Ledwell model using Equation 3.15, U is substituted for u_{rel} whose relationship to U_w changes depending on the blade behavior, as discussed in Chapter 2. Consequently, when considering the Ledwell model, the regime of the blade motion must be taken into account. Consider a very rigid blade (Ca< 15) in oscillatory flow. The blade would remain upright for most of the wave cycle and $u_{rel} \sim U$ as pictured on the far left of Figure 3-2. As a result of the blade's posture, the flat plate model does not apply.

The Ledwell model could apply, using $u_{rel} = U$. In the case of a very flexible blade (Ca > 15) in oscillatory flow with a wave excursion comparable to the blade length (the center scenario in Figure 3-2), the blade will move passively, and $u_{rel} < U$. The relative velocity could be estimated using observations of the blade excursion (x_{BE}) and Equation 2.3.

A third regime is possible under long wave conditions, shown on the far right in Figure 3-2. In this case, the wave excursion is much greater than the blade length. Especially for flexible blades, the blade will reconfigure to its stream wise position very early on in the wave cycle, again yielding $u_{rel} \sim U$. Over most of the wave cycle most of the blade is positioned parallel to the flow, so that the flat plate model may be applicable. However, the Ledwell model will not apply, because there is little or no blade normal velocity. Because $\delta_{D,eff}$ for the flat plate model is always greater than or equal to $\delta_{D,eff}$ for the surface renewal model, the effective diffusive boundary layer thickness determined using the flat plate model is the theoretical maximum for the mass transfer-limited situation across a diffusive sub-layer in this third regime. Stevens and Hurd (1997) observed an effective boundary layer thickness larger than this theoretical maximum (Equation 3.8) especially at velocities above 6 cm/s using the data collected by Hurd et al (1996) who measured the uptake of nitrate and ammonium by the kelp *Macrocystis integrifolia* (b = 13.4, 8.9 cm) using individual blades held horizontally in flow. They conclude that the results indicated a "reduced apparent velocity" and point out a number of potential complications such as a dependence of u_*/U on U and boundary layer separation resulting in a flow-independent boundary layer thickness. Alternatively, flapping motions of the blades in flow may have caused relative motions to dominate the flux, which result in a larger effective sub-layer thickness for U > 5 cm/s for the 13.4 cm and 8.9 cm wide kelp

blades. Otherwise, our analysis indicates that an effective boundary layer thickness exceeding the flat plate model is unlikely for a pronated blade and results to the contrary suggest that the flux may, in fact, have been biologically limited.

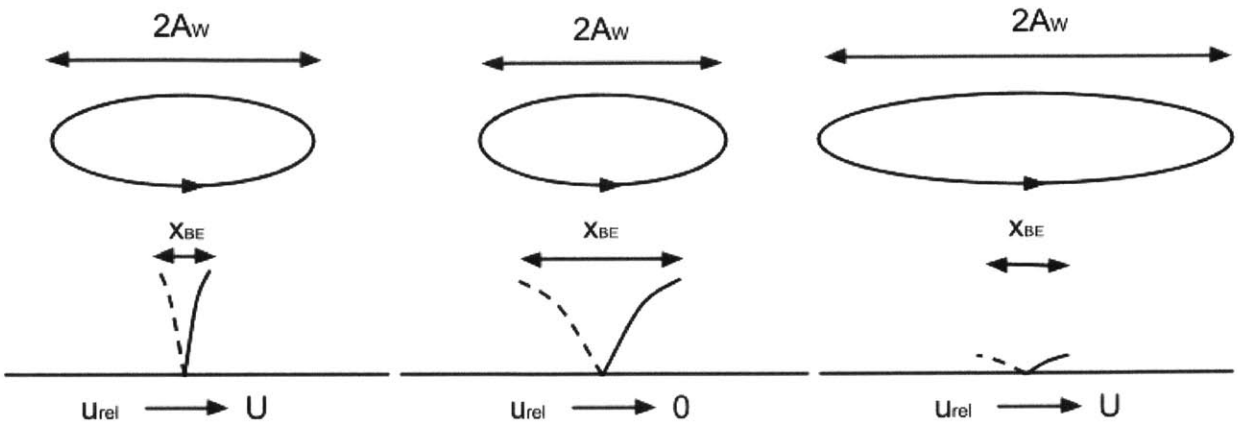

Figure 3-2. Different possible regimes for blades in oscillatory flow

3.3 METHODS

3.3.1 Flux Experiments

Model seagrass blades were fashioned from 0.25 mm LDPE sheeting. 1 cm wide blades were cut to lengths of 15 cm or 5 cm from 0.25 mm thick LDPE with Young's modulus of 0.3 GPa and density of 0.925 g/cm^3 (Ghisalberti and Nepf, 2002). The different lengths of model blades allowed testing of a range of dynamic behavior typical to seagrass observed in the field and relevant to physical regimes in mathematical parameter space (See Table 2.1). Blades were cleaned using the procedure described below and stored in clean water. We carried out experiments in a 24 m long, 38 cm wide flume filled to 38 cm depth. Blades were mounted using a metal clamp on an acrylic ramp where depth was reduced to 25 cm and the velocity field compressed to make it more uniform across the

depth. At the start of a set of experiments, approximately 130 μL $CHBr_2Cl$ (Acros Organics) was injected directly into the flume near the pump inlet. The pump was run at maximum speed for a minimum of 30 min to insure a uniform concentration of approximately 80 ppb $CHBr_2Cl$ throughout the flume. See Appendix A for a justification of the flume mixing time. In order to prevent loss of the volatile chemical over the course of the experiment, the entire length of the flume was covered with aluminum foil. Background concentrations obtained throughout the experiments confirmed minimal decay of the chemical concentration in the flume water. Both unidirectional and wave only conditions were examined.

For unidirectional experiments, the flow rate was set using a recirculating pump with a controller. The velocities tested included 0, 5.3, 10.3, 20.7 and 39.6 cm/s, measured using a 3D Nortek Vectrino Acoustic Doppler Velocimeter (ADV). For each flow rate, different blades were exposed for 180, 360, and 720 s resulting in a total of 15 samples. All blades exposed to unidirectional flows were 15 cm in length resulting in Ca numbers ranging from 3.0-1200 due just to the variation in velocity.

Wave conditions were achieved using a paddle wavemaker controlled with a programmable signal generator (Syscomp WGM-101). With water depth, desired frequency and amplitude as inputs, an appropriate waveform for the signal generator was created using the code developed by Luhar (2012) based on the closed form solution for piston movement. Waves with a period of 2 seconds and amplitude of either 1 cm or 4 cm were generated resulting in a peak wave velocity, U_w, of 6.2 cm/s (KC = 12.4) and 18.9 cm/s (KC = 37.8), respectively, measured with an ADV placed 10 cm above the center of the ramp. A large 'beach' was placed at the end of the flume to reduce that reflection of waves off the

back wall. Both 15 cm long and 5 cm long blades were exposed to wave conditions, all of which were placed in the flume for 360 s. The wave conditions combined with model blade physical characteristics resulted in Ca numbers ranging from 0.25-380 and shown in Table 2.1 in comparison to actual seagrass. The specific Ca numbers for each blade length and wave condition are provided in Table 2.3.

For all experimental conditions, a blade was placed in the flume for the prescribed amount of time, removed, dried with a kimwipe (Kimtech) to remove excess flume water, and placed in a clean 40 mL glass amber vial (Qorpak) with clean milliQ water (18 MΩ). After each blade was removed, a flume water sample was taken and used to monitor the background concentrations in the flume ($C_{w,\infty}$). The blade samples were then placed on a shaker table at room temperature for 10 days to reach equilibrium. Previous experiments of $CHBr_2Cl$ and LDPE showed that 7 days is sufficient to reach equilibrium after observing no change in the concentration measured from vials with the same starting concentration of $CHBr_2Cl$ and mass of LDPE left on the shaker table for 7 and 21 days (Rominger, 2013). Because the vial water and LDPE is assumed to have reached equilibrium, the measured concentration of the vial water is used to determine the mass of $CHBr_2Cl$ in the strip at the time it was placed in the vial using Equation 3.16. The total mass in the vial after equilibrium (right-hand side) equals the total mass originally in the blade (left-hand side).

$$M_{PE} = K_{PEW} C_{W,vial} V_{PE} + C_{W,vial} V_W \quad (3.16)$$

Where V_w is the volume of water, V_{PE} is the volume of LDPE, and $C_{w,vial}$ is the concentration in the water in the vial measured after equilibrium has been reached. Equation 3.16 divided by the saturated mass uptake ($M_{sat} = C_{w,o} K_{PEw} V_{PE}$), results in the following equation for the ratio of mass uptake to saturated mass.

$$\frac{M_{PE}}{M_{sat}} = \frac{C_{w,vial}(V_w + K_{PEW}V_{PE})}{C_{w,o}K_{PEW}V_{PE}} \quad (3.17)$$

3.3.2 LDPE Preparation

All LDPE used in experiments described in this chapter were first cut to the desired length from the same roll of 250 μm film (McMaster) stored at room temperature. The strips were cleaned by twice soaking them for at least 24 hours in dichloromethane, twice in methanol and twice in clean milliQ water (18 MΩ), where they were stored until use in experiments.

3.3.3 Concentration Measurements

The concentration of $CHBr_2Cl$ in water was measured using gas chromatography (GC) with an electron capture detector (Perkin Elmer Autosystem XL) in combination with a purge and trap system (Tekmar LSC 2000). Calibrations with standard concentrations were obtained for each purge time used.

3.3.4 Determining K_{PEw}

In order to determine the uptake of dibromochloromethane ($CHBr_2Cl$) by LDPE using GC, the partition coefficient must be known. It is dependent on the material, the target chemical, and environmental conditions, especially temperature. Correlations have been developed to determine K_{PEw} using the octanol-water partition coefficient, K_{ow} (Lohmann and Muir, 2010). However, as measured K_{PEw} used in the correlations only included thinner LDPE (50-100 μm) and larger organic molecules, we determined K_{PEw} in a separate experiment for the 250 μm LDPE and smaller organic molecule used ($CHBr_2Cl$). While one approach to obtain K_{PEw} involves measuring the uptake of $CHBr_2Cl$ at known concentrations over time, we were also interested in the potential impact of different sizes

of LDPE in a single volume of water. The partition coefficient is not a function of the length of the LDPE strip, so any significant difference in measured K_{PEw} indicates an experimental limitation. Therefore, an experiment was designed to address both aspects by measuring the partitioning of $CHBr_2Cl$ into different lengths of LDPE after a sufficient time to reach equilibrium has passed.

A known concentration (34 ppb) of $CHBr_2Cl$ was added to 40 mL glass amber vials containing approximately 10, 50, 500, 350, 1000, and 2000 mg of 250 μm thick LDPE. The samples spent 10 days on a shaker table at room temperature to reach equilibrium. Additionally, a control vial containing only water at the same starting concentration was measured after 10 days and confirmed the absence of other sinks such as poor sealing or chemical degradation. The sum of the mass in the water and in the LDPE at equilibrium must be equal to the mass of $CHBr_2Cl$ originally added to the vial in the water. Therefore, the equilibrium water concentration is predicted using the following equation,

$$C_W = \frac{V_w C_{W,i}}{V_w + K_{PEW} V_{PE}} \tag{3.18}$$

where $C_{w,i}$ is the initial concentration in the water at the start of the experiment.

The results of this preliminary experiment are summarized in Figure 3-3. Error bars shown represent the standard deviation in replicate measurements of the same sample on the GC. By adjusting the K_{PEw} value, the best-fit line for the predicted concentrations is calculated using Equation 3.18. A partition coefficient, K_{PEw}, equal to approximately 25 m^3/m^3 is determined as best fitting the data, and the resulting line is shown in the figure. This value is reasonably similar to Lohmann and Muir's (2010) correlation with K_{ow} which predicts K_{PEw} = 48 ($\log K_{ow}$=2.16, EPI Suite). The equilibrium concentrations for the two

largest masses are higher than predicted indicating less mass partitioned into the LDPE than expected. These larger masses were first rolled loosely in order to fit into the vials. It's likely that PE to PE contact within the vial inhibited uptake of the chemical. Subsequent uptake experiments carried out in the laboratory flume only used LDPE that was 350 mg and did not appear to have contact issues within the vial.

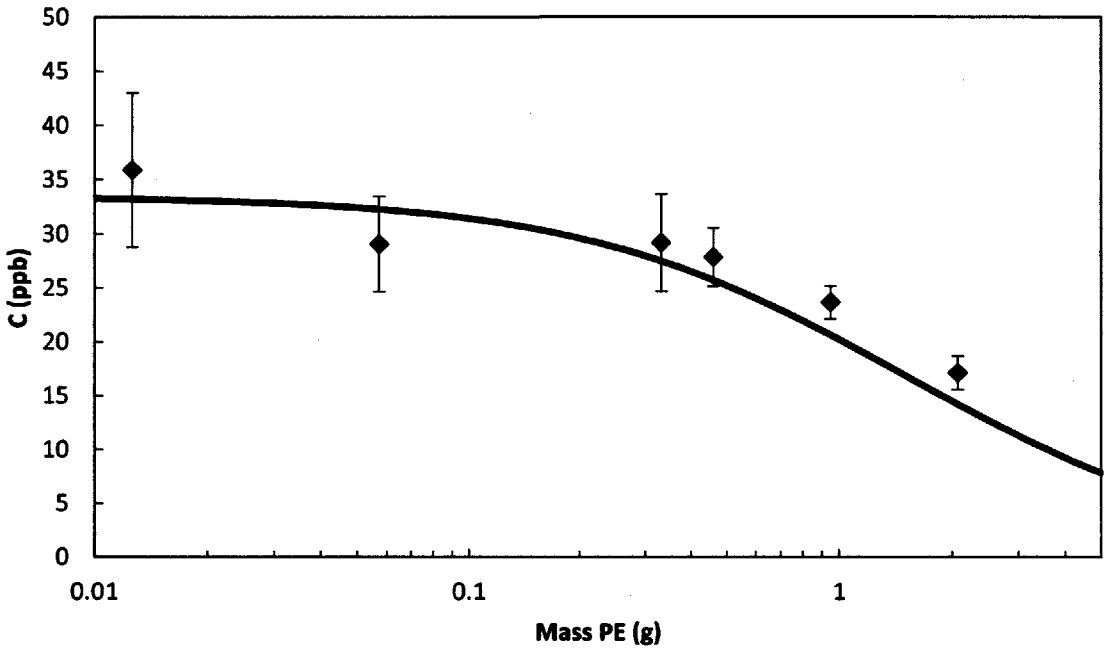

Figure 3-3. Vial water concentrations measured for samples with different masses of LDPE and an initial water concentration of 34 ppb. The solid line shows the calculated vial concentration for K_{PEW} = 25. Table of values provided in Appendix B.

3.3.5 Air Exposure

Flux experiments carried out in the flume required handling LDPE after exposure in the flume. Due to the volatile nature of $CHBr_2Cl$, we characterized the loss of chemical to the air during handling. To achieve this goal, another preliminary experiment was designed in which LDPE samples with a known concentration of $CHBr_2Cl$ were exposed to air in a controlled manner and analyzed for any losses. We cut 250 μm thick LDPE into 3 cm by 30

cm strips and placed them in 40 mL amber vials with a known initial water concentration. These were allowed to equilibrate for 10 days on a shaker table at room temperature. The strips were removed from their vials and exposed to air for times ranging between 15 and 240 seconds. These times were chosen based on typical handling times during the flux experiments. After air exposure, the strips were placed in clean vials with clean water. These samples were again placed on a shaker table at room temperature for 10 days. Two initial water concentrations, 65 ppb and 95 ppb, were used, resulting in two initial amounts of $CHBr_2Cl$ in the LDPE before air exposure. The initial mass of $CHBr_2Cl$ in the LDPE before air exposure, $M_{PE,i}$, is determined from samples containing LDPE that is never exposed to air but still allowed to reach equilibrium with the two initial water concentrations. The concentration of the water in the control samples is measured on the same day the other samples are exposed to air.

Predictions for the loss to the air were made by modeling the diffusion of $CHBr_2Cl$ within the LDPE. Because the length and width of the strip are much larger than the thickness, the flux of $CHBr_2Cl$ across these coordinates is assumed to be negligible. The governing equation results from one-dimensional flux within the strip due to Fickian diffusion across the thickness of the blade. The equation is also given by Equation 3.1. For the case of mass loss to the air, the boundary conditions are as follows:

$$\frac{\partial C_{PE}}{\partial z} = 0, \qquad at\ z = 0 \tag{3.19}$$

$$D_{PE}\frac{\partial C_{PE}}{\partial z} = D_{air}\frac{C_{air}(z = h/2) - C_{air,\infty}}{\delta}, \qquad at\ z = \pm h/2 \tag{3.20}$$

The second boundary condition, Equation 3.20, results from the continuity in fluxes on the LDPE-air boundary. By assuming the ambient concentration in the air, $C_{air,\infty}$, to be

negligible and the concentration of the air right at the surface, $C_{air}(z = h/2)$, to be in equilibrium with the LDPE, Equation 3.20 can be simplified to Equation 3.21 shown below.

$$D_{PE}\frac{\partial C_{PE}}{\partial z} = D_{air}\frac{C_{PE}(z = h/2)}{K_{PEa}\delta}, \qquad at\ z = \pm h/2 \tag{3.21}$$

In this equation, D_{air} is the diffusion coefficient of $CHBr_2Cl$ in air. K_{PEa} is the PE-air partition coefficient, which can be approximated from the air-water partition coefficient as K_{PEw}/K_{aw} (Lohmann, 2012). The air-side diffusion boundary layer thickness, shown here as δ, is taken to be almost negligible (10^{-5} cm) resulting in a maximum loss scenario. With the initial condition that the LDPE is fully saturated, the governing equation is solved numerically in Matlab.

The results of this experiment and numerical model are presented in Figure 3-4. Mass losses ranged from 0% to 40%. Error bars in the figure represent 30% error based on typical measurement variability in the concentrations measured on the GC and propagated through the ratio of final to initial mass. The losses from the lower starting concentration were zero within uncertainty for all times. However, the losses from the higher starting concentration were on the order expected from the numerical model. Within experimental error for both cases, the mass loss seen after 15 seconds of exposure was indistinguishable from the mass loss after 240 seconds. Additionally, for all but one instance, there was no difference in fractional mass loss depending on the initial concentration. Amongst all samples, an average of 15% of the original mass was lost due to handling.

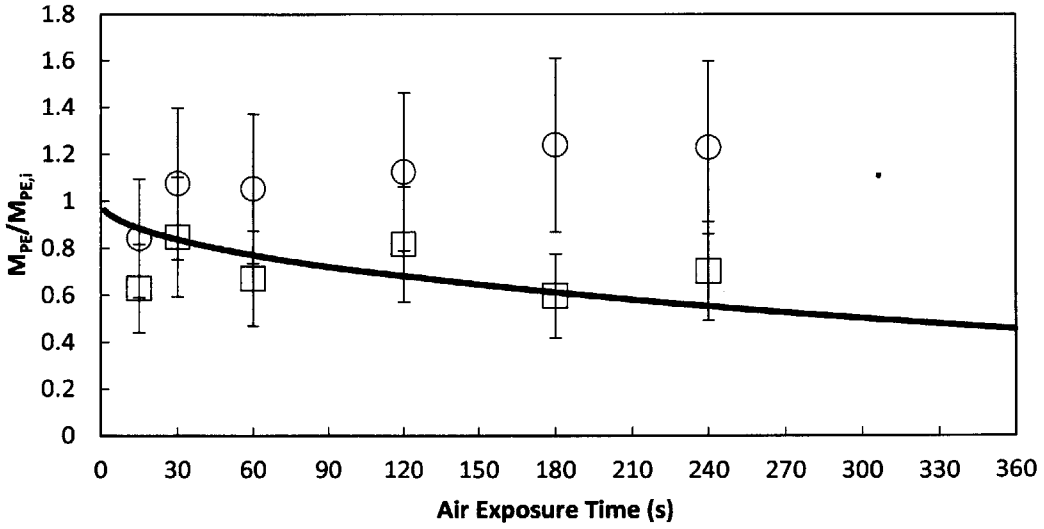

Figure 3-4. Mass loss due to exposure to air for fully saturated LDPE strips. The solid line indicates the results of the numerical model, the circles show results for C_o=65 ppb and the squares show results for C_o=95 ppb. Table of raw measured data provided in Appendix B.

3.5 RESULTS

3.5.1 Current Experiment

Figure 3-5 shows the results of the flux experiments for blades exposed to $CHBr_2Cl$ in a flume with U = 0 cm/s for 180 s, 360 s, and 720 s. The mass uptake in the LDPE increases from 3.8 to 5.5 % of the saturated mass with longer exposure times. For the zero velocity case, the diffusive sub-layer could not be predicted from the flat-plate boundary layer theory, $\delta_D = 5\upsilon/u_* Sc^{-1/3}$, because $u_* = 0$ yields an infinite δ_D. However, one important feature of the model (Equations 3.1 and 3.2) is that there is an upper limit to the thickness of the boundary layer beyond which the thickness no longer affects the mass uptake. This limit is determined by the timescale for diffusion through the water-side boundary layer ($T_D = \delta_D^2/D_w$). As long as this timescale is much greater than the timescale of interest (i.e. blade exposure time), then the model results are not significantly impacted by the choice of δ_D. Therefore, I chose an arbitrary, but large, value for δ_D (10^{15} cm) which

met this requirement for all exposure times considered with U = 0 cm/s. The diffusion coefficient for $CHBr_2Cl$ in LDPE that best fits the measured mass uptake is 9.8E-10 cm^2/s. The solid line in Figure 3-5 shows the predicted mass uptake using the best-fit D_{PE} in comparison to the measured values, and uncertainty in D_{PE} due to uncertainty in the measured values and sensitivity of the fitting algorithm to D_{PE}. Lohmann (2012) predicts $-\log D_{PE} = 0.0145V_m + 6.1$ which gives 4.7E-8 cm^2/s for a molar volume $V_m \approx 85$ cm^3. In addition, Lohmann (2012) discusses the difficulty in determining D_{PE} by comparing two techniques: a film stacking approach and a spinning approach. The film stacking approach involves pressing layers of LDPE against an inner layer loaded with a known amount of analyte. The layers are then taken apart and analyzed to track the movement of the diffusion front. In the spinning approach, a well-stirred aqueous solution is used to measure the absorption/desorption of a chosen chemical species in time. Estimated diffusion coefficients measured this way are based on the assumption that the mass transfer is LDPE-side controlled. This approach generally results in lower values for the diffusion coefficient than the film stacking approach. Lohmann (2012) suspects an issue with the assumptions of the spinning approach and suggests its lower diffusivities are caused by boundary layer control limiting the diffusion. The experiment shown here is most similar to the spinning technique and, consistent with this comparison, results in a much lower D_{PE} than predicted by the film stacking method. Despite this deviation, the estimated diffusion coefficient from the flume experiments will be used in this work for two reasons. First, similar to the correlations for K_{PEw}, the correlation for D_{PE} used by Lohmann (2012) was obtained from experiments using much thinner LDPE. Second, the

diffusion in the water-side boundary layer and in the LDPE-side boundary layer were accounted for in the model used to obtain a best fit D_{PE} from the data.

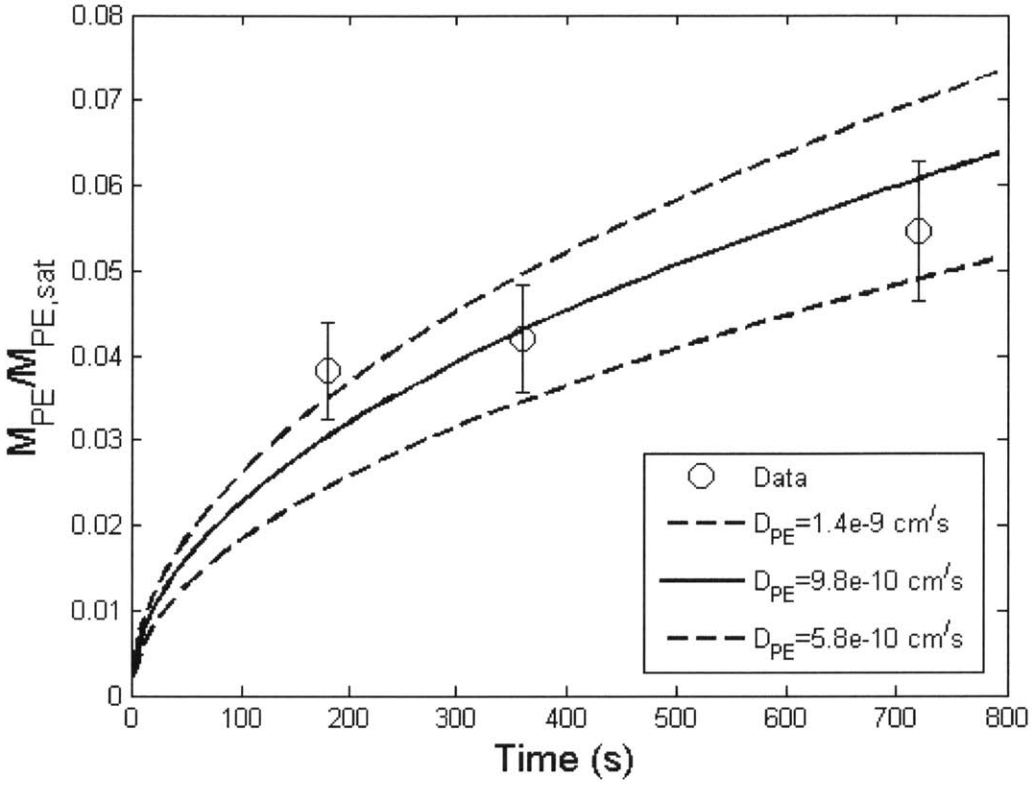

Figure 3-5. Uptake of $CHBr_2Cl$ by LDPE in the flume with U = 0 cm/s. Lines show predicted uptake in time using the best-fit diffusion coefficient, D_{PE} (solid line) and the limits of uncertainty on the fit D_{PE} (dashed lines) based on the model sensitivity to D_{PE}.

The results of the unidirectional flow experiments for U ≥ 0 cm/s are shown in Figure 3-6. The lowest fractional uptake observed was 0.029 (10.3 cm/s, 180 s) and the highest uptake was 0.14 (20.7 cm/s, 720 s). Except for 40 cm/s, mass uptake at each velocity increased with increasing exposure time in the flume, which is the physical expectation. Because this trend does not hold at 40 cm/s, the data collected at this flow rate were considered to be compromised in some way. For U > 0 cm/s, the mass uptake is constant within experimental error. However, it does appear to increase slightly with

velocity for the blades exposed for 720 s (green circles in Figure 3-6). The uptake predicted from a transfer velocity described by the flat plate model for δ_D and using K_{PEw} = 25 and either D_{PE} = 1.4E-9 cm^2/s (the value determined by best-fit of data at U = 0, dashed lines) or D_{PE} = 4.7E-8 cm^2/s (the value determined from the Lohmann correlation, solid lines) are also shown for comparison in Figure 3-6. There is generally poor agreement between the model and the experimental data regardless of the diffusion coefficient used. The model greatly under-predicts the uptake for 720 s and 360 s exposure times when D_{PE} = 1.4E-9 cm^2/s, but it over-predicts all three exposure time to an even larger degree when D_{PE} = 4.7E-8 cm^2/s. One possible explanation for this poor agreement is that the diffusion coefficient is actually in between the two values shown in Figure 3-6. Another explanation is that the diffusion coefficient is on the order of 10^{-8} cm^2/s, as suggested by the Lohmann correlation, but that significant losses occurred in processing the blades. However, the air loss experiments described in the methods section make the second explanation less likely, since we expect only 15% to be lost on average. Using the lower value for the diffusion coefficient, the model only exhibits variation in uptake with velocity for the 720 s exposure time and U < 5 cm/s. In this respect, the model (D_{PE} = 1.4E-9 cm^2/s) and the experimental data are consistent with each other. Both the model results (D_{PE} = 1.4E-9 cm^2/s) and the experimental results indicate the uptake is controlled more by diffusion within the LDPE rather than diffusion in water-side boundary layer which is expected to cause an increase in uptake with an increase in velocity.

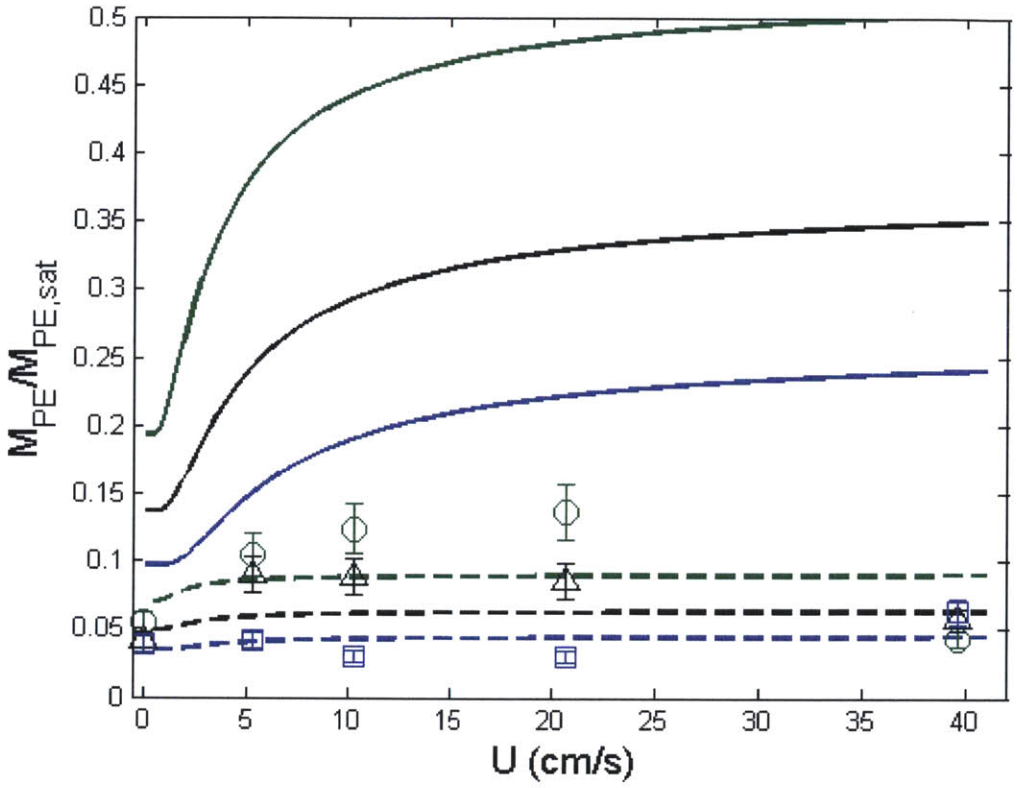

Figure 3-6. Mass uptake normalized by saturated mass as a function of velocity. Circles, triangles, and squares show data for exposure times of 720 s, 360s, and 180 s, respectively. Solid lines show model using flat-plate value of δ_D (K_{PEw} = 25 and D_{PE} = 4.7E-8 cm2/s) results for exposure times of 720 s (green), 360s (black), and 180 s (blue). Dashed lines show flat plate model (K_{PEw} = 25 and D_{PE} = 1.4E-9 cm2/s) results for exposure times of 720 s (green), 360s (black), and 180 s (blue). Table of raw measured data provided in Appendix C.

3.5.2 Wave Experiments

The measured relative mass uptake versus the wave velocity is shown in Figure 3-7 for blades exposed to $CHBr_2Cl$ for 360 s, with green and blue symbols distinguishing between 15 cm and 5 cm blades, respectively. The small amplitude wave (T_w = 2 s, a = 1 cm, U_w = 6.2 cm/s) and the large amplitude wave (T_w = 2 s, a = 4 cm, U_w 18.9 cm/s) are represented by circles and squares, respectively. The relative velocity for each blade in each wave condition was determined experimentally and presented in the results of Chapter 2 (Equation 2.3). The uptake, normalized by the saturated mass, M_{sat} =

$C_{w,\infty}K_{PEW}V_{PE}$, increased only slightly with increasing relative velocity ranging from 0.026 to 0.083. The prediction from the uptake model with K_{PEw} = 25 is also shown in Figure 3-7 using both the Ledwell model (blue lines) and the surface renewal model (dashed black lines) to define the effective diffusive sub-layer thickness ($\delta_{D,eff}$) in Equation 3.6. The solid black lines indicate the effective upper limit of the uptake, determined by running the diffusion model with $\delta_D = 10^{-15}$ cm, i.e. effectively zero. The diffusion model was run with D_{PE} = 1.4E-9 cm^2/s (lower lines) and D_{PE} = 4.7E-8 cm^2/s (higher lines). The diffusion model over-predicts the mass uptake regardless of the diffusion coefficient with the exception of D_{PE} = 1.4E-9 cm^2/s for the highest u_{rel}. Like the unidirectional case, the diffusion model predictions of mass uptake were insensitive to velocity, especially for the lower PE diffusion coefficient. This result suggests that, over the entire velocity range, the timescale for diffusion through the water-side boundary is shorter than the timescale for diffusion through the LDPE. As a result the mass transfer velocity is dominated by the diffusion through the LDPE, which is independent of the velocity. This hypothesis is explored further with consideration to the uncertainty in D_{PE} in the discussion below (sub-section 3.5.3).

The experiment was rerun with the same flow conditions and the same blade geometries. To explore a wider range of u_{rel}, an extra set of 15 cm blades were exposed in the flume and only the last 5 cm of the free end of the blade were cut and analyzed for the uptake of $CHBr_2Cl$. The relative velocity for these blade tip samples was found by taking the length-averaged relative velocity of the last 5 cm of the 15 cm long blades, as observed in Chapter 2. In this second experiment, uptake was much larger than that measured in the previous experiment (ranging from M_{PE}/M_{sat} = 0.076 to 0.22) with no consistent pattern with the relative velocity (Figure 3-8).

As in the previous experiment, the diffusion model using D_{PE} = 4.7E-8 cm^2/s over-predicts the mass accumulation, but the diffusion model using D_{PE} = 1.4E-9 cm^2/s under-predicts the mass accumulation. It is difficult to say why the two experiments shown in Figures 3-7 and 3-8 were so inconsistent, if there were losses, contamination, or some other experimental factor for which we did not account. For example, both the diffusion coefficient and partition coefficient are temperature sensitive. The large difference in the mass uptake relative to the saturated mass between the two experiments shows the importance of taking multiple exposure times for a given flow condition as a means of measurement quality control and identifying spurious data points. Because of the uncertainty associated with the diffusion coefficient in the PE and in K_{PEw}, seeing an increase in the mass uptake with exposure time is the best way to confirm the blades were not contaminated or otherwise mishandled.

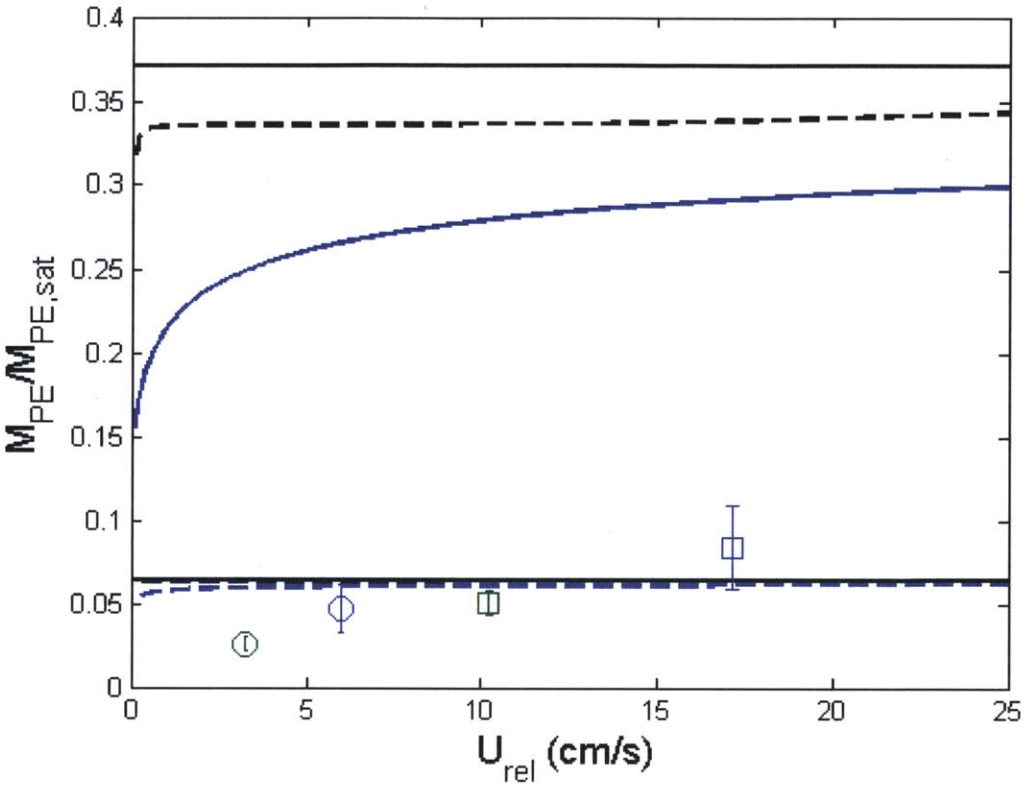

Figure 3-7. Mass uptake relative to the saturated mass versus characteristic velocity after 360 s. Data for 5 and 15 cm blades (blue and green symbols, respectively) are shown versus their relative velocity ($U=u_{rel}$) in small amplitude waves (U_w = 6.2 cm/s, circles) and large amplitude waves (U_w = 18.9 cm/s, squares). The model results are shown for the Ledwell model versus relative velocity ($U=u_{rel}$) with D_{PE} = 1.4E-9 cm²/s (dashed blue line) and D_{PE} = 4.7E-8 cm²/s (solid blue line). The surface renewal model (T_w = 2 s) for the two D_{PE} values are shown with dashed black line versus peak wave velocity ($U=U_w$). Table of raw measured data provided in Appendix C. The solid black lines indicate the diffusion model with $\delta_D=10^{-15}$ cm, i.e. effectively zero.

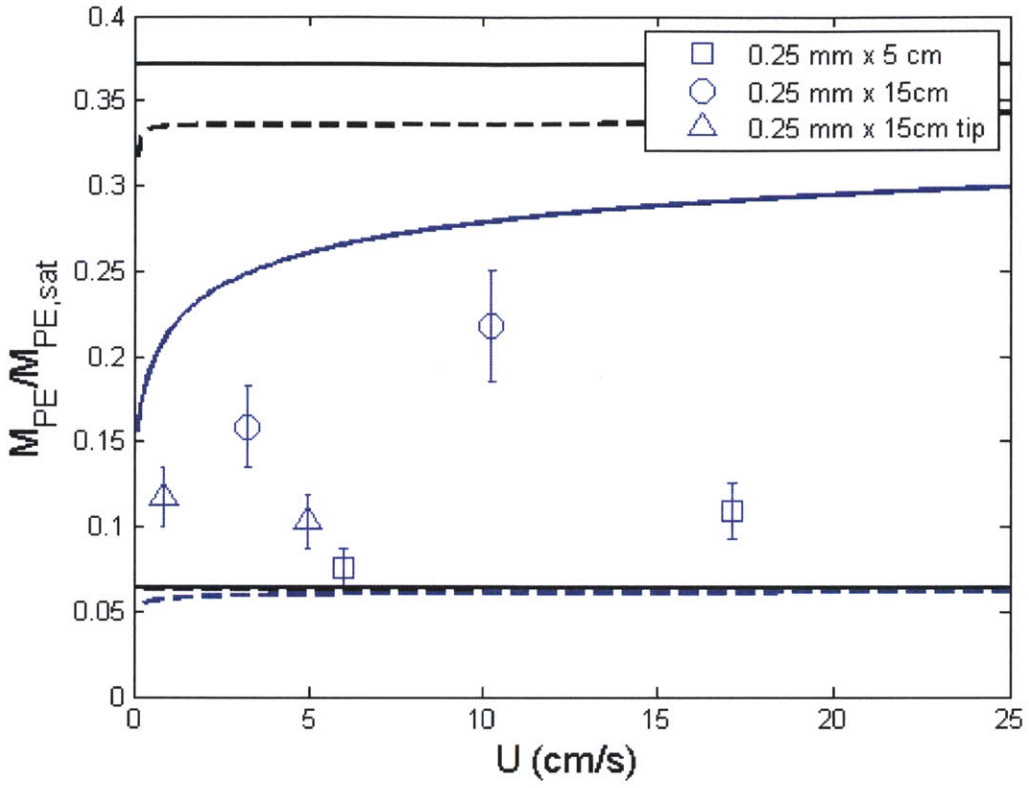

Figure 3-8. Mass uptake relative to the saturated mass versus characteristic velocity after 360 s. Data for 5 cm long blades (squares), 15 cm long whole blades (circles), and the top 5 cm of a 15 cm long blade (triangles) are shown versus their relative velocity ($U=u_{rel}$) in small amplitude waves (U_w = 6.2 cm/s) and large amplitude waves (U_w = 18.9 cm/s). The model results are shown for the Ledwell model versus relative velocity ($U=u_{rel}$) with D_{PE} = 1.4E-9 cm^2/s (dashed blue line) and D_{PE} = 4.7E-8 cm^2/s (solid blue line). The surface renewal model (T = 2 s) for the two D_{PE} values are shown with dashed and solid black lines versus peak wave velocity ($U=U_w$). Table of raw measured data provided in Appendix C. The solid black lines indicate the diffusion model with $\delta_D=10^{-15}$ cm, i.e. effectively zero.

3.5.3 K_{PE}^{crit} for Water-side Control of Flux

The uncertainty in the diffusion coefficient in PE and lack of variation in uptake with velocity makes it very difficult to compare the performance of the different models in predicting $\delta_{D,eff}$ (ie flat plate, surface renewal, and Ledwell). Only when the rate of uptake by the blade is comparable to (mixed control) or much larger than (water-side control) the rate of transport to the blade surface, can the measured uptake be used to infer changes in

the water-side control parameters, namely $\delta_{D,eff}$. For a final analysis of the experiment's ability to meet the requirement that either water-side control or mixed control is occurring, we follow the example of Schwarzenbach et al (2003) who consider a simple two film model with a phase change at the interface with an emphasis on an air-water system. Each film consists of one the phases with a characteristic transfer velocity. The overall transfer velocity (k_{PEw}) is a combination of the transfer velocity on the water-side (k_w) and the transfer velocity on the LDPE-side (k_{PE}), mediated by the partition coefficient, which sets the concentration jump (phase change) at the interface. Starting from the assumption of mass conservation at the interface (Eq. 3.4), i.e. flux from water to interface must equal the flux from interface into the LDPE, Schwarzenbach et al (2003) show the overall transfer velocity is given by the following equation.

$$\frac{1}{k_{PEw}} = \frac{1}{k_w} + \frac{1}{k_{PE}K_{PEw}} \tag{3.22}$$

In order for the overall exchange to be dominated by the water-side, the transfer velocity on the LDPE side ($k_{PE}K_{PEw}$) must be much larger than the transfer velocity on the water side (k_w) so that the second term on the right-hand side of Equation 3.22 goes to zero and the overall transfer velocity is only dependent on k_w. The water-side transfer velocity, k_w, can be reasonably approximated by the diffusion coefficient divided by a characteristic length-scale for diffusion for each phase. Then, a critical partition coefficient can be defined such that the exchange is water-side controlled when $K_{PEw} >> K_{PEw}^{crit}$ (Schwarzenbach et al., 2003). Taking the half-thickness (h/2) of the LDPE as its characteristic length (due to symmetry at z = 0) and the diffusive boundary layer thickness (δ_D) as the water-side characteristic length, the critical partition coefficient is shown as Equation 3.23.

$$K_{PEw}^{crit} = \frac{D_w}{\delta_D}\frac{h/2}{D_{PE}} \tag{3.23}$$

Values of K_{PEw}^{crit} calculated for a range of D_{PE} and δ_D, and using $D_w = 10^{-5}$ cm^2/s and h = 0.025 cm, are given in Table 3.1. In the first two rows of the table, the diffusive sub-layer thicknesses were calculated using Equation 3.8 for U = 1 cm/s and U = 1 m/s. In each case, the experimentally determined partition coefficient K_{PEw} = 25 is the same order of magnitude or less than the critical value. At best, this means that the exchange is controlled by both the water-side and the LDPE-side together, in which case the experiment should reveal physical changes in δ_D and its impact on flux. However, in some cases, $K_{PEw} << K_{PE}^{crit}$, which suggests that exchange will be LDPE-phase controlled, and the diffusion model will be insensitive to the value of δ_D. The velocities which result in $K_{PEw} = K_{PE}^{crit}$, for D_{PE}=1.4E-9 cm^2/s and D_{PE}=4.7E-8 cm^2/s are 0.14 cm/s and 4.7 cm/s, respectively (last two rows in Table 3.1). This analysis is supported by the experimental data for both unidirectional and oscillatory conditions, which show little variation with velocity. Increasing the velocity decreases the effective thickness of the water-side boundary. Therefore, the mass uptake is sensitive to hydrodynamic conditions only when the system is water-side controlled to a comparable or greater degree than it is LDPE-side controlled. The fact that the experiments (e.g. mass uptake vs velocity in Figure 3-6, 3-7, and 3-8) showed so little variation in uptake with velocity strongly supports the conclusion that the experiments were limited by LDPE-side mass transfer.

Table 3.1 Sub-layer thickness, δ_D (Eq. 3.8), and critical partition coefficient, K_{PEw}^{crit}, corresponding to the velocity in column 1. Assuming $D_w = 10^{-5}$ cm^2/s, h = 250 μm and $u_*/U = 0.05$.

U (cm/s)	δ_D (mm)	D_{PE} = 1.4E-9 cm^2/s	D_{PE} = 4.7E-8 cm^2/s
1	2.00	89	2.7
100	0.0200	890	27
0.14	0.714	25	0.745
4.7	0.0213	840	25

3.6 CONCLUSIONS

In this chapter, a method for determining the mass uptake of $CHBr_2Cl$ by LDPE in a laboratory flume was described. A preliminary experiment determined the partition coefficient, $K_{PEw} = 25$. Additionally, loss of $CHBr_2Cl$ to the air during sample processing and handling appeared to be minimal (15% loss on average). Mass uptake by blades in unidirectional flow (U = 0 - 40 cm/s) was observed for exposure times of 180 s, 360 s, and 720 s. Mass uptake was clearly seen to increase with increasing exposure time, but was constant for a given exposure time across all velocities. In wave conditions, a single exposure time was used for all blades with a range of relative velocities (u_{rel} = 0.8 - 17 cm/s). There was no clear trend in uptake with relative velocity or wave velocity. There was also poor agreement between replicate experiments, which could not be explained. Additionally, measured mass uptake deviated significantly from predicted mass uptake for both waves and currents. The model results were very sensitive to the choice of D_{PE}, which was not well constrained, such that the main uncertainty in the models was the uncertainty in D_{PE}. The goal of the experiment was to compare the effectiveness of different flux models described in the introduction. However, it is crucial that the experiment exhibit some water-phase control in order to do so. Ideally, the experiment would be completely water-phase controlled because this would also make the models less sensitive to D_{PE}. However,

the lack of dependence of measured uptake on hydrodynamic condition, as well as a comparison of the contribution of water-side and PE-side control to the overall exchange velocity (summarized in Table 3.1) suggest that the experimental uptake was controlled by the flux within the PE. Based on the analysis using Equation 3.23, future experiments need to use a chemical with a much higher K_{PEw} (>> 100), and/or thinner blades (smaller h), and/or a lower range of velocity, to achieve experimental conditions in which the flux is water-side controlled

CHAPTER 4. FLUX EXPERIMENTS USING 1,2-DICHLOROBENZENE

4.1 SELECTION OF 1,2-DICHLOROBENZENE

In Chapter 3 a method was described for measuring the uptake of dibromochloromethane ($CHBr_2Cl$) by low-density polyethylene (LDPE). The flow conditions and thickness of the LDPE were chosen in order to explore a range of dynamic behavior determined by the Cauchy number (Ca) and the buoyancy parameter (B). These parameters were defined and explored in detail in Chapter 2. Unfortunately, the conclusion arrived at in Chapter 3 was that the low partition coefficient (K_{PEw}) and diffusion coefficient (D_{PE}) for $CHBr_2Cl$ resulted in LDPE-side controlled mass uptake. Consequently, the method was ill-suited for testing different models for the transport of chemical species from the bulk fluid to the blade surface under varying flow conditions.

To resolve this issue, a different chemical species was sought for use with the same LDPE. The smaller the chemical, usually quantified by molar volume, the smaller the diffusion coefficient. However, larger hydrophobic organic molecules have larger partition coefficients (due to lower water solubility). In this experiment, a larger organic molecule was chosen for two reasons. First, the partition coefficient is more sensitive to chemical species than the diffusion coefficient, so that a chemical species larger than $CHBr_2Cl$ likely has a significantly larger partition coefficient and a relatively similar diffusion coefficient. More importantly, as long as the K_{PEw} is high enough, specifically higher that the critical value defined in Eq. 3.23, the diffusion coefficient of the chemical in the LDPE should be less important.

A final consideration in choosing the chemical species arose from the need to use the chemical at sufficiently high concentrations to exceed instrument detection limits while

not exceeding drinking water limits because the flume water drains to the city sewer. The chemical species chosen was 1,2-dichlorobenzene. The EPA drinking water standard for this species is 600 ppb. With a $\log K_{ow} = 3.43$ (EPI Suite), the species is predicted to have $\log K_{PEw} = 3.01$, using the correlation found in Lohmann and Muir (2010) for 50 to 100 μm LDPE. For the 250 μm LDPE, K_{PEw} is expected to be of the same order of magnitude, $K_{PEw} = O(1000)$, but will likely be little smaller than this, as was seen for dibromochloromethane ($CHBr_2Cl$, discussed in Chapter 3). In addition to changing the chemical species, an alternative method for analyzing the blades after exposure in the flume was developed. Specifically, the new method used partitioning to dichloromethane, rather than to water, to evaluate the mass uptake to the blades, so that after exposure in the flume the blades are placed in vials with dichloromethane. The concentration of 1,2-dichlorobenzene in the vial was analyzed using gas chromotography-mass spectrometry. In this chapter, the new method is described and the results of blades exposed to flume water with 1,2-dichlorobenzene are presented. Finally, the new method is compared to the old method, and suggestions are made for making further improvements to the experimental technique.

4.2 METHODS

4.2.1 Flux experiment

As described in Chapter 3, flux experiments took place in a 24 m long, 38 cm wide flume filled to 38 cm depth and operated with a recirculating pump. The length of the flume was covered with aluminum foil to reduce volatilization of the target chemical. Clean blades were attached to wooden dowels using rubber bands and mounted on an acrylic ramp where the depth was reduced to 25 cm. The water temperature was recorded (24.0°C) and

three blades, used to estimate the background concentration, were placed towards the back of the ramp. Before any blades were added to the flume, 800 mg 1,2-dichlorobenzene (TCI America) was injected into the flume, and the pumps were run at full speed for 40 min to ensure the concentration in the flume was uniform at approximately 200 ppb. Once the concentration was uniform in the flume, the flow rate was adjusted to one of the target flow rates and new blades were inserted after waiting 8-10 min. Three blades were inserted at a time in a row so that they were as close as possible to the position on the ramp where corresponding force and velocity measurements were taken (Chapter 2). The blades were spaced 10.4 cm from both walls and 9 diameters (8.4 cm) apart so that they would not be impacted by wall effects or each other (Figure 4-1). The velocity conditions are shown as "Experiment 2" in Table 2.2 and the Acoustic Doppler Velocimetry (3D Nortek Vectrino) measurements shown in Figure 2-5.

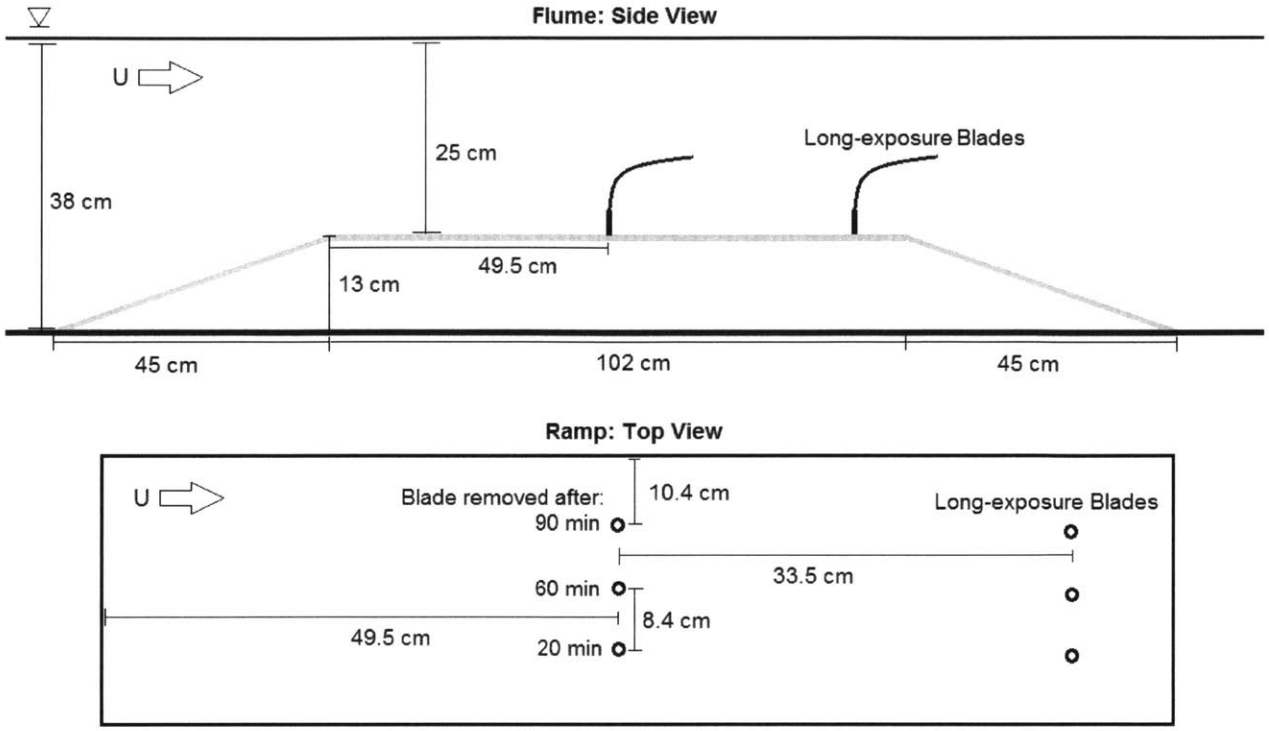

Figure 4-1. Schematic of blade positions while mounted in the flume. Not to scale.

Blades were then removed one at a time after 20 min, 60 min and 90 min using metal tongs. Excess water and potential contamination was removed from the blade surface using a kimwipe (Kimtech) before the blade was place in a clean 40 mL glass amber vial with 40 mL of dichloromethane (JT Baker). Approximately 15 min before the blade was added, the vials were also spiked with 100 µg 4-bromofluorobenzne (2000 µg/mL analytical standard solution in methanol, NSI Environmental Solution). Because all vials were spiked with the same amount of 4-bromofluorobenze, its measured mass was used to correct both for potential losses during the processing of samples and for fluctuations in the GC-MS response. After blades had been collected for each flow condition and exposure duration (7.25 hours from the time of injection), the pumps were run at full speed for an additional 4 hours while the long-exposure blades remained in the flume. The long-

exposure blades were collected in the same manner. It was noted that the process of removing a blade from the flume and inserting it into a solvent-filled vial took about 45 s. All samples were left in solvent for two days and analyzed on the same day. It was determined experimentally (see subsection 4.2.4) that a single extraction after two days was sufficient to extract all of the 1,2-dichlorobenzene from the blade. With the exception of vials with long-exposure blades, the concentration of all other vials was measured after concentrating them to ~4 mL as described below.

4.2.2 LDPE Preparation

All LDPE used in experiments described in this chapter were first cut into 15 cm long and 5 cm wide blades from the same roll of 250 μm film (McMaster) stored at room temperature. The strips were then cleaned by twice soaking for at least 24 hours in dichloromethane, twice in methanol and twice in clean milliQ water (18 MΩ) where it was stored until use in experiments.

4.2.3 Concentration measurements

Chemical concentrations in dichloromethane were measured using gas chromatography-mass spectrometry (GC-MS, Perkin Elmer Clarus 600/c) with a flame ionization detector (FID). An autosampler made splitless 3 μL injections onto a 30 m Agilent J&W DB–XLB capillary column (0.250 mm internal diameter with a 1.00 μm film). The carrier gas flow rate through the column was maintained at 2 mL/min while the GC temperature was initially held at 80°C for 1 min, then ramped at 15°C/min to 220°C and held for 6.67 min for a total run time of 17 min. The MS was operated in selected ion monitoring (SIM) and EI+ modes after a solvent hold of 4 min. Peak areas were obtained using the most abundant ions (m/z 95 for 4-bromofluorobenzene and m/z 146 for 1,2-

dichlorobenzene). Calibrations with standard concentrations of 1,2-dichlorobenze and 4-bromofluorobenze are shown in Figure 4-2 and Table 4.1. The lower limit of detection for 1,2-dichlorobenzene was found to be 0.1 µg/mL.

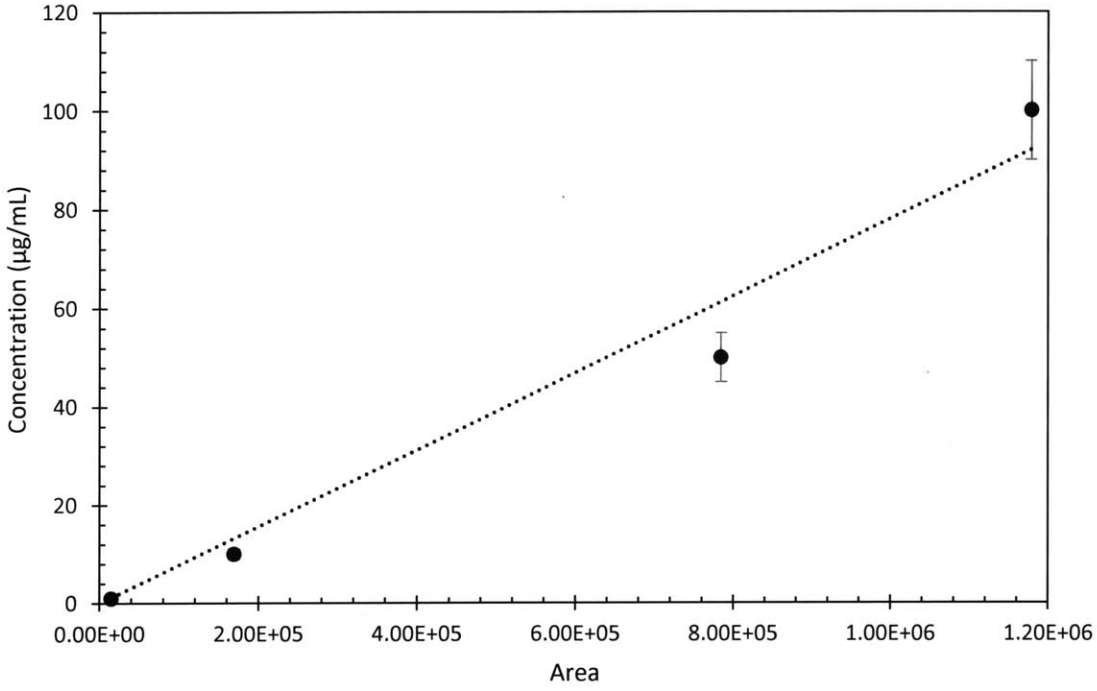

Figure 4-2. Calibration of GC/MS response for 1,2-Dichlorobenzene

Table 4.1 GC/MS peak areas for known concentrations of 1,2-Dichlorobenzene and 4-Bromofluorobenzene.

	1,2-Dichlorobenzene	4-Bromofluorobenzene
Retention Time (min):	5.74	4.44
Concentration (µg/mL)	m/z 146 Area	m/z 95 Area
1	15000	5000
10	169000	37000
50	784000	
100	1178000	
Overall response factor Area/(µg/mL)	7.8E-5	2.7E-4

4.2.4 Determining K_{PEw}

Pure 1,2-dichlorobenzene was diluted to a stock solution of 1000 μg/mL in dichloromethane. This solution was further diluted to 2 ppm in clean milliQ water (18 MΩ) and shaken vigorously so no beads of 1,2-dichlorobenzene were visible and the solution was well mixed. Three separate 40 mL glass amber vials (Qorpak) with individual clean blades were filled to over flowing with this solution so that no air was present in the vials. In order to get as accurate a measure of the initial concentration of the water before equilibrium ($C_{w,o}$) as possible, the same 1000 μg/mL 1,2-dichlorobenzene stock solution used to bring water to 2 ppm was used to make a solution of 2 ppm 1,2-dichlorobenzene in dichloromethane and measured on the same day that the solution was made with milliQ and placed in vials with blades.

After three days, the blades were removed from the water, patted dry, and placed in clean 40 mL amber vials with 40 mL dichloromethane. Three days equilibration time was estimated to be sufficient based the numerical model for uptake in a finite bath assuming a range of K_{PEw} between 25 and 1000 and D_{PE} = 5E-9 cm^2/s (Tcaciuc et al, 2014). At this time, the vials were spiked with 100 μg 4-bromofluorobenzene as an internal standard. After soaking overnight in dichloromethane, the blades were removed and the concentration was measured. A second extraction was done to confirm that a complete transfer of 1,2-dichlorobenzene occurred in the first extraction. The blade removed from the first vial was placed in a clean vial with 40 mL dichloromethane. After the extraction, the concentration was well below detection limits so that it was subsequently assumed that a complete transfer of all 1,2-dichlorobenzene initially present in the LDPE to dichloromethane is achieved using a single extraction. In addition, the concentrations of all three samples were

measured three times to assess measurement uncertainty. The mass of 1,2-dichlorobenzene in the LDPE at saturation, is calculated as the total mass in the extract by multiplying the vial concentration by the volume of solvent ($M_{PE,sat}=C_{vial}V_{solvent}$). Assuming the blades were in equilibrium with the water at the time they were removed, conservation of mass leads to the following equation.

$$C_{w,o}V_w = M_{PE,sat} + \frac{M_{PE,sat}}{K_{PEW}V_{PE}}V_w \tag{4.1}$$

In this equation, V_w is the volume of water (~41 mL) brought to equilibrium with the volume of LDPE (V_{PE}~0.38 mL), and $C_{w,o}$ is the initial concentration of 1,2-dichlorobenzene in the water before equilibrium. Rearranging Equation 4.1 results in the equation for the partition coefficient as a function of measured experimental values shown below.

$$K_{PEW} = \frac{M_{PE,sat}V_w/V_{PE}}{(C_{w,o}V_w - M_{PE,sat})} \tag{4.2}$$

4.2.5 Blow-down Process to Concentrate Vial Fluid Samples

The mass of 1,2-dichlorobenzene in a blade (M_{PE}) at the time is placed in solvent for extraction is related to the concentration measured in the final volume of solvent ($V_{solvent}$)through Equation 4.3. Assuming conservation of mass, the total mass originally in the blade (left-hand side) is equal to the sum of the mass in the blade and the mass in the solvent after equilibrium is reached (right-hand side).

$$M_{PE} = K_{PES}C_{vial}V_{PE} + C_{vial}V_{solvent} \tag{4.3}$$

K_{PES} is the partition coefficient between the blade and the solvent. Because experiments in subsection 4.2.4 showed that a second extraction into solvent resulted in C_{vial} less than detection limits, K_{PES} cannot be determined from that experiment. However, it does show

that K_{PEs} is significantly close to zero (<<1), so Equation 4.3 can be simplified to Equation 4.4 below.

$$M_{PE} \approx C_{vial}V_{solvent} \tag{4.4}$$

Extracting blades from flume (flux) experiments into 40 mL dichloromethane resulted in concentrations below detection limits. To bring them within detection limits, the extracts were concentrated to approximately 4 mL. The concentration process involved gently heating the sample on the lowest setting of a hot plate while streaming ultra-pure grade nitrogen across the surface for approximately 2 hours. The final volume of the extract was determined by weight. To determine potential losses due to this process, four 40 mL samples with a known concentration of 1,2-dichlorobenzene in dichloromethane were brought down to approximately 4 mL as described and re-measured. On average, 90% of the mass of 1,2-dichlorobenze was recovered. The mass of 1,2-dichlorobenzene measured in blades from the flume experiments (Eq. 4.4) was corrected for mass loss using the measured concentration of 4-bromofluorobenzene (C_{BFB}) and the following equation.

$$M_{PE} = \left(m_{spike}/C_{BFB}V_{solvent}\right)C_{vial}V_{solvent} \tag{4.5}$$

The mass of 4-bromofluorobenzene spiked into each sample was 100 µg, i.e. m_{spike} =100 µg.

4.3 RESULTS AND DISCUSSION

4.3.1 K_{PEw} and D_{PE}

The results of the batch experiment to find K_{PEw} are summarized in Table 4.2. The average relative standard error from the concentration measurements was 2.5%. Because this uncertainty is less than the estimated loss due to the blow-down process (10%), the concentration of 4-bromofluorobenzene is used mainly to estimate and correct for the losses due to the process of concentrating the samples. The average K_{PEw} of the three

replicate blades was 200 ∓ 70. This value is much lower than expected based on the correlation with K_{ow} resulting in K_{PEw} = 1020. Similarly, a large over-estimation of K_{PEw} was observed in Chapter 3 for $CHBr_2Cl$ (K_{PEw} = 25 observed versus K_{PEw} = 48 predicted). The previous chapter also showed that the correlation for D_{PE} likely over-predicted its value. Although the diffusion coefficient for $CHBr_2Cl$ in LDPE is not equivalent to the diffusion coefficient for 1,2-dichlorobenzene in LDPE, their molecular weights are similar enough that we expect their respective diffusion coefficients to be of the same order of magnitude. Therefore, we assume that the prediction for dichlorobenzene (D_{PE} = 1.8E-8 cm^2/s) by the same correlation is also an over-estimation, and also use an approximate value (D_{PE} = 5E-9 cm^2/s) based on the best-fit results for $CHBr_2Cl$ (see Chapter 3) in subsequent model predictions for comparison.

Table 4.2 K_{PEw} estimated from experiment with known initial concentration ($C_{w,o}$=2.41∓0.02 µg/mL) using Equation 4.2.

Sample	V_w (mL)	V_{PE} (mL)	$V_{solvent}$ (mL)	Concentration of 1,2-Dichlorobenzene in solvent (µg/mL)	Relative Standard Error (%) amongst three replicates	K_{PEw}
1	42.27	0.36	38.77	1.77	2.6	250
2	41.71	0.37	38.62	1.62	1.6	190
3	41.64	0.38	38.74	1.52	3.3	160
Average				1.63	2.5 ∓ 1.2	200 ∓ 70

4.3.2 Mass Uptake by individual blades

The mass uptake by the three long-exposure blades is given in Table 4.3 and averaged 11.6 µg. Assuming K_{PEw} = 200, D_{PE} = 5E-9 cm^2/s, the blades are estimated to be 70-90% saturated at the time of their removal from the flume. This estimate was obtained by running the numerical model described in Eqs. 3.1 to 3.7 with the boundary layer

thickness set by the flat plate model prediction given by Equation 3.8 ($\delta_{D,eff} = 5\upsilon/u_* Sc^{-1/3}$ with $u_*/U = 0.05$). The lower and upper limits are based on model results for 4 hours at 25 cm/s and 10 hours at 9 cm/s, respectively. However, it is difficult to provide an exact estimate because of the constantly changing velocity conditions, which would have changed the diffusive sub-layer thickness. Using the intended background concentration (C_W = 0.200 µg/mL) and K_{PEw}, the saturated mass uptake in the blade is predicted to be $M_{sat} = V_{PE} K_{PEw} C_W$ = 16 µg. The measured mass uptake (11.6 µg) is only 72.5% of this. If we assume the blades were at 90% saturation, the background concentration would have needed to be 0.160 µg/mL. The inability to accurately and independently determine the background water concentration using the long-exposure blades as described is a major shortcoming in the experimental set-up. Future experiments would greatly benefit from addressing this issue, and suggestions for doing so are presented in the next chapter.

Table 4.3 Mass uptake (µg) by LDPE blades in flume (Eq. 4.5) including long-exposure blades with an average uptake of 11.6 µg.

Long-exposure blades (11.25 hrs)	**Blades exposed for specific durations and flow rates**				
	Time (min)	**U = 2.0 cm/s**	**4.5**	**9.4**	**19.2**
10.8	20	4.62	1.38	1.98	2.46
12.7	60	2.59	4.20	4.30	4.88
11.3	90	3.08	4.93	5.45	6.82

4.3.3 Relative Mass Uptake versus Velocity

The measured mass uptake normalized by the mass uptake at saturation is shown in Figure 4-3 with the corresponding results of the numerical model described in Eqs. 3.1 to 3.7 and run with the boundary layer thickness set by the flat plate model prediction given by Equation 3.8 ($\delta_{D,eff} = 5\upsilon/u_* Sc^{-1/3}$ with $u_*/U = 0.05$). The experimental observations

are normalized by the saturated mass accumulation, M_{sat}, which is estimated from the average mass accumulated by the three long-exposure blades (11.6 μg, Table 4.3), adjusted to account for only 72.5% saturation (see section 4.3.2). The resulting value is M_{sat} = 16.1 μg. With the exception of the sample collected for 20 min at U = 2.0 cm/s, normalized uptake increased with time at each velocity. Additionally, for each collection time, the uptake increased with increasing velocity. However, for U ≥ 4.5 cm/s, the increase was very slight and did not exceed experimental uncertainty. Figure 4-3 also shows that the flat plate model (K_{PEw} = 200 and D_{PE} = 5E-9 cm^2/s) agrees with observations, within experimental uncertainty, for all samples collected. The flat plate model with a higher diffusion coefficient (K_{PEw} = 200 and D_{PE} = 1.8E-8 cm^2/s) shown in Figure 4-3 (dashed blue lines) exhibits a higher dependence on velocity than the other model runs (with D_{PE} = 5E-9 cm^2/s) as well as the experimental observations. The model is sensitivity to the diffusion coefficient D_{PE}, which is not well defined and thus remains a large source of uncertainty in the model, indicating significant LDPE-side control over mass uptake. At low velocity (U ≤ 4.5 cm/s) and shorter exposure time (20 min), there is less sensitivity of the model to the diffusion coefficient.

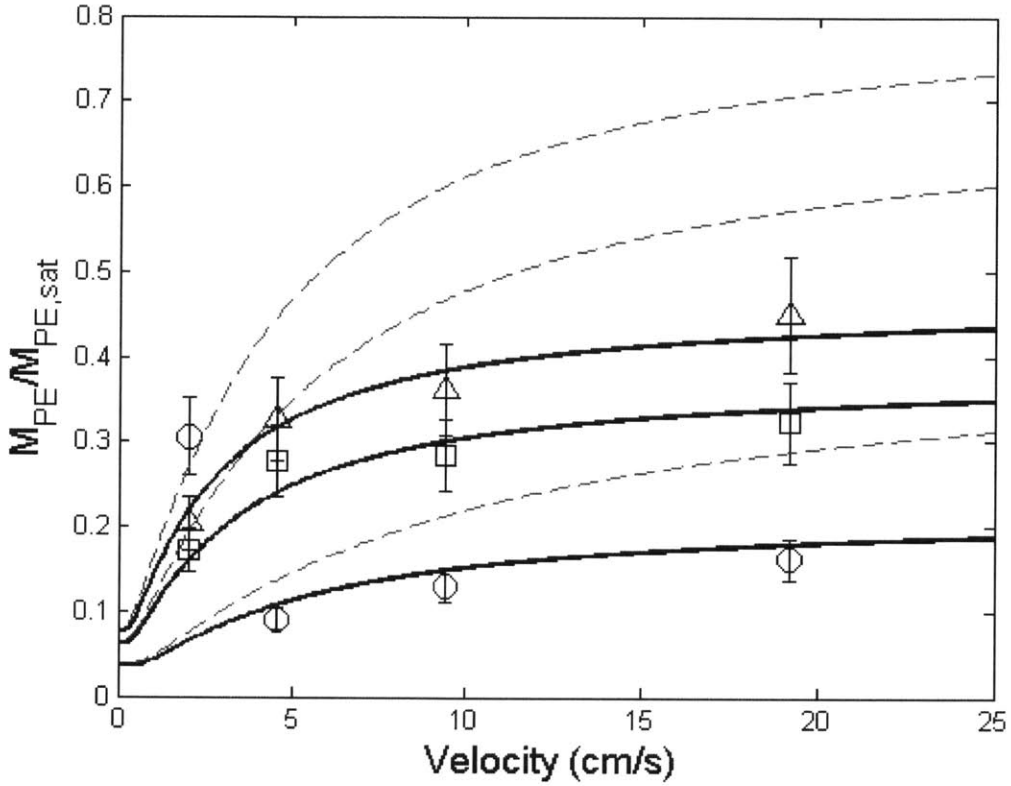

Figure 4-3. Mass uptake normalized by saturated mass. Circles, squares, and triangles, show measured values for samples removed after 20 min, 60 min, and 90 min, respectively. The thick black lines show model results for K_{PEw} = 200 and D_{PE} = 5E-9 cm^2/s and the blue dashed lines show model results for K_{PEw} = 200 and D_{PE} = 1.8E-8 cm^2/s. The model predictions assume the sub-layer thickness is set by the flat-plate model with $\delta_{D,eff} = 5\upsilon/u_* Sc^{-1/3}$.

To further evaluate the applicability of flat plate model sub-layer thickness, the effective thickness of the diffusive boundary layer, $\delta_{D,eff}$, was extracted from the fitting the accumulation model (Equations 3.1 to 3.7) to the data. At each velocity, the effective diffusive sub-layer thickness was determined by finding the least sum-squared difference between the observed relative mass uptake and the modeled mass uptake at each of the three time points (Table 4.4). The effective boundary layer thickness, assuming K_{PEw} = 200 and D_{PE} = 5E-9 cm^2/s, was most similar to the flat plate boundary layer prediction (Equation 3.8) agreeing within uncertainty and with a mean percent difference of 36%. The effective boundary layer thickness, assuming K_{PEw} = 200 and D_{PE} = 1.8E-8 cm^2/s, agreed

with the flat plate model within uncertainty for $U \leq 4.5$ cm/s, but not for $U > 4.5$ cm/s. Overall, the fit sub-layer thickness, assuming D_{PE} = 1.8E-8 cm^2/s, had a percent difference of 180% with the sub-layer thickness predicted by the flat plate model.

Table 4.4 Effective boundary layer thickness (cm) implied by observed mass uptake and assuming K_{PEw} = 200. Flat plate model boundary layer thickness was calculated using Eq. 3.8 and u_*/U = 0.05. The ranges of possible values due to uncertainty in Eq. 3.8, where u_*/U can vary between 0.05 and 0.1 and the prefactor 10 is sometimes used instead of 5, are shown in parentheses.

U (cm/s)	D_{PE} = 5E-9 cm^2/s	D_{PE} = 1.8E-8 cm^2/s	Flat Plate Model
2.0	0.050	0.073	0.049 (0.024-0.098)
4.5	0.028	0.042	0.022 (0.011-0.043)
9.4	0.016	0.033	0.010 (0.0052-0.021)
19.2	0.0081	0.023	0.0051 (0.0025-0.010)

The fit sub-layer thicknesses are also represented graphically versus velocity in Figure 4-4 (a). The blue and black symbols show the results assuming D_{PE} = 1.8E-8 cm^2/s and D_{PE} = 5E-9 cm^2/s, respectively. For comparison, the flat plate model sub-layer thickness calculated from Equation 3.8 (u_*/U = 0.05) is shown in red. Assuming the flat plate model, we expect the sub-layer thickness to vary with velocity as $\delta_{D,eff} \sim U^{-a}$ with a = 1. However, the experimental data shows a different dependence of $\delta_{D,eff}$ on U with a = 0.799 and a = 0.494 for D_{PE} = 1.8E-8 cm^2/s and D_{PE} = 5E-9 cm^2/s, respectively. Because sufficient time ($t > T_D = \delta_{D,eff}^2/D_w$) has passed even for the shortest exposure time (20 min), we can also infer from the effective sub-layer thickness a constant water-side transfer velocity, $k_w = D_w/\delta_{D,eff}$ (Eq. 3.9). The transfer velocities calculated from the fit sub-layer thicknesses shown in Table 4.4 and Figure 4-4 (a) are shown as a function of velocity in comparison to the flat plate model (red line) in Figure 4-4 (b). Because $\delta_{D,eff}$ is inversely proportional to U in Equation 3.9, the flat plate model predicts k to increase linearly with

velocity whereas Figure 4-4 (b) shows k calculated from fit $\delta_{D,eff}$ increasing with velocity in a non-linear way. Also shown in Figure 4-4 (b) is the empirical relation between the blade tip height and the velocity derived in Chapter 2 (see Figure 2-8). The changing posture of the blade is also illustrated qualitatively in Figure 4-5 which shows a trace of the entire blade for different values of z_{tip}/l from images obtained using a Sony digital camera. Blades with $U > 4.5$ cm/s ($Ca > 16$) bend to a height below half the blade length ($ztip/l < 0.50$) whereas blades below this velocity remain mostly upright ($ztip/l \geq 0.85$).

The significant change in posture is a possible explanation for the non-linear scaling of the transfer velocity. Sparrow et al (1979) found that the heat (measured via mass) transfer velocity varies with U as $k \sim U^{1/2}$ for plates inclined from 90°-25° with 90° being normal to the flow. For a narrow plate ($b<l$), there was some variation (20%) in the dependence of k on U with angle of incidence. With $0.5 < a < 1$, the data shown in Figure 4-4 imply that the rate at which k increases with U decreases with greater pronation. A similar trend was observed in the force measurements reported in Chapter 2 for the same blade geometry and over the same velocity range (see Figure 2-9). Specifically, blade streamlining in the flow diminished the dependence between F_x and U, relative to the quadratic dependence expected for a non-pronated blade. The diminished dependence of transfer velocity on U relative to the linear dependence expected for a flat plate is similar (Figure 4-4). In comparison to Sparrrow et al, it is likely due to this streamlining and the coupling of velocity with the angle of incidence.

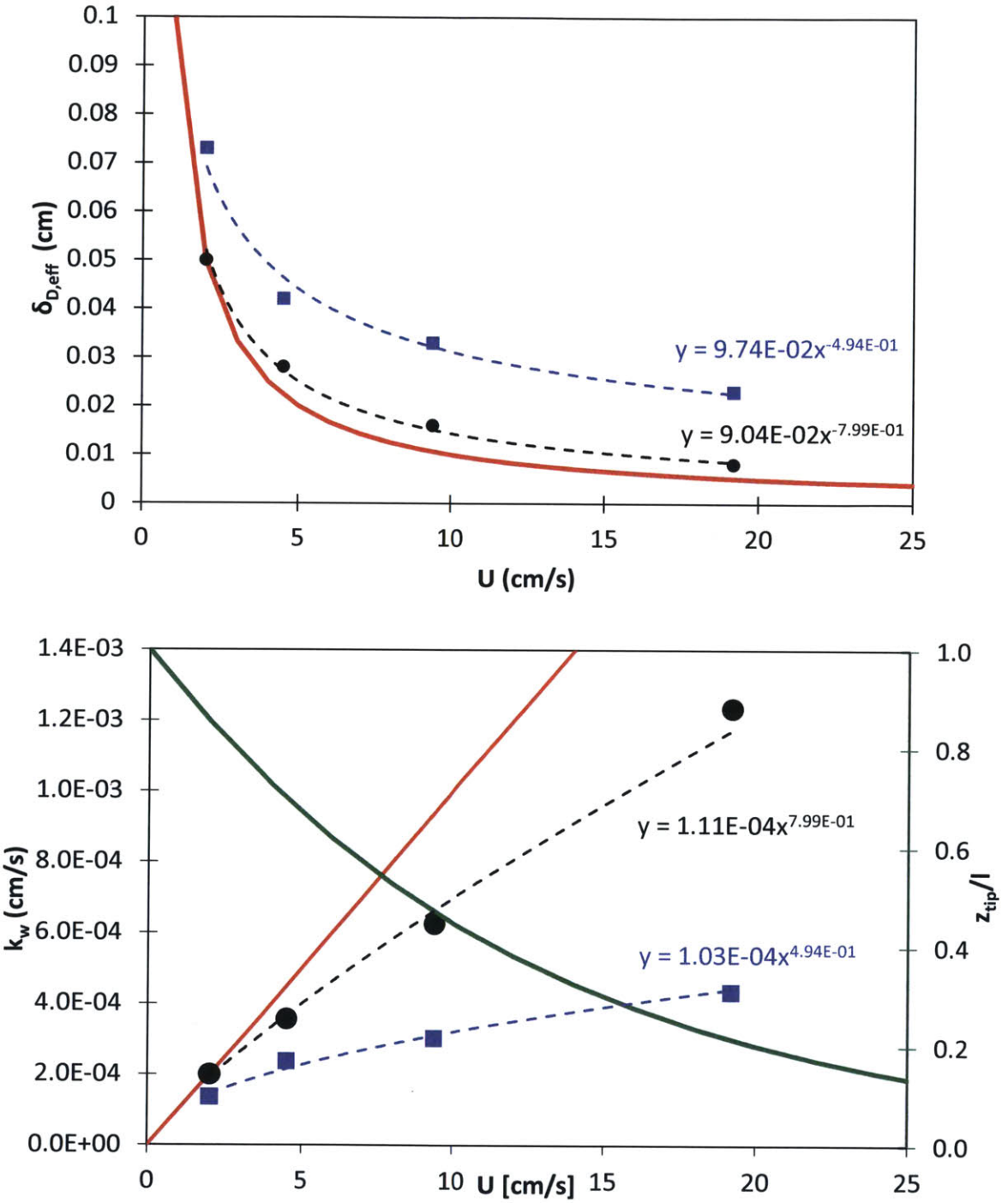

Figure 4-4. (a) Effective boundary layer thickness ($\delta_{D,eff}$) implied by observed mass uptake for D_{PE} = 1.8E-8 cm^2/s (blue squares) and D_{PE} = 5E-9 cm^2/s (black circles) and assuming K_{PEw} = 200. Red line shows the flat plate model sub-layer thickness calculated from Equation 3.8 (u_*/U = 0.05). (b) Transfer velocity calculated from boundary layer thicknesses shown in (a) using Eq. 3.9 and assuming $D_w = 10^{-5}$ cm^2/s. The red line shows the flat plate model water-side transfer velocity assuming $D_w = 10^{-5}$ cm^2/s and a sublayer thickness calculated from Equation 3.8 (u_*/U = 0.05). The green line (right axis) shows the blade tip height normalized by blade length calculated from the empirical relationship $z_{tip}/l = 1.03 * \exp[-0.08 * U]$.

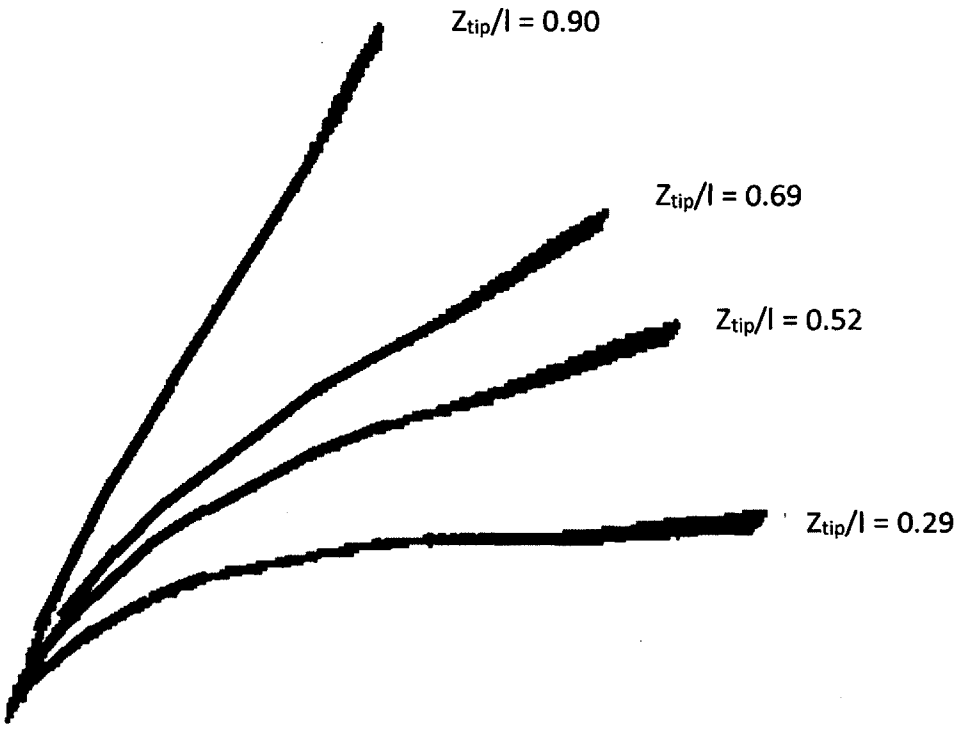

Figure 4-5. Posture of the entire blade for different normalized tip heights (z_{tip}/l).

4.3 CONCLUSIONS

In this chapter an alternative method for observing the uptake of mass by LDPE was described, and the results of a unidirectional current experiment presented. The target chemical for uptake was 1,2-dichlorobenzene, which was spiked into a large recirculating flume with an adjustable flow rate. The measured partition coefficient for 1,2-dichlorobenzene diffusing into 250 um thick LDPE was 200 ∓ 70. Mass uptake increased with increased exposure time. While some increase in mass uptake was observed for increasing velocity, the mass uptake showed much less sensitivity to velocity than expected for an entirely water-side controlled mass transfer. The weak dependence of mass uptake on velocity indicates that the blade-side diffusion exerted some control on the uptake. This is interpreted to mean that K_{PEw} and D_{PE} were too low to result in purely water boundary layer-controlled mass transfer of chemical species from the bulk fluid. This is not an optimal condition for the experiment, because the change in mass uptake between the velocity conditions are close to the uncertainty in the method. Never-the-less, the numerical prediction of mass uptake using a flat plate model for diffusive sub-layer thickness produced reasonable agreement with measured mass uptake for D_{PE}=5E-9 cm^2/s (Figure 4-3).

Despite both the water-side and LDPE-side impacting the mass uptake, we were able to extract the effective transfer velocity on the water-side using the numerical model. The fitted values for the transfer velocity had a positive correlation with velocity as would be expected for the flat plate model. However, the rate at which the transfer velocity increased with velocity decreased with increased velocity. Increased velocity also leads to

increased blade pronation (see Chapter 2), so that the change in dependence of k on U most likely results from the changes in blade posture as U is increased.

In comparison to the method described in Chapter 3, the method described here has several advantages. First, the target chemical has a higher partition coefficient (K_{PEw} = 200 for 1,2-dichlorobenze versus K_{PEw} = 25 for $CHBr_2Cl$). While K_{PEw} was not as high as anticipated (K_{PEw}=1020 according to the correlation from Lohmann and Muir, 2010), 1,2-dichlorobenze still provides a better experimental system than dibromochloromethane. Second, the method of extracting the target chemical into a solvent (as described in this chapter) is preferable to the method of extracting the target chemical into water, as described in the previous chapter. While the purge and trap method is analytically simple and reduces chemical waste (water is used instead of solvent), the technique of extracting the target chemical into solvent greatly reduces experimental uncertainty. Specifically, any uncertainty in determining K_{PEw} is compounded in the propagation of error using the method described in Chapter 3, because both the determination of M_{sat} from flume water concentration and the determination of the mass uptake to individual blades depend upon it. In contrast, in the method using solvent extraction from the blades, the partitioning coefficient used in the analysis can be assumed $<<1$, removing a source of uncertainty in determining mass uptake to individual blades. Additionally, direct extraction into solvent made the application of the internal standard straightforward, and allowed for a useful control of losses during sample processing, which was remarkably low (10%).

One disadvantage of the method described in this chapter was the difficulty in determining the background concentration in the flume. However, future experiments could account for this uncertainty by measuring the concentration directly using a purge

and trap (as described in chapter 3), leaving the background blades in the flume for longer times, or using thinner LDPE which would equilibrate more quickly. These suggestions are described in further detail in the following chapter. Both experimental techniques suffered from limitations due to the slow diffusion of the chemicals within the LDPE. In order for these experiments to be useful in understanding flux limited regimes for all flow conditions relevant to seagrass, further adjustments in experimental methods are still needed.

CHAPTER 5. CONCLUSIONS AND SUGGESTIONS FOR FUTURE WORK

The influence of the hydrodynamic environment on nutrient flux to seagrass blades remains unclear despite the many in-depth studies on the mutual influence of fluid motion and seagrass meadow characteristics. There have been several studies that show increased nutrient uptake with increased flow velocity (eg. Cornelisen and Thomas, 2006 and 2009; Nishihara and Ackerman, 2006; Morris and Peralta, 2008). However, the exact physical mechanism for flux enhancement is poorly understood, especially under oscillatory flow conditions. Since blades are flexible objects with a highly dynamic response to their environment, the physical transport of dissolved chemicals to the blade surface is an extraordinarily complex process and a predictive model for uptake has yet to be fully realized. An applicable flux model needs to account for blade dynamics as a result of the fluid environment, which influences the mass transfer velocity at the blade surface. In Chapter 1, these concepts were discussed in greater depth and three models were introduced (flat plate, surface renewal, and Ledwell) that could be used to describe the transport of dissolved chemicals to seagrass blades.

In Chapter 2, a well-established laboratory proxy for seagrass was used to determine behavior regimes under current and wave flow conditions. These regimes were related to the Cauchy number (Ca), a dimensionless parameter representing the ratio of the drag force to the restoring force due to the blade stiffness. A range of Cauchy numbers were considered by adjusting the blade length and thickness as well as the flow conditions. In currents (this study considered Ca = 3-1200), the blade height above the flume bed decreased continually and gradually with increasing velocity. The horizontal drag force had a reduction in velocity dependence ($F \sim U^{3/4}$) relative to that expected for an upright, rigid

blade ($F \sim U^2$). This indicates that streamlining of blade posture in flow (also called reconfiguration) significantly reduced the drag, relative to an erect blade of the same length. In oscillatory flow conditions (this study considered Ca = 0.25-380), the blade behavior was characterized by three regimes depending on the Cauchy number and blade length. For Ca <15, the blades remained vertical (or nearly so) with little movement in response to the waves, so that the blade-normal relative motion $u_{rel} \rightarrow U_w$. For Ca > 15 and blade length comparable to wave excursion, the blades moved with the wave throughout the wave cycle, which reduced the relative velocity, $u_{rel} < U_w$. For Ca > 15 and blade length much less than wave excursion, the blades moved with the wave for only a fraction of the wave cycle, so that over most of the wave cycle $u_{rel} = U_w$..

In Chapter 3, a method for measuring flux to the model blades was described using $CHBr_2Cl$ as the tracer chemical in the flume and a purge and trap with gas chromatography as a technique for measuring chemical concentrations. Flume experiments with unidirectional flow showed little variation in uptake with increasing velocity. Experiments in oscillatory conditions were similarly insensitive to peak wave velocity. The insensitivity of mass uptake to velocity suggested that the flux into the blade was limited by the diffusion on the LDPE side. Additional analyses that defined a critical partition coefficient, below which LDPE-controlled flux was expected, led to the conclusion that the system was LDPE-side dominated and therefore not a proper design to study the water-side hydrodynamic controls to flux.

In Chapter 4, an alternative method was explored using the same LDPE (250 μm), but with 1,2-dichlorobenzene as the tracer compound measured using gas chromatography-mass spectrometry. This experimental method resulted in mass uptake

that exhibited a greater sensitivity to velocity and better agreement with the flat plate model. The effective thickness of the water-side diffusive sub-layer was found by fitting a numerical model for mass uptake to the data and used to estimate a water-side mass transfer velocity. Using this method, the value of the water-side mass transfer velocity (k) could be isolated from the overall mass transfer velocity, even though this method had some LDPE-side control over mass flux. The water-side mass transfer velocity (k) varied with fluid velocity as $k \sim U^a$ with $0.5 < a < 1$. The flat plate model predicts $a = 1$ whereas previous studies of rigid plates inclined to flow have found $a = 0.5$ for incline angles of 90° to 25°. The results presented in Chapter 4 indicate that increased blade pronation, as a consequence of increased velocity, reduced the dependence of k on U from the flat plate model prediction.

The chemical analysis of blade concentration was improved by extracting directly into solvent, eliminating additional propagation of uncertainty in the partition coefficient (K_{PEw}), and using an internal standard to account for losses and instrument variability. However, this method still had major shortcomings. The lower than expected partition coefficient (K_{PEw}=200 observed versus K_{PEw}=1020 expected) resulted in a weaker than anticipated increase in mass uptake with increasing velocity. Additionally, the background concentration of 1,2-dichlorobenzene was not accurately known. The experiment had effectively three fitting parameters (K_{PEw}, D_{PE}, and $C_{w,\infty}$) which made comparison to the model less robust. Therefore, the following suggestions for improvements of the method focus on better constraining these parameters as well as recommendations for further reducing uncertainty.

One major improvement of the method could be achieved by more accurately determining the background concentration in the flume. There are a number of ways to accomplish this goal. For example, the concentration of water samples taken directly from the flume at the time of experiments could be measured using the purge and trap method with GC described in Chapter 3. A disadvantage of using this method is that the blade concentrations and background concentrations would be measured using two different instruments. Therefore, it would become even more important for concentration measurement to be both precise and accurate. However, this is a straightforward and potentially very reliable method.

To avoid using two different chemical analysis techniques, another option for determining the background concentration in the flume is to leave the long-exposure blades in the flume for a greater period of time (more than 12 hours). While this strategy also seems straightforward, there may be a few disadvantages. For example, such long experimental times may lead to significant losses of the chemical from the flume. As a result, the mass uptake by the long-exposure blades would reflect a different background concentration than the other blades exposed closer to the time of chemical injection into the flume. Additionally, running the pumps for such long times could cause significant heating (of several degrees) of the flume water which would affect D_{PE} and K_{PEw} in a highly non-linear way.

To reduce the total experiment time while still avoiding the use of multiple chemical analysis techniques, a third option for determining the background concentration is to use thinner LDPE for the long-exposure blades. These blades would reach equilibrium much faster than the thicker blades, thereby avoiding concerns about volatilization of the

chemical from the flume and heating by the pumps. One disadvantage to this approach is that the saturated concentration in the thinner blades is potentially different than the 250 μm thick blades, e.g. if K_{PEw} differs for the blades of different thickness. Further, the resulting sample vial concentrations may approach the GC-MS detection limits. Also, this approach requires knowing the partition coefficient for more than one thickness of LDPE, which introduces an additional source of uncertainty. However, using this approach could be especially useful in combination with the direct measurements of the flume concentration using the purge and trap technique. Using both approaches simultaneously could provide a means for identifying and correcting for variables that impact mass uptake, such as temperature.

In order to use the approach just described, and to better understand the effect of LDPE thickness on the partition coefficient, it would be useful to measure the partition coefficient for several thicknesses of LDPE under the same laboratory conditions. The review of LDPE passive samplers by Lohmann (2012) maintains that the diffusion coefficient and partition coefficient do not depend on the thickness of LDPE used. However, the measured partition coefficients for $CHBr_2Cl$ and 1,2-dichlorobenzene were significantly lower than predicted by the correlation provided by Lohmann (2012). I hypothesize that this is due to the fact that the LDPE used in this study (250 μm) was significantly thicker than the LDPE in the studies used to create the correlation (50-100 μm). Additionally, the crystallinity of different thicknesses of LDPE could be different, and this could impact both D_{PE} and K_{PEw}. The crystallinity could be measured using x-ray diffraction. Comparing the crystallinity of the different LDPE thicknesses used as passive samplers to those used in

model seagrass studies may provide insight into the observed differences in chemical properties within the different LDPE thicknesses.

I recommend the method for measuring blade concentration using desorption into solvent and analysis on the GC-MS. However, this method can also be improved, and one potentially simple improvement is to use additional internal standards. As done in Chapter 4, one internal standard can be added at the time of placing the blade in the vial with solvent to correct for losses due to handling. An additional standard (e.g. another benzene with halogen substitutions such as 4-chlorofluorobenze) could be spiked into the sample just before injection into the GC-MS so that it can be used as a correction for instrument variation due to random variations in injection volume or detector response.

Finally, I recommend that for every flow condition tested, multiple blades be used with varying exposure times. The uptake should always increase with increasing exposure time. As a result, comparing exposure times for a particular flow condition provides a quality check to ensure that samples were not somehow compromised. With these adjustments in the method, LDPE mass uptake experiments show great potential as a powerful tool for exploring the impact of fluid flow on blade motion and nutrient flux to the seagrass, an invaluable natural resource.

APPENDIX A. FLUME MIXING TEST

I conducted a preliminary experiment to determine the amount of time needed for a chemical to be well-mixed throughout the flume after injection at the pump intake. Assuming concentrations become homogenous through turbulent mixing and dispersion, both chemicals used in experiments (dibromochloromethane and 1,2-dichlorobenzene) will behave the same as a surrogate with a concentration that can be monitored in real time. I injected the surrogate tracer, Rhodamine WT, in the same manner as the flux experiment chemicals with a depth-averaged velocity of 10 cm s^{-1}. The concentration of Rhodamine WT was measured using a fluorometer and is shown in Figure B-1 below. At first, the injected Rhodamine WT was concentrated in a slug that caused peaks in the fluorometer response each time it passed through the detection window. As the chemical mixed, the peak broadened and its magnitude decreased. A constant detector signal signified that the flume was well-mixed and the concentration was homogenous. Figure B-1 shows the concentration became homogenous at ~2300 s.

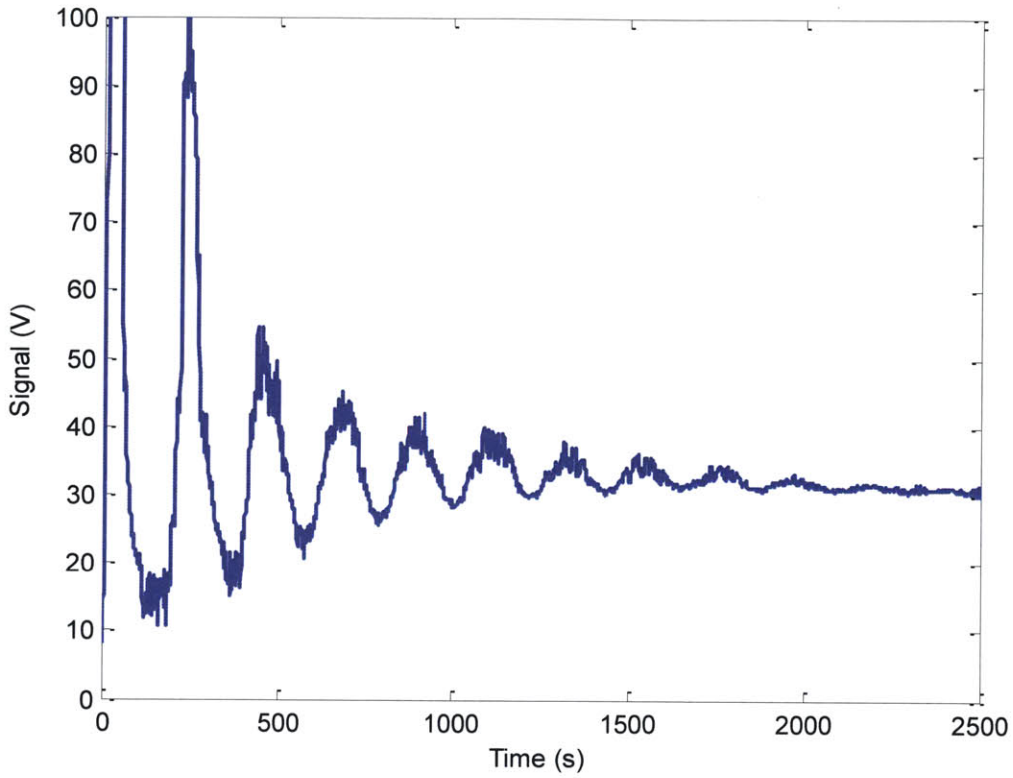

Figure B-1. Fluorometer detector response (proportional to the concentration of Rhodamine WT) as a function of time from injection of Rhodamine WT into the flume with velocity U = 10 cm/s.

APPENDIX B. MEASURED CONCENTRATIONS FROM EXPERIMENTS TO DETERMINE K_{PEw} AND THE EFFECT OF AIR EXPOSURE FOR $CHBr_2Cl$

Table B.1. Measured concentrations of $CHBr_2Cl$ from the experiment to determine K_{PEw} using different masses of LDPE with the same starting concentration of $CHBr_2Cl$ (33.5 +/- 1.32 ppb) shown in Figure 3-3.

Mass PE (g)	V_w (mL)	C_w (ppb)
0.0126	41.60	35.88 +/- 5.93
0.0573	41.97	29.04 +/- 3.67
0.332	41.28	29.18 +/- 3.76
0.46	41.56	27.85 +/- 2.26
0.95	41.97	23.66 +/- 1.27
2.07	38.84	17.11 +/- 1.28

Table B.2. Measured concentrations of $CHBr_2Cl$ from the experiment to determine the loss of $CHBr_2Cl$ from LDPE due to controlled exposure of blades to air. The mass in the PE (right-most column) is calculated using Eq. 3.16. The initial concentration of water to load the LDPE with $CHBr_2Cl$ was 64.17 +/- 0.13 ppb. The top row shows data from the control blade which was not exposed to air so that the right-most column shows $M_{PE,i} = K_{PEw}C_{w,vial}V_w$.

Exposure Time (s)	PE Mass (g)	V_w (mL)	$C_{w,vial}$ (ppb)	M_{PE} (µg)
0	2.09	40.40	41.27	$M_{PE,i}$ = 2.33 +/- 0.37
15	1.98	39.90	21.03	1.96 +/- 0.08
30	2.06	39.92	26.24	2.51 +/- 0.15
60	1.97	39.84	26.45	2.46 +/- 0.23
120	2.01	39.94	27.81	2.62 +/- 0.20
180	2.02	40.03	30.53	2.89 +/- 0.10
240	1.96	39.94	30.84	2.87 +/- 0.01

APPENDIX C. MEASURED CONCENTRATIONS FOR FLUX EXPERIMENTS WITH $CHBr_2Cl$

Table C.1. The measured concentration of $CHBr_2Cl$ in the flume water ($C_{w,\infty}$) and in the vial water ($C_{w,vial}$) for each experimental time and velocity in the current experiment. The flume water concentration and vial water concentration were used to calculate the saturated mass ($M_{PE,sat}$) and actual mass uptake (M_{PE}), respectively. The column on the far right is calculated from the vial concentration using Eq. 3.16, and the ratio of the last column to the second to last column (relative mass uptake) is also shown in Figure 3-6.

t (s)	PE Mass (g)	V_w (mL)	$C_{w,\infty}$ (ppb)	$C_{w,vial}$ (ppb)	$M_{PE,sat}$ (ng)	M_{PE} (ng)
U = 39.6 cm/s						
720	0.30	41.77	124.1	1.04	1010 +/- 25	52.0 +/- 9.1
360	0.29	41.79	136.6	1.34	1070 +/- 18	66.6 +/- 5.0
180	0.29	41.22	123.9	1.50	971 +/- 25	73.6 +/- 19
U = 20.7 cm/s						
720	0.30	40.85	144.4	3.35	1170 +/- 38	164 +/- 4.6
360	0.34	40.49	144.5	2.37	1330 +/- 16	117 +/- 17
180	0.29	41.52	154.3	0.70	1210 +/- 38	34.4 +/- 2.4
U = 10.3 cm/s						
720	0.31	41.50	145.9	3.10	1220 +/- 39	155 +/- 19
360	0.34	40.12	153.0	2.44	1410 +/- 25	120 +/- 13
180	0.34	41.40	175.8	0.79	1620 +/- 64	40.1 +/- 9.3
U = 5.3 cm/s						
720	0.37	40.33	172.2	3.09	1720 +/- 18	156 +/- 26
360	0.26	41.65	143.9	1.94	1010 +/- 46	94.2 +/- 24
180	0.31	41.20	179.6	1.04	1510 +/- 53	51.5 +/- 16
U = 0 cm/s						
720	0.30	41.46	136.2	1.33	1100 +/- 13	65.8 +/- 6.8
360	0.35	41.40	155.5	1.16	1470 +/- 18	59.0 +/- 4.0
180	0.31	41.18	141.9	0.96	1190 +/- 51	47.7 +/- 6.8

Table C.2. The measured concentration of $CHBr_2Cl$ in the flume water ($C_{w,\infty}$) and in the vial water ($C_{w,vial}$) for each blade length (l) and wave velocity (U_w) used in wave experiment 1. All blades were exposed in the flume for 360 s. The flume water concentration and vial water concentration were used to calculate the saturated mass ($M_{PE,sat}$) and actual mass uptake (M_{PE}), respectively. The column on the far right is calculated from the vial concentration using Eq. 3.16, and the ratio of the last column to the second to last column (relative mass uptake) is also shown in Figure 3-7.

l (cm)	U_w (cm/s)	U_{rel} (cm/s)	PE Mass (g)	V_w (mL)	$C_{w,\infty}$ (ppb)	$C_{w,vial}$ (ppb)	$M_{PE,sat}$ (ng)	M_{PE} (ng)
5	6.2	5.95	0.14	41.96	24.82	0.107	104 +/- 15	4.92 +/- 0.86
5	18.9	17.1	0.13	39.31	25.14	0.173	88.3 +/- 15	7.41 +/- 2.4
15	6.2	3.21	0.33	39.39	28.66	0.133	245 +/- 110	6.41 +/- 0.10
15	18.9	10.2	0.38	40.67	31.42	0.322	323 +/- 22	16.4 +/- 2.5

Table C.3. The measured concentration of $CHBr_2Cl$ in the flume water ($C_{w,\infty}$) and in the vial water ($C_{w,vial}$) for each blade length (l) and wave velocity (U_w) used in wave experiment 2. All blades were exposed in the flume for 360 s. The flume water concentration and vial water concentration were used to calculate the saturated mass ($M_{PE,sat}$) and actual mass uptake (M_{PE}), respectively. The column on the far right is calculated from the vial concentration using Eq. 3.16, and the ratio of the last column to the second to last column (relative mass uptake) is also shown in Figure 3-8.

l (cm)	U_w (cm/s)	U_{rel} (cm/s)	PE Mass (g)	V_w (mL)	$C_{w,\infty}$ (ppb)	$C_{w,vial}$ (ppb)	$M_{PE,sat}$ (ng)	M_{PE} (ng)
Whole blades								
15	18.9	10.2	0.34	41.7	102.3	3.14	951 +/-210	160 +/- 11
5	18.9	17.1	0.11	42.4	115.9	0.59	359+/-20	26.8 +/- 1.1
15	6.2	3.21	0.38	41.6	75.1	2.48	770+/-25	129 +/- 11
5	6.2	5.95	0.14	41.6	75.5	0.51	293+/-62	23.3 +/- 8.9
Top 5 cm of 15 cm long blades placed in the flume								
5	18.9	4.93	0.14	41.9	80.4	0.68	306+/-36	31.0 +/- 3.5
5	6.2	0.822	0.13	41.3	72.7	0.71	248 +/-19	31.6 +/- 2.3

APPENDIX D. MEASURED CONCENTRATIONS FOR FLUX EXPERIMENTS WITH 1,2-DICHLOROBENZE

Table D.1. Measured concentrations of 4-bromofluorobenzene (C_{BFB}) and 1,2-dichlorobenzene (C_{vial}) used to calculate relative mass uptake (Eq. 4.6) due to different exposure times and flume conditions.

t (min)	Mass PE (g)	$V_{solvent}$ (mL)	C_{BFB} (ppm)	C_{vial} (ppm)
U = 19.2 cm/s				
20	0.38	3.70	13.6 +/- 0.54	0.343 +/- 0.014
60	0.38	4.65	21.7 +/- 0.87	1.09 +/- 0.044
90	0.38	3.41	33.1 +/- 1.3	2.32 +/- 0.093
U = 9.4 cm/s				
20	0.38	2.14	20.9 +/- 0.84	0.426 +/- 0.017
60	0.37	3.44	30.1 +/-1.2	1.33 +/- 0.053
90	0.37	1.54	79.3 +/- 3.2	4.46 +/- 0.18
U = 4.5 cm/s				
20	0.35	3.25	14.0 +/- 0.56	0.199 +/- 0.0079
60	0.37	3.63	28.4 +/- 1.1	1.23 +/- 0.049
90	0.35	2.69	45.0 +/- 1.8	2.29 +/- 0.091
U = 2.0 cm/s				
20	0.35	3.08	25.8 +/- 1.0	1.23 +/- 0.049
60	0.36	3.62	35.0 +/- 1.4	0.934 +/-0.037
90	0.38	2.59	19.8 +/- 0.79	0.629 +/- 0.025
Long-exposure Blades				
	0.37	39.31	2.75 +/- 0.11	0.304 +/- 0.012
	0.37	39.17	2.54 +/- 0.10	0.297 +/- 0.012
	0.37	39.08	3.57 +/- 0.14	0.47 +/- 0.019

WORKS CITED

Abdelrhman, Mohamed A. (2007). Modeling coupling between eelgrass *Zostera marina* and water flow. Mar. Ecol. Prog. Ser., 338: 81-96.

Adams, Rachel G., Rainer Lohmann, Loretta A. Fernandez, John K. MacFarlane and Philip M. Gschwend (2007). Polyethylene devices: passive samplers for measuring dissolved hydrophobic organic compounds in aquatic environments. Environ. Sci. Technol. 41: 1317-1323.

Bal, Kris D., Natacha Brion, Veronique Woulé-Ebongué, Jonas Schoelynck, Antoinette Jooste, Cristina Barrón, Frank Dehairs, Patrick Meire, and Tjeerd J. Bouma (2013). Influence of hydraulics on the uptake of ammonium by two freshwater plants. Freshwater Biology, 58, 2452-2463.

Barko, J.W., and W. F. James (1998) Effects of submerged aquatic macrophytes on nutrient dynamics, sedimentation and resuspension. In Erik Jeppesen, Martin Søndergaard, Morten Søndergaard and Kristen Christoffersen (Eds.), *The Structuring Role of Submerged Macrophytes in Lakes* (197-214). New York: Springer-Verlag.

Bradley, K. and C. Houser (2009). Relative velocity of seagrass blades: Implications for wave attenuation in low-energy environments. J. Geophys. Res. Earth Surf. 114: F01004.

Cornelisen, Christopher D. and Florence I. M. Thomas (2006). Water flow enhances ammonium and nitrate uptake in a seagrass community. Mar. Ecol. Prog. Ser., 312: 1-3.

Cornelisen, Christopher D. and Florence I. M. Thomas (2009). Prediction and validation of flow-dependent uptake of ammonium over a seagrass-hardbottom community in Florida Bay. Mar. Ecol. Prog. Ser., 386: 71-81.

Costanza, R., Ralph d'Arge, Rudolf de Groot, Stephen Farber, Monica Grasso, Bruce Hannon, Karin Limburg, Shahid Naeem, Robert V. O'Neill, Jose Paruelo, Robert G. Raskin, Paul Sutton, and Marjan van den Belt (1997). The value of the world's ecosystem services and natural capital. Nature 387: 253-260.

Denny, Mark and Loretta Roberson (2002). Blade motion and nutrient flux to the kelp. *Eisenia arborea*. Biol. Bull., 203: 1-13.

Duarte, Carlos M. and Carina L. Chiscano (1999). Seagrass biomass and production: a reassessment. Aquat. Bot. 65(1-4): 159-174.

Fernandez, Loretta A., John K. MacFarlane, Alexandra P. Tcaciuc and Philip Gschwend (2009). Measurement of freely dissolved PAH concentrations in sediment beds using passive samplers with low-density polyethylene. Environ. Sci. Technol., 43: 1430-1436.

Fernandez, Loretta A., Charles F. Harvey, and Philip M. Gschwend (2009). Using performance reference compounds in polyethylene passive samplers to deduce sediment porewater concentrations for numerous target chemicals. Environ. Sci. Technol., 43: 8888-8894.

Folkard, Andrew M. (2005). Hydrodynamics of model *Posidonia oceanica* patches in shallow water. Limnol. Oceanogr., 50(5): 1592-1600.

Fonseca, Mark S., M.A.R. Koehl, Blaine S. Kopp (2007). Biomechanical factors contributing to self-organization in seagrass landscapes. *J. Exp. Mar. Biol. and Ecol.,* 340(2): 227-246.

Fourqurean, James W., Carlos M. Duarte, Hilary Kennedy, Núria Marbà, Marianne Holmer, Miguel Angel Mateo, Eugenia T. Apostolaki, Gary A. Kendrick, Dorte Krause-Jensen, Karen J. McGlathery and Oscar Serrano (2012). Seagrass ecosystems as a globally significant carbon stock. Nature Geoscience 5: 505-509.

Ghisalberti, Marco and Heidi M. Nepf (2002). Mixing layers and coherent structures in vegetated aquatic flows. J. Geophys. Res. Oceans 107: 3011.

Graham, J. M. R. (1980) The forces on sharp-edged cylinders in oscillatory flow at low Keulegan-Carpenter numbers. J. Fluid Mech. 97: 331-346.

Higbie, R. (1935). The rate of absorption of a pure gas into a still liquid during short periods of exposure. Trans. Am. Inst. Chem. Eng. 31: 365-389.

Hollenbeck, K. J. (1998) INVLAP.M: A matlab function for numerical inversion of Laplace transforms by the de Hoog algorithm, http://www.isva.dtu.dk/staff/karl/invlap.htm

Huang, Ivy, Jeffrey Rominger, and Heidi Nepf (2011). The motion of kelp blades and the surface renewal model. Limonl. Oceanogr., 56(4): 1453-1462.

Hurd, C.L., P.J. Harrison, L.D. Druehl. (1996) Effect of seawater velocity on inorganic nitrogen uptake by morphologically distinct forms of Macrocystis integrifolia from wave-sheltered and exposed sites. Mar Biol 126: 205-214.

Jumars, Peter A., Jame E. Eckman, Evamaria Koch (2001). Macroscopic animals and plants in benthic flows. In Bernard P. Boudreau and Bo Barker Jørgensen (Eds.). *The Benthic Boundary Layer: Transport Processes and Biogeochemistry.* Oxford University Press.

Koch, Evamaria W., Edward B. Barbier, Brian R. Silliman, Denise J. Reed, Gerardo ME Perillo, Sally D. Hacker, Elise F. Ganek, Jurgenne H. Primavera, Nyawira Muthigam, Stephen Polasky, Benjamin S. Halpern, Christopher J. Kennedy, Carrie V. Kappel, and Eric Wolanski. (2009) Non-linearity in ecosystem services: temporal and spatial variability in coastal protection. Front Ecol. Env., 7: 29-37.

Koch, Evamaria W. and Giselher Gust (1999). Water flow in tide- and wave-dominated beds of the seagrass *Thalassia testudinum.* Mar. Ecol. Prog. Ser., 184: 63-71.

Koumoutsakos, P. and D. Shiels (1996). Simulations of the viscous flow normal to an impulsively started and uniformly accelerated flat plate. J Fluid Mech., 328: 177-227.

Kuo, J. and C. den Hartog (2006). Seagrass morphology, anatomy, and ultrastructure. In A.W.D. Larkum et al (Eds.). *Seagrasses: Biology Ecology and Conservation* (227-254). Dordrecht, The Netherlands: Springer.

Ledwell, J. J. (1984). The variation of the gas transfer coefficient with molecular diffusivity. In W. Brutsaert and G. H. Jirka (Eds.) *Gas Transfer at Water Surfaces* (293-302). Dordrecht, Netherlands: Reidel.

Lohmann, R. (2012). Critical review of low-density polyethylene's partitioning and diffusion coefficients for trace organic contaminants and implications for its use as a passive sampler. Environ. Sci. Technol., 46: 606-618.

Lohmann, R., and D. Muir (2010). Global aquatic passive sampling (AQUA-GAPS): Using passive samplers to monitor POPs in the waters of the world. Environ Sci Technol. 44: 860-864.

Lowe, Ryan J., Jeffrey R. Koseff, Stephen G. Monismith, and James L. Falter (2005). Oscillatory flow through submerged canopies: 1. Velocity structure. J. Geophys. Res., 110: C10016.

Lowe, Ryan J., Jeffrey R. Koseff, Stephen G. Monismith, and James L. Falter (2005). Oscillatory flow through submerged canopies: 2. Canopy mass transfer. J. Geophys. Res., 110: C10017.

Luhar, Mitul. (2012). Analytical and experimental studies of plant-flow interaction at multiple scales. (Doctoral dissertation). Massachusetts Institute of Technology, Cambridge.

Luhar, Mitul, S. Coutu, E. Infantes, S. Fox, and H. Nepf (2010), Wave-induced velocities inside a model seagrass bed, J. Geophys. Res., 115, C12005.

Luhar, Mitul and Heidi M. Nepf (2011). Flow induced reconfiguration of buoyant and flexible aquatic vegetation. Limnol. Oceanogr. 56(6) 2003-2017.

Luhar, Mitul and Heidi Nepf, (2013). From the blade scale to the reach scale: A characterization of aquatic vegetative drag. Advances in Water Resources. 51: 305-316.

McKone, Katie L. (2009) Light available to the seagrass Zostera marina when exposed to currents and waves. (Masters dissertation). The University of Maryland, College Park.

Morris, E. P. and G. Peralta, F. G. Brun, L. van Duren, T. J. Bouma, J. L. Perez-Llorens (2008). Interaction between hydrodynamics and seagrass canopy structure: Spatially explicit effects on ammonium uptake rates. Limnol. Oceanogr., 53(4): 1531-1539.

Nishihara, G. and J. Ackerman (2006). The effect of hydrodynamics on the mass transfer of dissolved inorganic carbon to the freshwater macrophyte *Vallisneria americana*. Limnol. Oceanogr., 51(6) 2734-2745.

Nishihara, G. and J. Ackerman (2009). Diffusive boundary layers do not limit the photosynthesis of the aquatic macrophyte *Vallisnera americana* at moderate flows and saturating light levels. Limnol. Oceanogr., 54(6): 1874-1882.

Romero, Javier, Kun-Seop Lee, Marta Pérez, and Miguel A. Mateo, Teresa Alcoverro (2006). Nutrient dynamic in seagrass ecosystems. In A.W.D. Larkum et al (Eds.). *Seagrasses: Biology Ecology and Conservation* (227-254). Dordrecht, The Netherlands: Springer.

Rominger, Jeffrey T. (2013). Hydrodynamic and transport phenomena at the interface between flow and aquatic vegetation: from the forest to the blade scale. (Doctoral dissertation). Massachusetts Institute of Technology, Cambridge.

Rominger, Jeffrey T. and Heidi M. Nepf (2014). Effects of blade flexural rigidity on drag force and mass transfer rates in model blades. In press Limnology and Oceanography.

Sanford, LP, and SM Crawford (2000). Mass transfer versus kinetic control of uptake across solid-water boundaries. Limnol. Oceanography 45:1180-1186.

Sparrow, E. M. and K. K. Tien (1977). Forced convection heat transfer at an inclined and yawed square plate – application to solar collectors. J. Heat Transfer, 99: 507-512.

Sparrow, E. M., J. W. Ramsey, and E. A. Mass (1979). Effect of finite width on heat transfer and fluid flow about an inclined rectangular plate. J. Heat Transfer, 101: 199-204.

Stevens, Craig L., Catriona L. Hurd (1997). Boundary-layers around bladed aquatic macrophytes. Hydrobiologia 346: 119-128.

Stevens, Craig L. Catriona L. and Pal E. Isachsen (2003). Modelling of diffusion boundary-layers in subtidal macroalgal canopies: The response to waves and currents. Aquat. Sci., 65: 81-91.

Swarzenbach, Rene P., Philip M. Gschwend, and Dieter M. Imboden (2003). *Environmental Organic Chemistry* (p. 889-943). 2nd Edition. Hoboken, NJ: John Wiley and Sons.

Tcaciuc, A. Patricia, Jennifer Apell, and Philip M. Gschwend (2014). Modeling the transport of organic chemicals between polyethylene passive samplers and water in finite and infinite bath conditions. In preparation.

Thomas, F. I. M. and C. D. Cornelison (2003). Ammonium uptake by seagrass communities: effects of oscillatory versus unidirectional flow. Mar. Ecol. Prog. Ser., 247: 51-57.

Touchette, Brant W. and JoAnn M. Burkholder (2000). Review of nitrogen and phosphorus metabolism in seagrasses. J. Exp. Mar. Ecol., 250: 133-167.

Vogel, S. (1994). *Life in Moving Fluids.* Princeton Univ. Press.

Waycott, Michelle, Ben J. Longstaff, and Jane Mellors (2005). Seagrass population dynamics and water quality in the Great Barrier region: A review and future research directions. Marine Pollution Bulletin, 51: 343-350.

Weitzman, Aveni-Deforge and Thomas Koseff (2013). Uptake of dissolved inorganic nitrogen by shallow seagrass communities exposed to wave-driven unsteady flow. Mar. Ecol. Prog. Ser., 475: 65-83.

Zeller, Robert B., Joel S. Weitzman, Morgan E. Abbett, Francisco J. Zarama, Oliver B. Fringer and Jeffrey R. Koseff. Improved parameterization of seagrass blade dynamics and wave attenuation based on numerical and laboratory experiments. Limnol. Oceanogr., 59(1): 251-266.

Zimmerman, Richard C. (2006). Light and photosynthesis in seagrass meadows. In A.W.D. Larkum et al (Eds.). *Seagrasses: Biology Ecology and Conservation* (303-321). Dordrecht, The Netherlands: Springer.